Study of Laser-Driven Ion Acceleration Through Relativistic Self-Induced Transparency

THESIS

Submitted in partial fulfillment
of the requirements for the degree of

DOCTOR OF PHILOSOPHY

by

SHIVANI CHOUDHARY
ID No. 2013PHXF0402P

Under the Supervision of

Dr. Amol R. Holkundkar

BIRLA INSTITUTE OF TECHNOLOGY AND SCIENCE, PILANI

JANUARY 2019

BIRLA INSTITUTE OF TECHNOLOGY AND SCIENCE, PILANI

CERTIFICATE

This is to certify that the thesis entitled "**Study of Laser-Driven Ion Acceleration Through Relativistic Self-Induced Transparency**", submitted by **Shivani Choudhary** ID No **2013PHXF0402P** for award of Ph.D. of the Institute embodies original work done by her under my supervision.

(Dr. Amol R. Holkundkar)

Associate Professor, Department of Physics
BITS-Pilani, Pilani Campus, Rajasthan India

Date:

DEDICATED TO ...
My Parents and Sister

तीव्रसंवेगानामासन्नः

The more intense faith and effort, the closer the goal will be
- Patanjali Yoga Sutra 1.21

We don’t make mistakes, We just have happy accidents
-Bob Ross

ACKNOWLEDGEMENTS

With God's grace and wisdom, first and foremost, I would like to acknowledge my thesis supervisor Dr. Amol R. Holkundkar, for his valuable guidance and support during my entire research work. It was his knowledge and incentive that kept me awake every time and guided me all throughout this crucial phase of life. His support was a tremendous assist to me that made my research ongoing till its last phase.

I am very grateful to Prof. Souvik Bhattacharyya, Vice Chancellor, BITS Pilani, for giving me an opportunity to work in such a premier institute. Also, I am thankful to Prof. A.K. Sarkar, Director, BITS Pilani, for creating such a wonderful environment of knowledge and learning throughout the campus, which helped me to build my research career ahead. I express my gratitude to Prof. Srinivas Krishnaswamy (Dean) and Dr. Jitendra Panwar (Associate Dean), Academic Graduate Studies and Research Division, BITS-Pilani for their official support and encouragement.

I am very much thankful to Dr. R.K.Gupta, present Head and all the previous HoD's for providing me with all the required facilities which were needed during my entire span of research work. I am very much obliged to my Doctoral Advisory Committee members Dr. Jayendra Nath Bandyopdhyay and Dr. Rakesh Choubisa, Department of Physics, BITS Pilani, Pilani Campus for taking immense pain in listening to all of my research work and giving me critical inputs regarding my work that have improved the thesis the way it looked from time to time. Also, I want to take this platform to acknowledge all the respected faculty members for giving all the efforts in molding me throughout my work by constant motivation and encouragement. I am grateful to the Department of Physics, BITS Pilani for providing all sorts of computational facilities and creating such pleasant surroundings. It would be very injustice if I fail in accepting the contribution of all the supporting staff Mr. Shrikant Sharma, Mr. Rajiv Gaur and Mr. Kundan Singh Shekhawat of the Department of Physics in every small or big task.

Also, I want to appreciate all of my fellow research scholars, juniors and seniors, for their great company who have shared all the joy and happiness, pain and agony and cherished every moment that I have spent with them during my stay here in Pilani. I am very much lucky to have Mr. Pradeep Yadav, Ms.

Prachi Venkat, Ms. Nikita Dhankhar, Mr. Rambabu Rajpoot, Ms. Khushboo Rao, Ms. Aayushi Agarwal and Ms. Aditi Mandal for standing beside me in all the times and making my stay more memorable and stress free for the past year. All of their support, generosity, and patience in all the times is really admirable and their timely suggestions have been helpful to me in overcoming any obstacles on a way to success.

I would like to acknowledge Birla Institute of Technology and Science, Pilani for giving me an all the world class facilities here that made me flourish and excel in every aspect of life. Last but not the least, I want to sincerely thank all the people for their great company, who have crossed in my life during this entire stay in BITS Pilani. I am delighted to thank every one of them who have contributed and supported me by keeping a zest alive within me.

Finally, I am indebted to my parents, my sister and Dr. Sachin Kumar for there faith, trust, patience, love, and care. They were the immense supporting pillar for me every time I was in a tough situation. Their blessings and invaluable support throughout my academics have been my strength making me reach this stage and pursue higher studies.

And most importantly, I want to behold and bow down in front of The Great Almighty God for keeping the ray of hope alive within me during all the sleepless night and wildest dreams, and making everything become possible at the end.

Shivani Choudhary
BITS-Pilani

ABSTRACT

The progress in the compact laser driven particle accelerators have paved the possibilities to efficiently accelerate the electrons and ions to MeVs and GeVs of energies, which promises a vast variety of applications in both fundamental and applied sciences. The thesis presents the theoretical and numerical studies of the ion acceleration from ultra-short laser pulses under the purview of Relativistic Self-Induced Transparency (RSIT) Mechanism.

We studied the effect of target thickness on ion acceleration though RSIT using one dimensional cold fluid model and also by particle-in-cell simulations. There is a threshold target density which allows the maximum transmission of the laser pulse and beyond it, the target becomes opaque. We have obtained a suitable scaling law for optimum laser and target conditions. The energy spectrum obtained is more significant from the applied perspective, if an extra low density layer is used instead of relying only on target ions.

In this thesis, we also studied the effect of pulse chirp on the transmission coefficient of the target for given laser and target parameters. We have used the sub-wavelength targets and the transmission coefficients are calculated by numerically solving the wave propagation equation with the corrected electron density, while taking into account the time-dependent frequency and amplitude of the circularly polarized chirped laser pulse. With the introduction of a very thin, low density ($< n_c$) secondary layer behind the primary layer have resulted in the acceleration of the ions as a mono-energetic bunch. The acceleration is mainly caused by the electrostatic field created by the primary layer upon interaction by the negatively chirped pulse.

We have also investigated the propagation of the laser pulses in the underdense plasma for two regimes, one with $a_0 < 1$ and other with $a_0 \geq 10$. For $a_0 < 1$ case, we used a cold relativistic fluid model, and the effect of laser pulse amplitude, pulse duration, and plasma density is studied and compared with the expected scaling laws as well as with the PIC simulations. For $a_0 \geq 10$, the study is done only using PIC simulation. In addition to it, the effective increase in the peak energy of a thin, low density secondary layer ions was observed, when the dispersed laser pulse is allowed to interact with the two layer composite target.

Contents

1 Introduction 1
1.1 Generation of Ultrashort Laser Pulses 2
1.2 Terminologies Associated with Laser-Plasma Interaction 5
1.2.1 Basic plasma phenomenon 6
1.2.2 Laser-plasma interaction concept 8
1.3 Application of Laser-Plasma Interaction 14
1.4 Overview of the Thesis 16
1.4.1 Ion Acceleration by Relativistic Self-Induced Transparency Mechanism 17
1.4.2 Chirp Assisted Ion Acceleration Through Relativistic Self-Induced Transparency 18
1.4.3 Laser Pulse Dispersion in Underdense Plasma and Associated Ion Acceleration 19
1.5 Thesis Framework 20

2 Laser Plasma Induced Particle Acceleration Mechanisms 23
2.1 Electron Acceleration Mechanisms 23
2.1.1 Laser Wakefield Acceleration (LWFA) 23
2.1.2 Self Modulated Laser Wakefield Acceleration (SMLWFA) 25
2.2 Ion Acceleration Mechanisms 25
2.2.1 Target Normal Sheath Acceleration (TNSA) 26
2.2.2 Radiation Pressure Acceleration (RPA) 30
2.2.3 Break-Out Afterburner (BOA) 33
2.2.4 Relativistic Self-Induced Transparency (RSIT) 34

3 Ion Acceleration by Relativistic Self-Induced Transparency 37
3.1 Model for Study 37
3.1.1 Relativistic cold fluid model 37
3.1.2 PIC Simulation 42
3.2 Results and Discussion 43
3.2.1 Difference between Light Sail (LS) and Induced Transparency (RSIT) Regime 43

3.2.2 Formation of electrostatic field 44
3.2.3 Ion acceleration 46
3.2.4 Optimization 49
3.2.5 Ion energy comparison 50
3.3 Summary 52

4 Chirp Assisted Ion Acceleration Through Relativistic Self-Induced Transparency 53
4.1 Theory and Simulation Model 54
4.1.1 Wave propagation model 56
4.1.2 Comparison with PIC simulations 59
4.2 Results and Discussion 60
4.2.1 Chirp effect on threshold plasma density 62
4.2.2 Spatio-temporal evolution of electrostatic field 64
4.2.3 Need for secondary layer 65
4.3 Optimization 69
4.4 Summary 71

5 Laser Pulse Dispersion in Underdense Plasma and Associated Ion Acceleration 73
5.1 Theory and Simulation Model 73
5.2 Results and Discussion 76
5.2.1 Pulse dispersion for $a_0 < 1$ 77
5.2.2 Pulse dispersion for $a_0 > 1$ 83
5.3 Ion Acceleration by Intense Dispersed Pulses 86
5.4 Summary 91

6 Summary and Future Scope 93

A Relativistic Cold-Fluid Model - RSIT Mechanism 99

B Numerical Methods 105

C Particle In Cell Simulations 107
C.1 Particle in cell (PIC) simulation method 107
C.2 LPIC++ - 1D Electromagnetic PIC Code 109
C.2.1 Kinetic energy of particles 111

Bibliography 112

List of Publications 129

Brief Biography of the Supervisor 131

Brief Biography of the Candidate 132

List of Figures

1.1 *Time scale of evolution of lasers and associated physics aspects (courtesy Wikipedia).* 3

1.2 *The schematic representation of chirped pulse amplification technique (courtesy Wikipedia).* 4

2.1 *The schematic diagram of target normal sheath acceleration mechanism. (a) when laser pulse irradiates the front surface of the solid target, accelerating fast electrons and propagate through to the rear surface. (b) The electrostatic field produced is strong enough to ionise the target surface and accelerate the ions. Also, the front surface ion acceleration occurs mainly due to the expansion of the laser-generated plasma.* 27

2.2 *Diagrammatic illustration of Hole boring regime for thick targets (a) and light sail regime for thin targets (b) in radiation pressure acceleration.* 31

2.3 *Diagrammatic representation of three stages of Break-out Afterburner mechanism. (a) TNSA, (b) enhanced TNSA and (c) Break-out Afterburner.* 34

2.4 *Diagrammatic illustration of processes in RSIT mechanism. (a) When a part of a laser pulse reflects while interaction with overdense plasma target. (b) Now the transparent region, where the relativistic factor γ decreases the target density, for laser pulse to penetrate and (c) making the target underdense for laser pulse to completely propagate through the target.* 35

3.1 *The component of the laser field along x direction (E_x) and electrostatic field (E_z) created by charge separation is presented by numerically solving Eqs. 3.2 - 3.8 (left panel) and compared with 1D PIC simulations (right panel).* 40

3.2 *Variation of threshold electron density (n_{th}) with laser amplitude is presented. Curve 'A' shows the expression given by Eq. 3.10. Points denote the results obtained by the 1D fully relativistic PIC simulation for a target thickness of 1λ (square), 0.5λ (circle) and 0.25λ (triangle). Curves 'B' and 'C' respectively show the qualitative estimate of threshold density for $d = 0.5\lambda$ and $d = 0.25\lambda$ using Eq. 3.11.* 41

3.3 *A schematic illustration of simulation domain (60 λ) where double layer target geometry place at 15λ. d and σ corresponds to different primary layer target thickness and density. A Flattop laser pulse is incident on the target with $\tau = 6cycles$ (rise and fall = 1cycle) from left side of domain.* 42

3.4 *The spatial profile of electrostatic field (E_z) and laser field (E_x) is plotted at 26τ for three different target thicknesses having density 7n_c.* . 44

3.5 *Space-time dependence of electron density for target thickness 0.5λ (a) and 0.25λ (b) along with longitudinal electrostatic field (E_z) for these two cases respectively are presented in (c) and (d).* 46

3.6 *Velocity spectrum (a) of target ions and ions from secondary layer is measured at 90τ for the case $a_0 = 20$, $d = 0.25\lambda$, $n_e = 3n_c$, $5n_c$ and $7n_c$. The energy spectrum (b) for $n_e = 5n_c$ at different time steps is also presented.* 47

3.7 *Variation of maximum energy of accelerated ions (from secondary layer) with density and thickness of primary layer for different laser amplitudes.* 48

3.8 *Optimum density of primary target is presented as a function of it's thickness and laser amplitude. The solid line represents the scaling law for optimum density as a function of laser amplitude and target thickness (Eq. 3.12). At these optimum densities ions from the secondary layer attains maximum energy.* 49

4.1 *Laser pulse profiles with negative (a), unchirped (b) and positive (c) chirp parameters. Time dependent frequency is also illustrated (dotted line) for each case as well.* 54

4.2 *(a), (b) and (c) represents the diagrammatic representation of simulation domain with different laser and target parameters used throughout the chapter. Here, domain(a) corresponds to Fig. 4.3 - Fig. 4.4, (b) discusses about Fig. 4.6 - Fig. 4.7 and (c) domain is used for Fig. 4.8 - Fig. 4.12. The simulation domain is considered of 100λ and plasma target is placed at a distance of 25λ in both the target geometry. The laser pulse used for interaction is circularly polarized with Gaussian envelope.* 55

4.3 *Transmission coefficient of the laser pulse ($a_0 = 0.5$, $\tau = 5$ cycles) for chirp parameters $\zeta = -5, 0, 5$ for different target thickness of density $n_0 = 1n_c$ is compared. The schematic diagram representing the target geometry (Eq. 4.4), incident pulse and transmitted pulse is illustrated as an inlet.* 56

4.4 *PIC simulation for transmission coefficient of the laser pulse ($a_0 = 0.5$, $\tau = 5$ cycles) for chirp parameters $\zeta = -5, 0, 5$ for different target thickness of density $n_0 = 1n_c$ is compared.* 58

4.5 *Variation of threshold target density for 80% and 1% transmission with chirp parameter.* 60

4.6 *The effect of pulse chirp is illustrated for two different target densities, $3n_c$ (upper panel) and $6n_c$ (lower panel). The spatial snapshot at 60τ for the electron density (a,e), ion density (b,f), longitudinal electric field (c,g) and transverse laser profile (d,h) is presented for $a_0 = 20$, $\tau = 5$ cycles and $d = 0.75\lambda$ (the target is placed at 25λ)* 61

4.7 *Spatio-temporal profile of the electron density (upper panel) and the longitudinal electrostatic field (lower panel) are presented for chirp parameters $\zeta = -5$ (left column), $\zeta = 0$ (center column) and $\zeta = 5$ (right column). The laser parameters are same as Fig. 4.6 with target density $n_e = 6n_c$.* 63

4.8 *Phasespace plots for the ions from the primary layer ($d = 0.75\lambda$, $n_e = 6n_c$) for Hydrogen (a,b) and Deuterium (c,d) at 50τ and 90τ are presented. The ions from the secondary layer ($0.2\lambda, 0.1n_c$) are presented in center column. The secondary layer in both the cases is considered to be of Hydrogen plasma. The velocity spectrum for the ions from primary and secondary layers are illustrated in right column. Here, we have considered a circularly polarized, Gaussian, 5 cycle laser pulse with $\zeta = -5$ and $a_0 = 20$.* 64

4.9 *Spatio-temporal evolution of the ion density of PL (upper panel) and SL (lower panel) are presented for* ***H+H*** *(a,b) and* ***D+H*** *(c,d) cases. The laser and target conditions are same as in Fig. 4.8.* 66

4.10 *The energy spectrum of primary and secondary ions are evaluated at 90τ for different chirp parameters (a) and (c). Moreover, the energy spectrum of the ions from the primary (d) and secondary (b) layer are presented at different time instances for $\zeta = -5$. All other laser parameters are same as Fig. 4.8.* 67

4.11 *The effect of the pulse chirping on the maximum energy of the ions from the secondary layer is presented for different primary target density (a). The thickness of the primary layer is* 0.75λ *and peak laser amplitude is* $a_0 = 20$*. The variation of the maximum ion energy with* a_0 *is presented in (b), here we have fixed the density of the primary layer to* $6n_c$*.* 69

4.12 *The longitudinal electrostatic field (a) and energy spectrum of the ions from secondary layer (b) are presented for three different primary target conditions. However, the maximum ion energy of the secondary layer is also presented for different thicknesses and densities of the primary layer (c). The laser pulse with peak amplitude* $a_0 = 20$*, duration 5 cycles and chirp parameter* $\zeta = -5$ *is considered. The target conditions* $(d/\lambda, n_e/n_c)$ *are X (0.55,5.2), Y (0.75,5.8), and Z (0.95,6.8). All the quantities are evaluated at* 90τ*.* 70

5.1 *(a), (b) and (c) corresponds to various simulation domain taken into account for different laser and target parameters. Here, domain (a) is taken into consideration for Fig. 5.2 - Fig. 5.6. Similarly, domain (b) corresponds to Fig. 5.7 - Fig. 5.9 and domain (c) discusses Fig. 5.10 - Fig. 5.12 For all the cases linearly polarized, Gaussian laser pulse is taken into account.* 74

5.2 *The spatial profile of the electromagnetic (transverse) fields (a,c) and electrostatic (longitudinal) fields (b,d) is presented at different time instances using fluid simulation (left panel) and PIC simulation (right panel). Here, we modeled the interaction of the 800 nm, 3 cycles (FWHM) Gaussian laser pulse* $(a_0 = 0.1)$ *with plasma having density* $0.5n_c$*.* 75

5.3 *The temporal evolution of the pulse length (red circle, left axis) and the peak field amplitude (blue filled circles, right axis) as it propagates in the underdense plasma is compared by fluid (a) and PIC simulations (b). The pulse length* L_{fwhm} *is estimated in units of the fundamental wavelength of the laser pulse, similarly time is presented in units of fundamental laser cycle. The laser and plasma conditions are same as Fig. 5.2.* 76

5.4 *Temporal evolution of the peak laser amplitude (a) and pulse length (b) is presented for different plasma densities. The results of the PIC simulations are also shown with open circles in both (a) and (b). The peak amplitude is normalized to the peak value of the pulse at* $t = 10\tau$ (a_{p10})*. The value of these parameters are evaluated at 100*τ *are also presented in (c) for different* n_e/n_c*. The* $a_0 = 0.1$ *and* $\tau_{fwhm} = 3$ *cycles is considered for this case.* 78

5.5 *Temporal evolution of the peak laser amplitude (a) and pulse length (b) is presented for different pulse duration. The results of the PIC simulations are also shown with open circles in both (a) and (b). The peak amplitude is normalized to the peak value of the pulse at it would be at* $t = 10\tau$ *(*a_{p10}*). The value of these parameters are evaluated at 100*τ *and are presented in (c) for different* τ_{fwhm}. *The* $a_0 = 0.1$ *and* $n_e = 0.5n_c$ *is considered for this case.* 79

5.6 *Temporal evolution of the peak laser amplitude (a) and pulse length (b) is presented for different laser amplitudes. The results of the PIC simulations are also shown with open circles in both (a) and (b). The peak amplitude is normalized to the peak value of the pulse at it would be at* $t = 10\tau$ *(*a_{p10}*). The value of these parameters are evaluated at 100*τ *and are presented in (c) for different* a_0. *The* $n_e = 0.5n_c$ *and* $\tau_{fwhm} = 3$ *cycles is considered for this case.* 80

5.7 *The temporal snapshots of the laser field as evaluated at 30, 60 and 90*λ *is illustrated for the case when 3 cycle laser with* $a_0 = 20$ *is propagating in the plasma with density 0.01*n_c *(a), 0.02*n_c*(b) and 0.03*n_c*(c). The Fourier spectrum of the laser pulse as evaluated at* 90λ *is also compared for different plasma densities (d).* 82

5.8 *The temporal snapshots of the laser field as evaluated at 30, 60 and 90*λ *is illustrated for the 3 cycle laser propagating in the plasma with density 0.03*n_c. *The laser amplitude* $a_0 = 10$ *(a), 15(b) and 20(c) are considered. The Fourier spectrum of the laser pulse as evaluated at* 90λ *is also compared for different laser amplitudes (d).* 84

5.9 *Temporal evolution of the laser pulse energy (a) and the longitudinal field energy (b) is presented for 3 cycle Gaussian pulse with* $a_0 = 10,\ 20$ *when it propagated in the plasma with density* $0.01,\ 0.03n_c$. *The laser pulse energy in (a) is normalized to maximum value at* $t = 10\tau$*, as we are interested in the depletion rate of the laser pulse energy for different laser and plasma parameters.* 85

5.10 *The energy spectrum of the ions from the secondary layer as evaluated at 170*τ *are presented for different pre-target plasma densities (a). The variation in the peak energy of the ions from the secondary layer with pre-target plasma density (*n_0*) is illustrated (b). We have used 3 cycles, Gaussian, linearly polarized laser with peak amplitude* $a_0 = 20$. *The geometry of the setup is also illustrated as an inlet, here* n_0, n_1 *and* n_2 *respectively represents the pre-target plasma density, density of the primary layer and secondary layer.* 87

5.11 *The spatial profile of the longitudinal electrostatic field is presented at different time instances for different underdense plamsa densities. The spatial profile of the transverse electric field (e) and electron density (f) profiles are also presented as evaluated at 50τ. The laser and target parameters are same as mentioned in Fig. 5.10.* 88
5.12 *The phasespace plots of ions from the pre-target plasma along with the primary layer (left column) and the secondary layer (right column)are presented at different time instances from 50τ to 170τ. The pre-target layer is of Hydrogen with thickness of 50λ and density n_0 = 0.11n_c . The primary layer is comprised of Deuterium plasma of 0.75λ and n_1 = 3.5n_c; along with the secondary layer Hydrogen having thickness and density respectively 0.2λ, 0.1n_c.* 89

B.1 *Central difference scheme for solving differential equations* 106

C.1 *Particle-in-cell (PIC) simulation technique* 108
C.2 *Simulation geometry of LPIC++, lables show the actual name of input parameter.* 109

LIST OF ABBREVIATIONS/SYMBOLS

Symbols

c	speed of light in vacuum
ϵ_0	permittivity of free space
μ_0	magnetic permeability of free space
m_e	mass of electron
m_i	mass of ion
p	momentum
$v_{e,i}$	electron and ion velocity
e	electron charge
Z	atomic number
τ	laser cycle
λ	laser wavelength
λ_D	Debye length
ω	laser frequency
ω_s	seed frequency
ω_{pump}	pump frequency
ω_p	plasma frequency
Ω_p	ion plasma frequency
ω_i	idler photon frequency
K_B	Boltzmann constant
T_e	electron temperature (in kelvins)
$n_{e,i}$	plasma electron and ion density
$q_{e,i}$	plasma electron and ion charge
n_c	plasma critical density

N_D	number of particles in Debye sphere
v_g	group velocity of the wave
v_{HB}	hole boring velocity of ion
v_ϕ	phase velocity of the wave
η	refractive index
γ	relativistic factor
Ξ	maximum ion energy
β_{ls}	sail velocity
τ_{acc}	acceleration time of ions
δ	skin depth
$\mathbf{E}, \mathbf{B}$	Electric and Magnetic field
$\mathbf{A}$	Magnetic vector potential
$\mathbf{j}$	current density
$\mathbf{k}$	wave vector
$\mathbf{F_{NL}}$	Non-linear force
$\mathbf{f_P}$	Ponderomotive force per unit volume
U_p	Ponderomotive potential
p_z^e	longitudinal electron momentum
d_{opt}	optimum target thickness
$\mathcal{F}$	laser pulse energy per unit surface
ϕ	scalar potential
ρ	charge density
a_0	normalized laser pulse amplitude
ζ	chirp parameter of laser pulse

Abbreviations

ELI	Extreme Light Infrastructure
MeV	Megaelectron-Volt

GeV	Gigaelectron-Volt
TNSA	Target Normal Sheath Acceleration
BOA	Break-Out Afterburner
RPA	Radiation Pressure Acceleration
HB	Hole Boring
LS	Light Sail
RSIT	Relativistic Self-Induced Transparency
fs	femtosecond
ps	picosecond
CPA	Chirp Pulse Amplification
OPCPA	Optical Parametric Chirped Pulse Amplification
OPA	Optical parametric Amplifiers
EM	Electromagnetic
ICF	Inertial Confinement Fusion
FI	Fast Ignition
DCE	Directed Coulomb Explosion
PIC	Particle-in-Cell
PWFA	Plasma Wakefield Acceleration
LWFA	Laser Wakefield Acceleration
SMLWFA	Self Modulated Laser Wakefield Acceleration
CSL	Charge separation layer
CEL	Compressed electron layer
CFL	Courant-Friedrichs-Lewy
LP, CP	Linearly polarized, Circularly polarized
FWHM	Full width half maximum
PL, SL	Primary layer, Secondary layer

CHAPTER 1

Introduction

Lasers being a monochromatic coherent source of energy has emerged out as an outstanding advancement in the field of science, medicine, and technology. The advent of high power lasers promised the vast number of applications, covering both applied and fundamental aspects of basic sciences. The research in the field of laser-plasma interaction has turned out to be vigorous and persuasive over a few decades. With the highly advanced Extreme Light Infrastructure (ELI) laser facility, it is possible to obtain the intensity $\sim 10^{24}$ W/cm^2 [1]. One of the most significant breakthrough is in the field of laser based particle acceleration, which has attracted a great deal of research interest in recent decades. The table-top setup for the acceleration of ions and electrons to relativistic energies is a result of the technological advances in the field of high power lasers [2]. The laser-plasma based acceleration of the ions and electrons paved the possibility of constructing high energy charged particle beams for medical [3, 4] and industrial applications [5, 6].

The development of an efficient acceleration mechanism from both experimental and theoretical perspective has become a widespread field of interest. High energetic particle beam source promises remarkable applications in various areas of applied sciences [6–11]. In the last couple of decades, we have already witnessed the experimental realizations of the acceleration of ions to multi MeV of energies via various acceleration mechanisms depending on the laser and the target conditions.

The idea of the laser wakefield acceleration as demonstrated in Refs. [12–14] manifested the possibilities to accelerate the electrons to GeV of energies. The acceleration of the target ions to MeV of energies is also proved to be feasible with existing ultraintense lasers. Among all acceleration mechanisms, the Target Normal Sheath Acceleration (TNSA) is studied extensively on both experimental and theoretical fronts [15–19]. When target thickness is comparable to the skin depth of the plasma, then, after TNSA, another mechanism takes over, namely Break-Out Afterburner (BOA). In BOA, the hot electron plasma expands sufficiently by laser pondermotive force, as a consequence the target becomes underdense, the laser penetrates the target, and a strong electric field is induced through Buneman instability, resulting in the conversion of electron energy to ion energy, and thus ions are accelerated to very high energies [20, 21]. The Radiation Pressure Acceleration (RPA) begins to dominate the acceleration process for the laser intensity $\gtrsim 10^{20}$ W/cm^2 [22–26]. Depending on target thickness, the RPA mechanism is characterized as Hole Boring (HB) for thick targets and Light Sail (LS) for the thin targets. The RPA is mainly governed by the circularly polarized laser pulse so that $\mathbf{j} \times \mathbf{B}$ heating can be avoided and electrons are pushed deeper into the targets. In HB, radiation pressure drives material ahead of it like a piston but does not interact with the rear surface of the target [25, 27]. In the LS regime, the target is sufficiently thin such that the laser can accelerate the foil as a whole [28, 29]. One of the ion acceleration mechanism thoroughly discussed in this thesis is Relativistic Self Induced Transparency (RSIT). The RSIT is found to be a viable way to accelerate ions to MeVs of energy [30–33]. However, the laser intensity used for RSIT mechanism is comparatively lesser than it would have been required for other acceleration mechanisms.

We discuss the basic technique of generating ultraintense and ultrashort laser pulses in Section 1. The basic fundamentals of the plasma physics and different terminologies involved in the laser plasma interaction are explained in Section 1.2. The applications of the ion acceleration is presented in Section 1.3, followed by the overview of our published work in Section 1.4. The outline of the thesis is presented in Section 1.5.

1.1 Generation of Ultrashort Laser Pulses

Ultrashort laser pulses are designated as the laser pulses having a duration of a few tens of picoseconds (10^{-12} sec) to femtoseconds (10^{-15} sec). The delivery of several millijoules of energy in a time span of several femtoseconds over an area of around few microns results in laser intensities of the order $\sim 10^{20}$

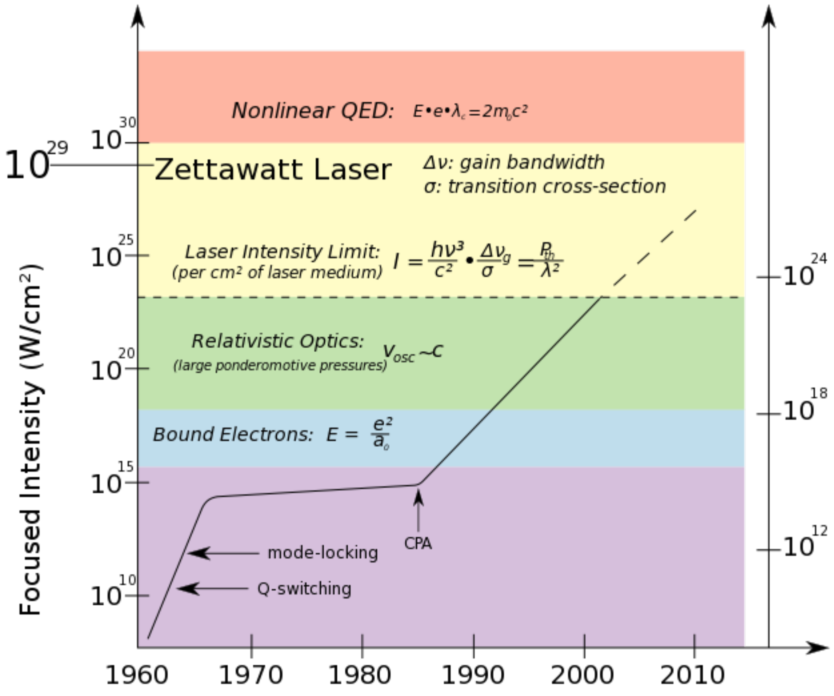

Figure 1.1: *Time scale of evolution of lasers and associated physics aspects (courtesy Wikipedia).*

W/cm^2. The demand for high intensity from the conventional lasers such as Ti-Sapphire or Nd-YAG resulted in the requirement for the generation of ultra-short pulses. The restriction in the peak power of the laser system was mainly limited by the damage threshold of the optical components of the laser systems.

The time evolution of the laser intensities throughout years is presented in Fig. 1.1. With the early development of lasers in the 1960s, the techniques like mode-locking and Q-switching proved to be promising to increase the peak intensity of the laser pulses [34–36]. The concept of Q-switching was able to realize the pulse duration in the range of about 10 nanoseconds [36]. However, with the mode-locking method (active [34] and passive [35]) the laser pulse duration of the order $\sim$ 5 fs were achieved [37]. For more than a decade the peak intensity of the lasers is almost saturated by the damage threshold of the optical components of the laser amplification system till the technique of *Chirped Pulse Amplification* (CPA) was introduced in 1985 by Strickland and Mourou [38].

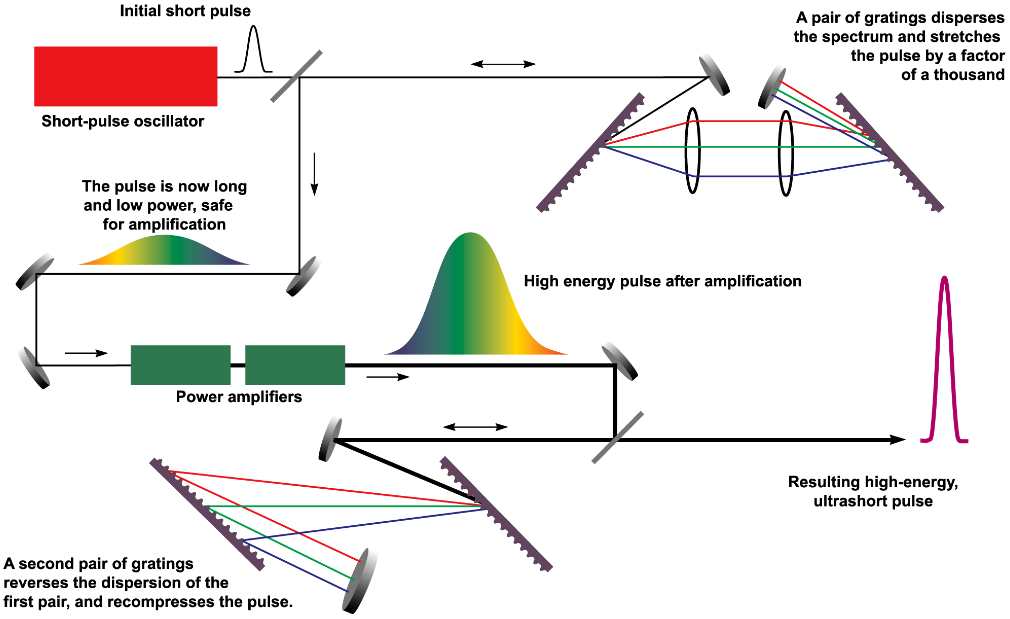
Initial short pulse
Short-pulse oscillator
A pair of gratings disperses the spectrum and stretches the pulse by a factor of a thousand
The pulse is now long and low power, safe for amplification
High energy pulse after amplification
Power amplifiers
Resulting high-energy, ultrashort pulse
A second pair of gratings reverses the dispersion of the first pair, and recompresses the pulse.

Figure 1.2: *The schematic representation of chirped pulse amplification technique (courtesy Wikipedia).*

The schematic representation of the chirped pulse amplification technique is shown in Fig. 1.2. In this technique, initially, the generated laser pulse is temporally stretched such that the peak power is lower than the damage threshold of the gain medium. Then, this stretched pulse is amplified in the gain medium without damaging the amplifiers due to reduced peak power. In the last stage, the amplified pulse is again compressed to a shorter duration. The pulse is stretched and compressed with the help of pair of gratings. The Nobel Prize in 2018 is awarded to D. Strickland and G. Mourou for the invention of the "Chirped Pulse Amplification (CPA)" [38]. Furthremore, half of the prize was shared by Arthur Ashkin for "Optical Tweezers", a device used for grabbing and manipulating small objects, and its application in biological systems [39].

To build high power lasers, the laser pulse needs to be shrunk further with high energy content. However, the gain-narrowing limit in the amplifier medium put constraints on CPA. These limitations are largely removed by the technique called as Optical Parametric Chirped Pulse Amplification (OPCPA). The optical parametric amplifiers (OPA) are used for increased gain bandwidth to obtain higher output energies. In OPA, two light beams (pump and seed) having frequency ω_{pump} and ω_s respectively, interact in a nonlinear crystal, yielding amplified ultrashort signal and idler pulses ω_i. The difference between the photon energies of the pump and signal wave is the idler wave photon energy. The pump energy is fully converted into signal and idler beam energy while avoiding the heating of crystal. Furthermore, the efficient transfer of energy is governed by the phase matching of all the frequencies.

The integration of CPA concept to optical parametric amplifiers (OPA) lead to the *optical parametric chirped-pulse amplification* (OPCPA), was first proposed by Dubietis [40]. OPCPA is a powerful tool for the generation of ultrashort pulses with extremely high peak power and pulse duration of few cycles. The experimental and numerical studies targeting the several aspects of OPCPA performance and development are discussed in Refs. [41, 42]. However, the theoretical studies have been performed in Refs. [43–47]. In this scheme, a pump beam with relatively narrow spectral bandwidth with longer pulse duration, and a seed pulse with extremely reduced peak intensity having a temporally chirped broad bandwidth is amplified by OPA to large bandwidth and chirped signal and idler pulse. Finally, these pulses are compressed to generate high intensity ultrashort pulses. It can be noted that if pump pulse and seed pulse overlaps, an adequate amount of energy extraction can occur, thus resulting in a high power signal and idler pulses [48]. The advantage of OPCPA is that it does not involve multipass geometries for amplification, as a result high gain bandwidth results in the generation of high energy pulse under optimum phase matching conditions.

1.2 Terminologies Associated with Laser-Plasma Interaction

In the previous Section 1, we focused on the generation of ultrashort laser pulses. In the current section, we would like to discuss the interaction of these ultraintense laser pulses with the plasma medium. The objective is to briefly describe the basic concepts of plasma and few terminologies associated with the process of laser plasma interaction.

1.2.1 Basic plasma phenomenon

The "Plasma" is a quasineutral gas of charged and neutral particles that exhibit collective behavior [49]. By *Collective Behavior*, we mean the condition that also depends on the state of the plasma in the remote region as well, along with local conditions. However, *quasi-neutrality* hints toward the presence of an approximately same number of positive and negative charge particles in the plasma. In this section, we discuss some typical characteristics of the plasma.

1. **Debye length**

   Debye length is a measure of the shielding distance or thickness of the sheath i.e., the scale over which mobile charge carriers screen out the electric field in plasmas. It is given by:

   $$\lambda_D = \left(\frac{\epsilon_0 K T_e}{n_e e^2}\right)^{1/2} \tag{1.1}$$

   where K, T_e and n_e are Boltzmann constant, electron temperature (in kelvins) and electron density respectively. For a system with dimension $L \gg \lambda_D$ whenever local charge concentration arises, or any external fields are introduced into the system, the created electric fields are shielded for a distance smaller than L, leaving the bulk of the plasma free of large electric potentials [49].

2. **Plasma parameter**

   The concept of Debye shielding is only statistically valid if the number of electrons in the charged cloud surrounding the ion is large enough. The number N_D of particles in a "Debye Sphere" is given as [49]

   $$N_D = n\frac{4}{3}\pi\lambda_D^3 = 1.38 \times 10^6 T^{3/2}/n^{1/2} \quad (T \quad in \quad {}^oK) \tag{1.2}$$

   For $N_D \gg 1$, the thermal motion of the particles are important and coupling among the particles is eventually weak, however for $N_D \ll 1$, the coupling between the particles are strong and hence the potential energy of the interacting particles play an important role in interaction dynamics.

3. **Plasma frequency**

   Plasma frequency is one of the fundamental parameter of the plasma. If the electrons are slightly displaced from their equilibrium position, they give rise to the oscillations in the plasma. These displaced electrons experience electrostatic force which tend to pull them back to their original positions. However, due to their inertia, the electrons overshoot and oscillate around their equilibrium position. The frequency of these oscillations is referred to as the plasma frequency, ω_p. The ions can be considered as fixed in space on the time scale of the plasma oscillations. The electron plasma frequency provides the fundamental measure of the plasma density and so the plasma response to external electromagnetic fields. From the first order perturbation theory the frequency of the plasma oscillations is expressed as [49]:

   $$\omega_p = \sqrt{\frac{n_e e^2}{\varepsilon_0 m_e}} \tag{1.3}$$

   where, n_e being electron density, ε_0 is the permittivity in vacuum, e and m_e are charge and mass of the electron.

4. **Criteria for plasmas**

   Fundamentally, there are three criteria for the ionized gas to be termed as plasma. The two of the conditions are already being discussed in the above subsection, firstly $L \gg \lambda_D$ which states that the dimension of the system must be greater than the typical Debye length, and $N_D \gg 1$ i.e., plasma should have a large number of particles within the Debye sphere for the statistical validity of the Debye length. The third and last condition requires $\omega_p \tau > 1$ to behave a charged particle gas like plasma rather than neutrals, where ω_p is plasma frequency, and τ is the mean time between charged particle collisions with neutral atoms [49].

1.2.2 Laser-plasma interaction concept

This section mainly emphasizes on the different physical processes which can be crucial in understanding the interaction of the laser pulses with the plasmas.

1. **Plasma fluid equations**

   Since the typical plasma density is about $\gtrsim 10^{12}$ m^{-3} or higher, so, it would be really difficult to calculate the trajectories of individual particle analytically or computationally. Therefore, instead of calculating the detailed particle trajectories, it is feasible to explain most of the plasma phenomenon by considering the motion of fluid element. Fortunately, this approach is sufficiently accurate to explain the experimentally observed phenomenon [49]. By considering the two species plasma (electrons and ions), we can have the complete set of plasma fluid equations by defining charge and current densities.

$$\rho = n_e q_e + n_i q_i \tag{1.4}$$

$$\mathbf{J} = n_e q_e \mathbf{v}_e + n_i q_i \mathbf{v}_i \tag{1.5}$$

   here $\mathbf{v}_{e,i}$ is the averaged (over Maxwellian) electron and ion velocities. To calculate $\mathbf{E}$ and $\mathbf{B}$, Maxwell's equations are used with momentum conservation, continuity equation and equation of state .

$$\nabla \cdot \mathbf{E} = \frac{1}{\epsilon_0}(n_e q_e + n_i q_i) \tag{1.6}$$

$$\nabla \cdot \mathbf{B} = 0 \tag{1.7}$$

$$\nabla \times \mathbf{E} = \frac{\partial \mathbf{B}}{\partial t} \tag{1.8}$$

$$\nabla \times \mathbf{B} = \mu_0(n_e q_e \mathbf{v}_e + n_i q_i \mathbf{v}_i) + \mu_0 \epsilon_0 \frac{\partial \mathbf{E}}{\partial t} \tag{1.9}$$

$$m_j n_j = \left[\frac{\partial \mathbf{v}_j}{\partial t} + (\mathbf{v}_j \cdot \nabla)\mathbf{v}_j\right] = q_j n_j [\mathbf{E} + \mathbf{v} \times \mathbf{B}] - \nabla p_j \tag{1.10}$$

$$\frac{\partial n_j}{\partial t} + \nabla \cdot (n_j \mathbf{v}_j) = 0 \tag{1.11}$$

$$p_j = C_j n_j^{\gamma_j} \tag{1.12}$$

where $j = e, i$ represents electrons and ions, n_j is electron and ion density, q_j is charge of electron and ion, m_j is mass of electron and ions, p_j is pressure, C_j is constant, γ_j is the ratio of specific heats. These are closed self-consistent set of equations which govern the plasma phenomenon under fluid approximation.

2. **Plasma dispersion relation**

The dispersion relation mainly describes the relation between the wave number ($\mathbf{k}$) and frequency (ω) of the wave, which actually helps in understanding the nature of wave excited. The dispersion relation for an electromagnetic wave propagating in a plasma is the most fundamental starting point in order to understand the laser propagation in plasma. This relation helps to find the group and phase velocity, and also the refractive index of the plasma. Here we consider the electric and magnetic field as $\mathbf{E} = \mathbf{E_0} + \mathbf{E_1}$ and $\mathbf{B} = \mathbf{B_0} + \mathbf{B_1}$, where the components with suffix '1' are first order perturbation to unperturbed values, i.e. suffix '0'. If the plasma is considered to be cold in the absence of any external electric or magnetic fields then relevant Maxwell's equations can be written as:

$$\nabla \times \mathbf{E_1} = -\frac{\partial \mathbf{B_1}}{\partial \mathbf{t}} \tag{1.13}$$

$$c^2 \nabla \times \mathbf{B_1} = \frac{\mathbf{j_1}}{\epsilon_\mathbf{0}} + \frac{\partial \mathbf{E_1}}{\partial \mathbf{t}} \tag{1.14}$$

The time derivative of Eq. 1.14 is written as:

$$c^2 \nabla \times \frac{\partial \mathbf{B_1}}{\partial \mathbf{t}} = \frac{\mathbf{1}}{\epsilon_\mathbf{0}} \frac{\partial \mathbf{j_1}}{\partial \mathbf{t}} + \ddot{\mathbf{E}}_\mathbf{1} \tag{1.15}$$

The curl of Eq. 1.13 results in,

$$\nabla \times (\nabla \times \mathbf{E_1}) = \nabla(\nabla \cdot \mathbf{E_1}) - \nabla^\mathbf{2} \mathbf{E_1} = -\nabla \times \dot{\mathbf{B}}_\mathbf{1} \tag{1.16}$$

From Eqs. 1.15 and 1.16 :

$$-c^2[\nabla(\nabla\cdot\mathbf{E_1})-\nabla^2\mathbf{E_1}]=\frac{\mathbf{1}}{\epsilon_\mathbf{0}}\frac{\partial\mathbf{j_1}}{\partial\mathbf{t}}+\ddot{\mathbf{E_1}} \tag{1.17}$$

Now invoking $\partial/\partial t\rightarrow -i\omega$ and $\partial/\partial x\rightarrow ik$, the above equation reduces to:

$$-c^2[i\mathbf{k}(i\mathbf{k}\cdot\mathbf{E_1})-(ik)^2\mathbf{E_1}]=\frac{(-i\omega)}{\epsilon_0}\mathbf{j_1}+(i\omega)^2\mathbf{E_1} \tag{1.18}$$

$$-\mathbf{k}(\mathbf{k}\cdot\mathbf{E_1})+k^2\mathbf{E_1}=\frac{i\omega}{\epsilon_0 c^2}\mathbf{j_1}+\frac{\omega^2}{c^2}E_1 \tag{1.19}$$

For transverse wave $\mathbf{k}\cdot\mathbf{E_1}=0$, therefore Eq. 1.19 becomes;

$$(\omega^2-c^2k^2)\mathbf{E_1}=-i\omega\mathbf{j_1}/\epsilon_0 \tag{1.20}$$

Assuming the fixed ionic background, the current density $\mathbf{j_1}$ is then given by:

$$\mathbf{j_1}=-n_e e\mathbf{v_{e1}} \tag{1.21}$$

The electron response to the electric field in linerazied term can be written as:

$$m\frac{\partial\mathbf{v_{e1}}}{\partial t}=-e\mathbf{E};\quad \mathbf{v_{e1}}=\frac{e\mathbf{E_1}}{im\omega} \tag{1.22}$$

Substituting Eq. 1.21 and Eq. 1.22 in Eq. 1.20 we get,

$$(\omega^2-c^2k^2)\mathbf{E_1}=\frac{i\omega}{\epsilon_0}n_e e\frac{e\mathbf{E_1}}{im\omega}=\frac{n_e e^2}{\epsilon_0 m}\mathbf{E_1}=\omega_p^2\mathbf{E_1} \tag{1.23}$$

Thus, the desired dispersion relation of an electromagnetic wave propagating in the plasma [49] :

$$\omega^2=\omega_p^2+k^2c^2. \tag{1.24}$$

In the limit of the plasma density $n_e\rightarrow 0$ i.e. $\omega_p\rightarrow 0$, the dispersion relation of electromagnetic waves in vacuum i.e. $\omega^2=k^2c^2$ can be retrieved. It can be understood from this dispersion relation that the electromagnetic waves of frequency say ω can not propagate beyond the point where

$\omega^2 > \omega_p^2$, this would lead to the imaginary propagation vector. We can define the critical density of the plasma for a given electromagnetic waves as $n_c = \omega^2 m\varepsilon_0/e^2$, such that the propagation of the electromagnetic wave is forbidden in the regions when the plasma density $n_e > n_c$ or $n_e/n_c > 1$.

The phase ($v_\phi = \omega/k$) and group ($v_g = d\omega/dk$) velocity of the wave is obtained from the dispersion relation [Eq. 1.24] as follows:

$$v_\phi^2 = \frac{\omega^2}{k^2} = \frac{\omega_p^2}{k^2} + c^2 \tag{1.25}$$

$$v_\phi^2 = \frac{\omega_p^2}{\omega^2} v_\phi^2 + c^2 \tag{1.26}$$

$$v_\phi = \frac{c}{\sqrt{1 - n_e/n_c}} \tag{1.27}$$

where, n_c is the critical density of the plasma for a given electromagnetic wave of frequency ω. Furthermore, the refractive index of the plasma can be defined as:

$$\eta = \frac{c}{v_\phi} = \sqrt{1 - \frac{n_e}{n_c}} \tag{1.28}$$

The group velocity of the electromagnetic waves in the plasma can be obtained as:

$$v_g = \frac{d\omega}{dk} = 2\omega\frac{d\omega}{dk} = 2kc^2 \implies v_g = \frac{c^2}{v_\phi} < c \tag{1.29}$$

It can be observed that the phase velocity of a light wave in a plasma is greater than the speed of light, however, the group velocity will always be less than the speed of light.

3. **Skin Depth**

The dispersion relation in Eq. 1.24 can be written as:

$$k = \frac{\omega}{c}\sqrt{1 - \frac{\omega_p^2}{\omega^2}} \tag{1.30}$$

Let us say, if $\omega_p^2 > \omega^2$, it will be resulted in an imaginary wave propagation vector indicating the attenuation of the electromagnetic waves. If the electric field component of the EM wave is expressed as:

$$\mathbf{E_1} = E_1 \exp[i(kx - \omega t)]\hat{z} \tag{1.31}$$

$$\mathbf{E_1} = E_1 \exp[ikx] \exp[-i\omega t]\hat{z} \tag{1.32}$$

it can be comprehended from the above equation that for $k \to ik$ the field amplitude of the wave would attenuate exponentially. The skin depth is defined as the distance or depth into the plasma wherein the fields would decay to $\exp[-1]$ to its vacuum value, which is given as:

$$\delta = \frac{1}{|k|} = \frac{c}{(\omega_p^2 - \omega^2)^{1/2}} \tag{1.33}$$

4. **Ponderomotive force**

A ponderomotive force is a nonlinear force that arises due to the spatial inhomogeneity of the laser intensity. It can be derived by considering the motion of an electron in oscillating, spatially inhomogeneous electromagnetic fields of the wave. Considering the monochromatic electromagnetic field given by,

$$\mathbf{E}(\mathbf{r}, t) = \mathbf{E_s}(\mathbf{r})\ \cos\omega t \tag{1.34}$$

$$\frac{\partial\, \mathbf{B}(\mathbf{r}, t)}{\partial t} = -c\, \nabla \times \mathbf{E}(\mathbf{r}, t) \tag{1.35}$$

$$\therefore \mathbf{B}(\mathbf{r}, t) = -\frac{c}{\omega}\ \nabla \times \mathbf{E_s}(\mathbf{r})\ \sin\omega t = \mathbf{B_s}(\mathbf{r})\ \sin\omega t \tag{1.36}$$

where, $\mathbf{E_s}(\mathbf{r})$ is the space-dependent component of the electric field and ω is the angular frequency of the field. The Lorentz force for an electron moving in these fields is then given by,

$$m_e\frac{d\mathbf{v}}{dt} = -e\left[\mathbf{E}(\mathbf{r}, t) + \frac{\mathbf{v}}{c}\ \times \mathbf{B}(\mathbf{r}, t)\right], \quad \mathbf{v} = \frac{d\mathbf{r}}{dt} \tag{1.37}$$

For the non-relativistic electrons ($\mathbf{v}/c \lll 1$) the second term is smaller as compared to the first one. In this case, to the first order perturbation ($\mathbf{v} = \mathbf{v_1}, \mathbf{r} = \mathbf{r_1}$), electrons will oscillate in the direction of $\mathbf{E}$, and one has to solve,

$$m_e \frac{d\mathbf{v_1}}{dt} + e\,\mathbf{E}(\mathbf{r_0}, t) = 0$$

$$m_e \frac{d\mathbf{v_1}}{dt} + e\,\mathbf{E_s}(\mathbf{r_0})\ \cos\omega t = 0, \quad \mathbf{v_1} = \frac{d\mathbf{r_1}}{dt}. \tag{1.38}$$

The solutions of these equations are given by,

$$\mathbf{v_1} = \frac{-e\,\mathbf{E_s}(\mathbf{r_0})\ \sin\omega t}{m_e\omega}, \quad \mathbf{r_1} = \frac{e\,\mathbf{E_s}(\mathbf{r_0})\ \cos\omega t}{m_e\omega^2}. \tag{1.39}$$

For the second-order accuracy, we consider,

$$\mathbf{v} = \mathbf{v_1} + \mathbf{v_2}, \quad \mathbf{E_s} = \mathbf{E_s}(\mathbf{r_0}) + (\mathbf{r_1}\cdot\nabla)\mathbf{E_s}(\mathbf{r} = \mathbf{r_0}), \quad \mathbf{B_s} = \mathbf{B_s}(\mathbf{r_0}). \tag{1.40}$$

Substituting Eqs. 1.38 and 1.40 into Eq. 1.37 we get the second order equation,

$$m_e \frac{d\mathbf{v_2}}{dt} = -e\left[(\mathbf{r_1}\cdot\nabla)\mathbf{E_s}(\mathbf{r_0})\cos\omega t + \frac{\mathbf{v_1}\times\mathbf{B_s}(\mathbf{r_0})\sin\omega t}{c}\right]. \tag{1.41}$$

The non-linear force $\mathbf{F_{NL}}$ acting on an electron is calculated by substituting Eqs. 1.39 and 1.36 in Eq. 1.41 and averaging over time [1] and is given by:

$$\mathbf{F_{NL}} = m_e\left\langle \frac{d\mathbf{v_2}}{dt}\right\rangle = \frac{-e^2}{2m_e\omega^2}[(\mathbf{E_s}\cdot\nabla)\mathbf{E_s} + \mathbf{E_s}\times(\nabla\times\mathbf{E_s})]. \tag{1.42}$$

The first term on the right-hand side of Eq. 1.42 is the force which causes the electron to move in a linear trajectory, while the second term on the right-hand side is the $\mathbf{E}\times\mathbf{B}$ force acting on the electron and distorts the linear motion. Using the following vector identity,

$$\mathbf{N}\times(\nabla\times\mathbf{N}) = \frac{1}{2}\nabla\mathbf{N}^2 - (\mathbf{N}\cdot\nabla)\mathbf{N}$$

---

[1] $\langle\sin^2\omega t\rangle = \langle\cos^2\omega t\rangle = 1/2$, $\langle\sin\,\omega t\ \times\cos\,\omega t\rangle = 0$, here $\langle\cdots\rangle$ represents the time average.

in Eq. 1.42 the ponderomotive force per unit volume is then obtained as,

$$\mathbf{f_p} = n_e \mathbf{F_{NL}} = -\frac{n_e e^2}{4 m_e \omega^2} \nabla \mathbf{E_s^2}. \tag{1.43}$$

Eq. 1.43 represents that a charged particle in an inhomogeneous oscillating field oscillates at the frequency of ω as well as drifts toward the weak field area. It is noteworthy that in this rare case, the sign of the particle charge does not change the direction of the force, unlike the Lorentz force.

5. **J × B Heating**

For higher intensities the nonlinear oscillations in the case of normal incidence may be driven by the magnetic force component of Lorentz force. The oscillating components leads to the oscillatory motion of the electrons, termed as $\mathbf{J} \times \mathbf{B}$ heating. Considering a linearly polarized light, the ponderomotive force component is expressed as [50]

$$\mathbf{f_p} = -\frac{m}{4} \frac{\partial v_l^2(x)}{\partial x} [1 - \cos(2\omega t)] \tag{1.44}$$

where v_l is the electron quiver velocity and ω is the laser frequency. The first term corresponds to the density gradient of the electrons in the forward direction, and the second term is for the $\mathbf{J} \times \mathbf{B}$ components which oscillate at twice the laser frequency along the direction of the laser propagation.

1.3 Application of Laser-Plasma Interaction

There are numerous potential applications for laser-accelerated ion beams, however their unique properties make them particularly interesting in areas such as cancer treatment [7], radiography [3] and fast ignition Inertial Confinement Fusion (ICF) [51]. The paramount application of laser-plasma interactions with immediate implication to the society is in the field of medicine. Since the past decade, there has been an exponential growth in the number of patients diagnosed with cancer. The use of radiotherapy technique to cure or restrict the growth of the cancer is proved to be effective treatment tool, as it uses not only high energy ions but also π-mesons, electrons, neutron, x-rays and also gamma-rays.

The first theory related to hadron therapy was proposed by Wilson in 1946 [52] for cancer treatment through ions and neutrons. Hadron therapy uses protons and higher mass ions for irradiation to the tumors, according to the irradiation dose as predicted by the so called *bragg peak* [53]. The energy deposition probability of ions at some given location (which depends on the energy of the ion beam) is more than the conventional radiation sources. The energy of the ion beams can be deposited directly at the location where the cancerous cells are present, without harming the healthy tissues. The conventional radio frequency based linear accelerators are expensive, large scale and difficult to maintain. In view of this, the alternate laser-based accelerators were proposed for high energy ion beam production [3, 7, 8]. Laser based particle accelerators are cost effective and compact, which can be installed in the basement of any hospital. The proton beam of $\gtrsim 250$ MeV is necessary for the treatment of tumors according to the Bragg peak measurement criteria. The advancement in the field of ion acceleration have resulted in the laser based high energetic proton beam production [4, 10, 54–56].

Highly energetic proton beams as a source of radiography tool were used to probe objects and study the density fluctuations [57, 58]. Similarly, using laser-plasma interaction to generate proton beam source for imaging applications was demonstrated by [59]. The method of proton radiography is also aimed to measure the radiations generated from the plastic foil when irradiated by a laser of intensity $10^{14} W/cm^2$ [60]. Proton radiography is also implemented in TNSA mechanism as well, where the high quality proton beam probes the sheath field and the target expansion [61]. The usage of the proton radiography also includes the probing of plasma channel [62, 63], resolving collisionless shock wave [64], radioisotope production [65], neutron production [11, 66], observing the fast magnetic field [67] and many more.

In Inertial Confinement Fusion (ICF), Deuterium and Tritium (D-T) filled capsule is compressed in a very short amount of time to release large energy through nuclear fusion. The first demonstration of ICF with the laser was done in the early 1970s [68]. Another approach for ICF was also demonstrated, wherein the inner surface of the metal cylinder (hohlrum) which contained the D-T capsule was irradiated by the lasers [69]. The absorbed laser energy from the cylinder walls was converted into the x-rays. The fuel in the capsule was compressed by these x-rays resulting in nuclear fusion of D-T capsule. However, this approach suffers hydrodynamic instabilities thus making it highly difficult to sustain [69]. A new concept of fast ignition (FI) for ICF was proposed by Tabak et al. [70] where, ignition is driven by the separate laser pulse, and compression was achieved by several laser pulses by creating a hot spot in a much shorter time. The use of conical targets [71, 72], Deuterium and Beryllium targets [73] for proton based Fast Ignition (FI) is also reported in the literature. A detailed review on ion beam based FI can be found in Ref. [51].

1.4 Overview of the Thesis

After a brief introduction of some important concepts in the field of laser-plasma interaction, in the following, we present an overview of the work we have carried out in this thesis. All quantities are in dimensionless units and are defined as follows:

- Space and time are normalized in terms of laser wavelength and laser cycle respectively,

$$x' = x/\lambda; \quad t' = t/\tau \tag{1.45}$$

- Velocities are scaled to velocity of light in vacuum,

$$\mathbf{v}' = \mathbf{v}/c \tag{1.46}$$

- Particle masses are in terms of electron mass,

$$m' = m/m_e \tag{1.47}$$

- Electric and magnetic fields are scaled as,

$$a \equiv \mathbf{E}' = e\mathbf{E}/m_e\omega c; \quad \mathbf{B}' = e\mathbf{B}/m_e c \tag{1.48}$$

- Potentials are scaled as,

$$\mathbf{A}' = e\mathbf{A}/m_e c; \quad \phi' = e\phi/m_e c^2 \tag{1.49}$$

- Densities are defined in terms of critical density $n_c = \omega^2 \epsilon_0 m_e/e^2$

$$n' = n/n_c \tag{1.50}$$

1.4.1 Ion Acceleration by Relativistic Self-Induced Transparency Mechanism

In order to efficiently accelerate the ions to ultrarelativistic energies, the use of a multilayer or multi-species target is examined in Refs. [74–78]. The laser-driven ion acceleration in the RSIT regime is also proving to be a feasible way to accelerate ions to the relativistic energies [79, 80]. In this regime, an ultraintense laser beam manifests the increase of effective mass of electrons through relativistic effects, which effectively lowers the critical density of the plasma, making the target transparent to the laser of particular intensity [11, 81–84]. The ion and neutron beams with energies around $\sim$ 180 MeV have also been observed in experiments [11, 82].

The interaction of a circularly polarized intense laser beam with the subwavelength target in the RSIT regime can quickly push all the electrons away, leaving behind only the ions. These ions can undergo coulomb explosion with 100% energy spread, which is not at all the desired outcome. In this work, we have studied the effect of target thickness on RSIT. It was observed that, for subwavelength targets, the corresponding threshold target density (beyond which the target is opaque to an incident laser pulse of given intensity) increases. The accelerating longitudinal electrostatic field created by RSIT from the subwavelength target is then used to accelerate the ions from a thin, low-density layer behind the main target to $\sim$ 100 MeV. It was also observed that, the energy spectrum of an extra low-density layer is more advantageous rather than relying only on target ions [85].

In Refs. [75–78, 86] they have examined the use of a multilayer or multi-species target in order to efficiently accelerate the ions to ultra-relativistic energies. The acceleration of protons to ~ 210 MeV by a laser with peak intensity 2.7×10^{22} W/cm^2, using double-layered thin foil is studied in Ref. [87], in Directed Coulomb Explosion (DCE) regime, where the high intense laser beam interacts with very high density Al^{13+} plasma ($\sim 400\ n_c$). As a consequence, all the electrons are expelled from the target and ions undergo Coulomb explosion. The adjacent proton layer of $30n_c$ is then accelerated by the electrostatic fields created by DCE. Furthermore, it was observed that for accessing the similar energy range, the laser intensities required by RSIT is around 2.5 times less than that in an LS (Light-Sail) or RPA (Radiation Pressure Acceleration) regime.

1.4.2 Chirp Assisted Ion Acceleration Through Relativistic Self-Induced Transparency

As we have already discussed, the laser-driven ion acceleration by using RSIT regime provides an efficient ion acceleration on a composite two-layer target. The electrostatic field created behind the primary layer is responsible for accelerating the ions from the thin low-density secondary layer as a mono-energetic bunch. To further elucidate on this aspect, the introduction of the chirp in the laser pulse proved to be a promising way to efficiently accelerate the ions from the secondary layer. In the chirped pulses, the pulse frequency has temporal variation about its fundamental frequency, which manifests in the temporal dependence of the critical density n_c. In this study, the aim is to characterize the effect of laser pulse chirp on the ion energies under RSIT regime. A chirp model which is beyond the linear approximation [88] is considered, that have a close analogy with the Chirped Pulse Amplification technique. In order to understand how the chirp of the laser pulse affects the transmission through the target, a simplified wave propagation model for the laser with $a_0 < 1$ is developed. The model takes into account the chirp of the pulse while calculating the target density as pulse traverses the target. The results of this simplified wave propagation are found to be consistent with the 1D PIC simulation [89]. Furthermore, the dual layer sub-wavelength target is considered, in order to have a very efficient generation of the accelerated ion bunch from the secondary layer [90–92]. The feasibility of the proposed scheme under experimental scenario needs full 3D Particle-in-Cell simulations.

1.4.3 Laser Pulse Dispersion in Underdense Plasma and Associated Ion Acceleration

The propagation of the laser pulses in the underdense plasma is a very crucial aspect of laser-plasma interaction process. The high contrast laser pulses are desirable for the studies involving the interaction with the thin foil targets, however, the prepulse of those high power lasers is intense enough to ionize the target before the arrival of the main pulse [93]. The ionization of the target and the formation of the plasma ahead of the main target has very dramatic consequences which in a sense can completely alter the dynamics of the interaction.

The study of the evolution of the laser pulse as it propagates in the tenuous plasma has drawn considerable research interest around the globe both theoretically and experimentally [94–97]. The propagation of the laser pulse in the under-dense plasma ($n_e < n_c$) has been studied in the past [96, 98]. The effect of the polarization on the dynamics of the laser-plasma interaction has been reported in Ref. [99]. The influence of the magnetic field on the propagation of the laser in the plasma is discussed in Ref. [100]. The generation of the magnetic fields during intense laser channeling in underdense plasma has been reported in Ref. [101]. The propagation of the laser or electromagnetic pulses in plasma also leads to a non-linear phenomenon resulting in the soliton formations [21, 102]. The existence of the solitary waves in the plasma and its effect on the laser pulse itself is reported in Ref. [103]. The wakefield generation is also one of the most important phenomenon as a consequence of the laser pulse propagation in the under-dense plasma [104]. As the plasma density approaches the critical density n_c, the wakefield generation is suppressed, and instead, laser undergoes nonlinear self-modulation [105]. A nonlinear fluid theory for the intense laser-plasma interaction have been reported by Sprangle et. al. [106, 107], where the relativistic optical guiding, coherent harmonic generation, nonlinear plasma wakefield generation are discussed in great detail. In Ref. [108], the nonlinear group velocity of a laser pulse propagating in a cold underdense unmagnetized plasma is reported for various pulse length regimes.

In order to understand the evolution of laser pulse as it propagates in an underdense plasma for $a_0 < 1$ case, a cold relativistic fluid model is used, wherein apart from immobile ions no further approximations are made. We have numerically solved the fluid equations in space and time, avoiding the Quasi Static Approximations generally used in the fluid simulations [106, 107]. However, the evolution of the ultraintense ($a_0 > 1$) laser pulses is studied by PIC simulation only. The effect of the laser pulse amplitude, pulse duration, and plasma density is studied using the fluid model and compared with the expected scaling laws and also with the PIC simulation. The delicate interplay between the conversion from the electromagnetic field energy to the longitudinal electrostatic fields results in the dispersion and so the red-shift of the pump laser pulse. Along with it, the interaction of the dispersed pulse (after the propagation in underdense plasma) with the sub-wavelength two-layer composite target have efficiently accelerated secondary layer ions to ~ 170 MeV.

1.5 Thesis Framework

In this thesis, we have studied the ion acceleration from plasma surface when irradiated with ultraintense laser pulse by using RSIT. The work is comprised of theoretical and computational studies. The thesis addresses three problems, first of all the necessity to use two-layer composite target geometry for the ion acceleration, next the use of chirped laser pulses on the similar double layer target configuration and last the propagation of laser pulse in underdense plasma and ion acceleration via dispersed laser pulses.

The thesis is organized as follows. After the brief introduction to the subject in the Chapter 1, the Chapter 2 is devoted to the detailed discussion about the various acceleration mechanisms. Next, Chapter 3 focuses on ion acceleration from a thin, low density secondary layer via RSIT, where the electrostatic field created behind the primary layer is responsible for accelerating ions from the rear surface of the composite double layer target. Subsequently, in Chapter 4 the effect of chirped laser pulse on the transmission of laser pulse is studied using cold relativistic fluid model and compared with the PIC simulation. Chapter 5 discusses the dispersion of laser pulse as it propagates in underdense plasma and ion acceleration from these dispersed laser pulses. Furthermore, the Summary of the work done and future scopes are presented in Chapter 6. The thesis comprises of three Appendix sections. The cold fluid model for RSIT mechanism and for wave propagation in underdense plasma are discussed in Appendix A and B respectively. Details of the PIC simulations are presented in Appendix C.

CHAPTER 2

Laser Plasma Induced Particle Acceleration Mechanisms

In this chapter, we will be discussing the various mechanisms for the charged particle acceleration. The prominence of the individual acceleration mechanism depends on the laser and the target parameters, such as laser pulse amplitude, target thickness, and the density. The interaction of ultraintense and ultrashort laser pulse with more innovative targets have resulted in acceleration of the particles to the energies in the range of GeVs [12, 14, 109]. Such high energetic particles are of great significance in the field of medicines; confinement fusion, etc. The role of these applications are discussed in Section 1.3.

2.1 Electron Acceleration Mechanisms

The efforts in the field of laser plasma accelerator were initiated with the notable work of Tajima and Dawson in 1979 [2]. A boost in high energy electron bunches was seen with the development of chirped pulse amplification technique (CPA). The fundamental principle to accelerate the electrons or ions is the generation of the electrostatic field. With the optimized laser and plasma parameters, the high-quality electron bunches were realized in Ref. [110, 111]. There are several electron acceleration mechanisms such as Plasma Wakefield Acceleration (PWFA) [112], laser wakefield acceleration (LWFA) [2] and self-modulated laser wakefield acceleration (SM-LWFA)[113, 114].

2.1.1 Laser Wakefield Acceleration (LWFA)

The propagation of the short and intense laser pulse in an underdense plasma ($n_e/n_c \ll 1$) with the group velocity ($v_g = c\sqrt{1 - n_e/n_c} \simeq c$), results in a ponderomotive push on the electrons, as a result, they are expelled out of the region of the laser pulse. The removal of the electrons from the propagation path of the laser causes the bunching of the electrons behind the laser pulse, which eventually manifests in the longitudinal electrostatic fields, referred as *wakes*. The phase velocity of the wakes is almost equal to the group velocity ($v_\phi = v_g \simeq c$) for underdense plasmas. Since the ponderomotive force of laser pulse has both the leading and lagging edge, it is appropriate to have a pulse duration close to the plasma oscillation i.e., $\tau_L \simeq \tau_P$ ($\tau_p \equiv 2\pi/\omega_p$) for efficient excitation of the plasma wakes. In other words, the most efficient wakefield acceleration will occur when the laser pulse length is comparable to the plasma wavelength $c\tau_L \sim \lambda_p$ while interacting with the underdense plasma.

The nonlinear theory of 1D and 2D wakefield excitation and the generation of the accelerating gradient of the order 100 GeV/m are reported in Refs. [107, 113, 115]. In the last decade, due to the generation of the energetic electrons with high quality bunches were obtained as a result of optimization of the laser and plasma parameters [116]. The use of plasma channel guided laser, self-focusing or particle injection method [14, 110, 117] have helped in obtaining narrow energy spread [116] and high quality electron bunches with tunable energies. Various types of plasma accelerator schemes such as hollow channel [118], bubble regime [119] and blow-out wakefield regime have also been studied to excite plasma wakes and wavebreaking [120, 121].

The injection of electrons into the plasma wave can be done by trapping of background hot electrons in the wake, or by longitudinal/transverse wavebreaking [120–123]. To control the process of electron injection experimentally, the external electron source is required (as RF guns) [124]. The study using internal electron of the plasma itself is found to be feasible for controlling the injection of electrons using counter-propagating laser pulse [125]. In this scheme, the two laser pulses are used, first one (Pump pulse) for exciting the wake and second pulse (injection pulse) to heat electrons during a collision with pump pulse. This results in trapping and acceleration of electrons in the wakefield [111]. Another way to control electron injection relies on downward density ramp as stated in Ref. [117], where plasma wave slows down at density ramp thereby causing a low threshold for trapping the plasma background electrons and causing wave-breaking of the wakefield [126]. A recently proposed scheme based on the large difference between ionization states of the atom too provides the control electron injection [127].

2.1.2 Self Modulated Laser Wakefield Acceleration (SMLWFA)

The development of table top set up for generating ultrashort laser pulse have influenced the growth in LWFA and SMLWFA electron acceleration mechanism. The SMLWFA [113, 114] has a close analogy with Forward Raman Scattering, where an electromagnetic wave $(\omega, \mathbf{k})$ decomposes into plasma wave $(\omega_p, \mathbf{k_p})$ and another forward-propagating light wave at a frequency shift of ω_p i.e., $(\omega - \omega_p, \mathbf{k} - \mathbf{k_p})$. The regime of SMLWFA occurs when laser pulse duration τ_L is larger than the plasma period τ_p . The group velocity of the laser pulse is influenced by electron density perturbation. Due to which, the laser pulse that propagates in plasma will slow down near density maximum and results in bunching. Now, as the bunching of the light and plasma density perturbation are $\pi/2$ out of phase, so the ponderomotive force of the bunched laser pulse reinforces the original density perturbation [128]. The self modulated wakefield can produce a much larger accelerating field than the standard LWFA, due to the scale in maximum longitudinal electric field. The accelerated electron energy achieved by SMLWFA mechanism are of the orders of ~ 100 MeV [122, 123, 129].

2.2 Ion Acceleration Mechanisms

The quest for obtaining high particle energies have resulted in the evolution of different design concept of the particle accelerators for both electrons and the ions. The significant boost in the field of ion acceleration is seen over the last couple of decades. The proton beams with multi-MeV energy as a result of ultraintense laser interaction with the solid targets was reported in Refs. [15, 130, 131]. Different types of ion acceleration mechanisms have been proposed depending on the laser and target conditions, such as Target Normal Sheath Acceleration (TNSA), Radiation Pressure Acceleration (RPA), Breakout Afterburner (BOA), Relativistic Self-Induced Transparency (RSIT) to name the few. In the following, we discuss various mechanisms responsible for ion acceleration.

2.2.1 Target Normal Sheath Acceleration (TNSA)

The TNSA is the most widely studied ion acceleration mechanism both theoretically and experimentally [16]. TNSA is mainly responsible for the acceleration in the intensity range of 10^{18} to 10^{20} W/cm^2 for a pulse duration of 1 ps to 50 fs and with layered target [132, 133]. When a high-intensity laser interacts with the target, it produces a cloud of hot electrons, generated by the blow-off plasma. These high energy electrons go through the target and ionize the hydrogen layer on the back of target which originates from a thin (~ 50Å) layer of contaminant, which is always present in the experiments. This was attributed to ever-present water vapour in the target chamber or a hydrocarbon layer due to the vacuum pump oil. These hydrogen ions then pulled off the surface by this cloud of electrons, and accelerated to tens of MeV, in tens of μm. The schematic diagram for the TNSA mechanism is shown in Fig. 2.1. The laser prepulse hits the front of the target creating an expanding plasma. Then the main laser pulse comes and interacts with plasma, generating a large number of hot electrons (electron cloud) at the critical surface. Since the target is transparent to these energetic electrons, the cloud extends past the back of the target, whereupon it ionizes and then accelerates the hydrogen layer. The energy of ions is decided by the intensity of the laser, and hence the energy of the electrons. The target must be thick enough so that the back surface remains unperturbed by the laser prepulse, yet thin enough for the electrons to penetrate through the solid slab of material.

Several models have been proposed and studied to analyze the TNSA mechanism. The physical process of TNSA mechanism involves complexities such as front surface laser pulse energy absorption, fast electron production as well as transport within the target and sheath evolution dependence. One of the most widely used TNSA model is "Plasma Expansion Model". A simple analytical model was proposed by Wilks et al [16], where it was assumed that the electrons from the front surface are transported through the back of the target surface. The electric field acting on ions was given by $E = T_{hot}/eL_n$,

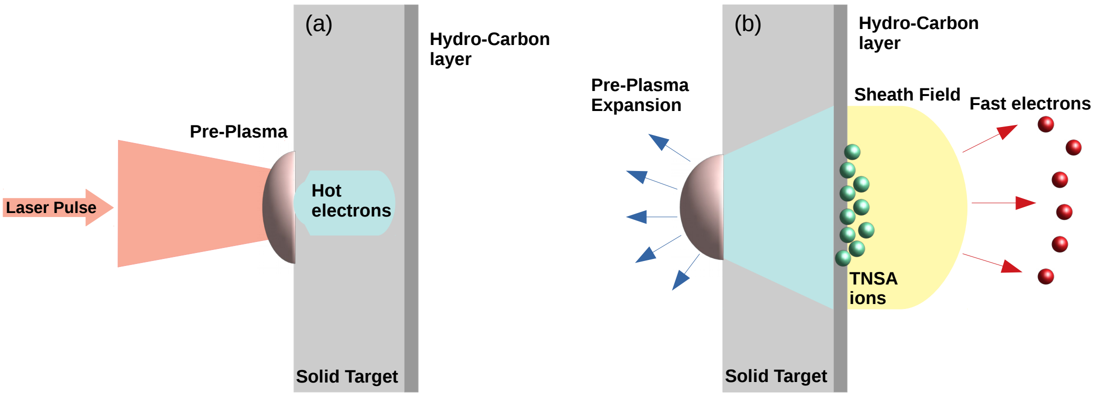
(a)
Hydro-Carbon layer
Pre-Plasma
Laser Pulse
Hot electrons
Solid Target
(b)
Hydro-Carbon layer
Pre-Plasma Expansion
Sheath Field
Fast electrons
TNSA ions
Solid Target

Figure 2.1: *The schematic diagram of target normal sheath acceleration mechanism. (a) when laser pulse irradiates the front surface of the solid target, accelerating fast electrons and propagate through to the rear surface. (b) The electrostatic field produced is strong enough to ionise the target surface and accelerate the ions. Also, the front surface ion acceleration occurs mainly due to the expansion of the laser-generated plasma.*

where $T_{hot} = mc^2(1 + 2U_p/mc^2)^{1/2}$ is the hot electron temperature (resembles the Maxwellian distribution) which is scaled through ponderomotive potential U_p and L_n is the plasma scale length. For short density scale length, a high acceleration gradient is achieved by an ultrashort pulse in comparison to the front surface where scale length is in few hundreds of μm. A more accurate model was proposed by Mora [134] which uses collisionless plasma expansion. It was assumed to have cold ions, initially at rest and an electron density n_e following Boltzmann distribution. Further using a fluid set of equations (i.e., Poisson's equation, the equation of motion and continuity equation) the ion front electric field, position and velocity were deduced.

$$E_{front} \simeq \frac{2E_0}{\sqrt{2\exp(1) + \Omega_p^2 t^2}} \tag{2.1}$$

Integrating Eq. 2.1 using $dv_{front}/dt = ZeE_{front}/m_i$ results in ion front velocity as:

$$v_{front} \simeq 2C_s \ln \tau + \sqrt{\tau^2 + 1} \tag{2.2}$$

and position; where $\tau = \Omega_p t/\sqrt{2exp(1)}$

$$x_{front} \simeq 2\sqrt{2e}\lambda_D[\tau \ln(\tau + \sqrt{\tau^2 + 1} - \sqrt{\tau^2 + 1} + 1)] \tag{2.3}$$

The maximum energy predicted by the model was

$$\mathcal{E} = 2ZT_e(\ln\tau + \sqrt{\tau^2+1})^2 \tag{2.4}$$

and the exponential decrease in the energy spectrum was calculated as:

$$\frac{dN}{d\mathcal{E}} = \left(\frac{n_i C_s t}{\sqrt{2ZT_e\mathcal{E}}}\right) exp\left(-\frac{2\mathcal{E}}{ZT_e}\right) \tag{2.5}$$

where, $K_BT_e \longrightarrow T_e$, $E_0 = \sqrt{n_0T_e/\epsilon_0}$, $\Omega_p = \sqrt{n_0e^2/\epsilon_0 m_i}$, $\lambda_D = \sqrt{\epsilon_0T_e/n_0e^2}$, $C_s = \sqrt{ZT_e/m_i}$, $\mathcal{E}$ is ion energy, m_i is ion mass, e electron charge, T_e electron temperature, Z ion charge number, t accelerating time, Ω_p ion plasma frequency, λ_D debye length, C_s sound speed, ϵ_0 is the permittivity, and n_0 is electron density. Experimental results are very well fitted using this model. Although there were some limitations to the model such as, (1) need of proper hot electron temperature estimation, (2) overestimation of the maximum cut-off energy for longer pulse duration and (3) plasma approximation $n_i \simeq n_e$ is taken at the rear side (which is dependent on the front surface hot electron density (n_e)).

Therefore, other methods and scaling laws were proposed to study the dependence of laser pulse duration (τ_l) on acceleration time (t) as $t = 1.3\tau_l$ was stated in Ref. [135]. The hot electron temperature dependence for relativistic ($a_0 \geq 1$) and non-relativistic ($a_0 \leq 1$) laser pulse amplitudes were studied in Refs. [136–138]. The hot electron re-circulation which plays a paramount role in increased duration of the accelerating field in TNSA is discussed in Refs. [139, 140].

Another "quasi-static field approach" was reported in Refs. [93, 141] in which electrons were confined in a bunch of length $c\tau_L$ at the rear side and considered to be transversely spread over a circular region of sheath radius r_{sheath}.

$$r_{sheath} = r_L + tan(\theta/2) \tag{2.6}$$

where, r_L is the laser focal spot radius and θ as expansion cone angle, thus the average electron density $n_{(e,0)}$ at the rear side is given by:

$$n_{(e,0)} = \frac{N_e}{c\tau_L\pi(r_{sheath})^2} \tag{2.7}$$

here $N_e \sim \eta E_L/k_B T_e$ is hot electron density propagating through the target, E_L is laser pulse energy, η is conversion efficiency, T_e is electron temperature. For laser energy conversion to the hot electron energy the maximum energy gain of the ion cloud $\mathcal{E}_i$ is;

$$\mathcal{E}_i = q_i 2mc^2 \left(\frac{\eta P_L}{P_R}\right)^{1/2} \tag{2.8}$$

where q_i is ion charge, P_L is laser power and $P_R = mc^3/r_e \sim$ 8.17 GW is relativistic power unit with r_e is electron radius. The model is efficient to predict experimentally obtained ion energies only for laser intensities in the range $10^{18} W/cm^2$ to $5 \times 10^{19} W/cm^2$.

A "hybrid PIC model" [132] was proposed which uses the analytical approach with Vlasov simulation to study the effect of proton density on the proton spectrum. The maximum proton energy estimated was in good agreement with experimental data, with a bit of discrepancy for longer pulses (> 1 ps).

The ion beam characteristics from TNSA have been explored both experimentally [15, 93, 130, 133, 142–144] and theoretically [132, 134, 138, 145, 146]. The rear surface ion acceleration was studied in Refs. [15, 147–149] along with a few reports suggesting the front surface acceleration in Refs. [130, 131, 150]. The experimental group of Allen et al. [151] reported that the acceleration occurs from both front and the rear surface of the target. However, the dominance of ion acceleration prevailed from the back surface as reported in Refs. [152, 153].

Similarly removal of the contamination layer from the target rear by preheating the target also showed that multiple ion species could be accelerated to produce high energetic ion beam [154, 155]. The quasi-monenergetic beam with narrow energy spread, low emittance are reported in Refs. [156]. The proton acceleration dependence on acceleration time [135], sheath radius [93, 152], effect of prepulse [93], beam divergence (bell shaped) [61], grooving targets [157], layered target [133] and the use of metallic mesh placement at a given distance also characterized the generated proton beam [59].

Scaling laws for the energy per nucleon $\mathcal{E}_n$ with laser and target parameters particularly with the laser pulse energy (U_L) and intensity (I_L) is of fundamental importance to evaluate the potential of TNSA based schemes for applications. The scaling law exhibited the production of more energetic dependence on the laser pulse duration(τ_L) and intensity (I_L) [143]. Few scaling laws were also given by reviewing the experimental data as well in Refs. [158, 159].

2.2.2 Radiation Pressure Acceleration (RPA)

The distinctive study of ion acceleration with intensity ranging above $10^{20} W/cm^2$ and upto $10^{23} W/cm^2$ [160] is done using Radiation Pressure Acceleration mechanism. This mechanism of ion acceleration is purely related to the formation of an electrostatic field due to the action of the laser ponderomotive force on electrons, and consequently, on the ions via space charge displacement. The radiation pressure P_{rad} exerted by the laser of intensity I on the non-transparent medium is given by:

$$P_{rad} = (1 + R - T)\frac{I}{c} \tag{2.9}$$

where, R and T are the reflection and transmission coefficients respectively. The maximum (minimum) radiation pressure that can be obtained for a solid target with zero transmission (reflection) is given as $P_{rad} = 2I_L/c$ (P_{rad} = 0). Although RPA is reported for linearly polarized laser pulse in [160], however the mechanism mainly dominates for the circularly polarized laser pulse. This is because the circularly polarized pulse suppresses the $\mathbf{J} \times \mathbf{B}$ heating [Section 5], as a result the electrons are pushed deeper into the target, creating stable electrostatic field. The mechanism is subdivided into two modes depending on the target thickness namely "Hole-Boring" for thick targets (i.e. much thicker than the skin layer, where ion acceleration occurs due to space-charge field) and "Light Sail" for thin targets (i.e. object of finite inertia having large surface and low mass) shown in Fig. 2.2.

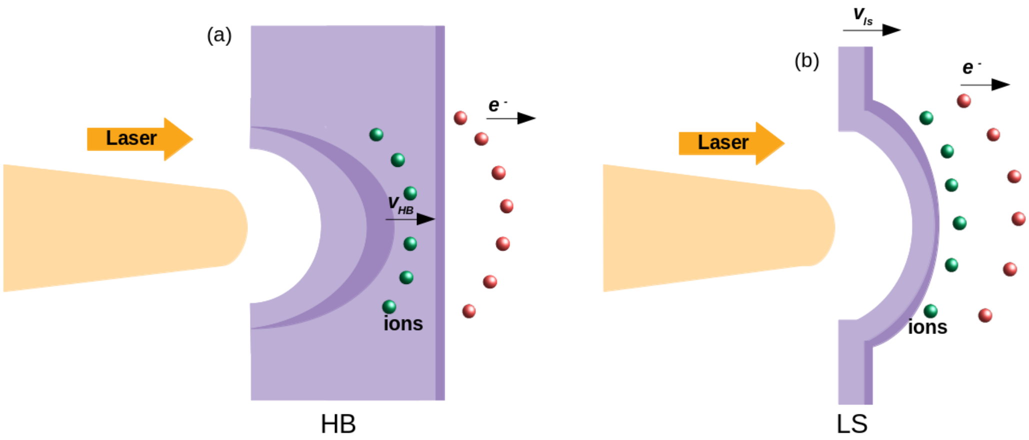

Figure 2.2: *Diagrammatic illustration of Hole boring regime for thick targets (a) and light sail regime for thin targets (b) in radiation pressure acceleration.*

Hole Boring

In hole boring as the name suggests the high intensity circularly polarized laser pulse when interacts with the thick overdense target, pushes the electron like a piston (or "bores the hole"). These electrons pile up at the front of the laser pulse, resulting in the steeping of the electron density profile. A charge separation is built up between immobile ions and electrons leading to the formation of strong electrostatic field.

In non relativistic theory, the hole boring velocity v_{HB} (ion front velocity) is obtained by balancing the momentum flux with radiation pressure [161, 162].

$$\frac{v_{HB}}{c} = \sqrt{\frac{n_c Z m_e}{2 n_e m_i}} a_0 \tag{2.10}$$

here, n_c is the critical density, n_e electron density, $m_e(m_i)$ is electron (ion) mass, Z is charge state, $a_0 = eE/m_e \omega c$ is normalized laser pulse amplitude. In a relativistically correct HB [23], the most significant assumption was that the laser intensity in instantaneous rest frame of the piston and lab frame are not equal, as a result relativistically corrected hole boring velocity and maximum ion energy are given by:

$$\frac{v_{HB}}{c} = \frac{\sqrt{\Xi}}{1+\sqrt{\Xi}}; \quad \Xi = \frac{I_L}{m_i n_i c^3} \tag{2.11}$$

$$\mathcal{E} = m_i c^2 \left(\frac{2\Xi}{1 + 2\sqrt{\Xi}} \right) \tag{2.12}$$

For $\Xi \ll 1$ and $v_{HB} \ll c$, one can obtain $v_{HB}/c \sim \sqrt{\Xi}$ and $\mathcal{E} \sim 2m_i c^2 \Xi$ in non relativistic regime. The first detailed HB using kinetic simulation was studied in Ref. [163], and a decade later was implemented for ICF targets [164]. The studies including different types of lasers [26, 165], gas jets [166], foam targets [167]and use of preplasma production etc are used to enhance maximum proton energy in HB-RPA.

Light Sail

In light sail regime "thin" target of few microns is accelerated as a whole due to the laser radiation pressure. The radiation pressure is balanced by the longitudinal electrostatic fields, as a result the complete mass of the target is accelerated as a whole. Ion acceleration for LS regime is more effective than in case of HB regime. The idea of LS regime came into picture when Esirkepov et al [160] illustrated the high intensity laser pulse interaction with the plasma target using 3D PIC simulation.

The 1D model for perfectly reflecting surface played a significant role in understanding the LS regime of ion acceleration. For the laser pulse intensity I_L and duration τ_l the sail velocity, energy per nucleon and efficiency are given by [168]:

$$\beta_{ls} = \frac{(1 + \mathcal{F}) - 1}{(1 + \mathcal{F}) + 1} \tag{2.13}$$

$$\mathcal{E}_{ls} = m_i c^2 \frac{\mathcal{F}^2}{2(\mathcal{F} + 1)} \tag{2.14}$$

$$\eta_{ls} = \frac{2\beta_{ls}}{1 + \beta_{ls}} = 1 - \frac{1}{(\mathcal{F} + 1)^2} \tag{2.15}$$

where $\mathcal{F} = 2I_L\tau_l/\sigma c^2$ is pulse energy per unit surface. Depending upon the constant parameter $\zeta = \pi(n_e/n_c)(d/\lambda)$ the dimensionless target parameter. Here, λ is the laser wavelength and d is a target thickness. It should be noted that for $a_0 < \zeta$ the LS regime prevails [28], however for $a_0 \geq \zeta$ the relativistic transparency starts to dominate. As $v_{ls}/c \to 1$, the reflected light is Doppler shifted $\omega_r = \omega_L/4\gamma^2$, where γ is relativistic factor, ω_L is laser frequency and ω_r is reflected pulse frequency.

The acceleration of ions are more significant and mono-energetic peaks [169] are achieved in case of LS regime since $\mathcal{F}$ is inversely proportional to surface areal density. The theoretical studies and PIC simulations with experimental evidence are reported in Refs. [25, 28, 29, 91, 168–171]. Though, the PIC simulation and energy scaling laws gave promising results but there are challenges to use this for applications such as the repulsion of all the electrons, the acceleration time τ_{acc} of ions should be small to prevent the Rayleigh Taylor [172] and Weibel-like [173] instabilities.

2.2.3 Break-Out Afterburner (BOA)

With the laser intensities comparable to the required that for TNSA mechanism ($\sim 10^{21} W/cm^2$) interacting with the ultra-thin high-density targets ranging from 0.5μm to tens of nm, the Break-out Afterburner acceleration mechanism prevails [20, 109]. There are three stages to the process of acceleration:

- After a brief period of TNSA mechanism as explained in Sec. 2.2.1. The sheath evolves to a quasi-steady-state associated with cold background electrons and hot electrons (by laser). In early TNSA phase, the formation of dense, cold electron component within the target prevents significant penetration of the laser pulse.

- In the enhanced TNSA phase, the plasma being overdense after the TNSA phase has the skin depth comparable to the target thickness. The attenuated laser field in the target heats all of the cold electrons in the target by the laser ponderomotive force. This, in turn, modifies the longitudinal field profile, thereby increasing the conversion efficiency of the laser into the hot electrons. The combined electric field (due to space-charge separation from the sheath and laser ponderomotive force) is experienced by the ions which is considerably larger than the field in the TNSA phase.

- Finally, the Break-out Afterburner stage, where the hot electron plasma expands sufficiently to become underdense to the laser. By the action of ponderomotive force laser pulse penetrates to the rear side of the target, setting up a large longitudinal electric field that co-moves with the ions.

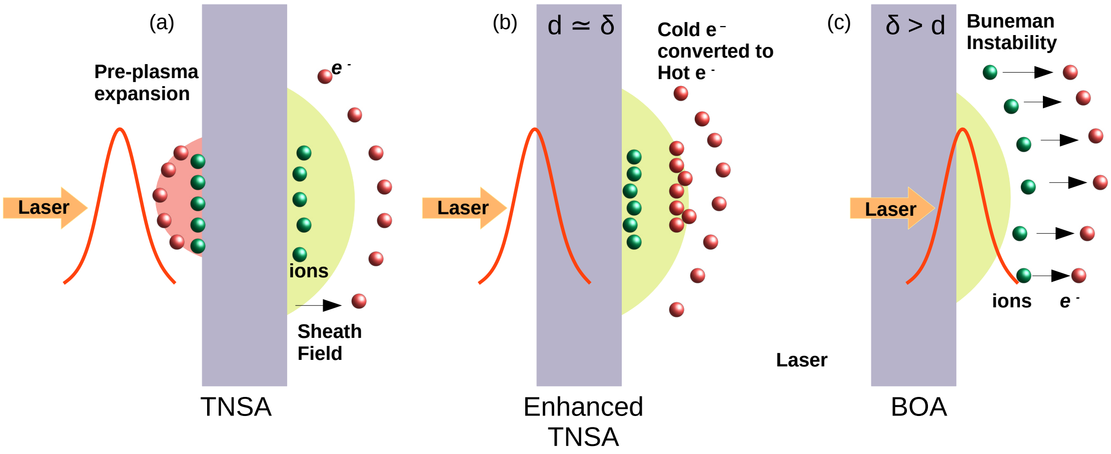

Figure 2.3: *Diagrammatic representation of three stages of Break-out Afterburner mechanism. (a) TNSA, (b) enhanced TNSA and (c) Break-out Afterburner.*

This results in the formation of the unstable relativistic electron beam due to the buneman instability which converts electron energy into the ions. A pictorial representation of the BOA mechanism is depicted in Fig. 2.3

The use of modified target geometry such as double layer target [78, 174], nanoscale targets [21, 175], pre heated diamond target [176] and laser polarization [177] leads to the improved quality of ion bunches. In all the studies done so far the achievable energy is in GeV for BOA mechanism. An interesting experimental study using plastic target of 200nm and 1200nm was done which results in simultaneously two separate acceleration mechanisms (TNSA and BOA) when laser pulse incident at an incidence angle of 10^0 [178].

2.2.4 Relativistic Self-Induced Transparency (RSIT)

The theory of RSIT was proposed in the notable work by Kaw et al. [79] and Max et al. [80]. When an intense laser pulse propagates through an overdense plasma, it accelerates electrons from rest to the relativistic velocities, thus effectively increasing the electron mass m_e with a relativistic factor γ which in turn reduces the electron plasma frequency by the same factor. Here, $\gamma \equiv \sqrt{1 + a_0^2/2}$ is a relativistic factor and $a_0 = eA_0/(m_e c)$ is normalised laser pulse amplitude. As the electrons leave the target, a strong electrostatic field is created between *immobile* ions and electrons. The dispersion relation for the EM wave propagation in case of induced transparency modifies as follows;

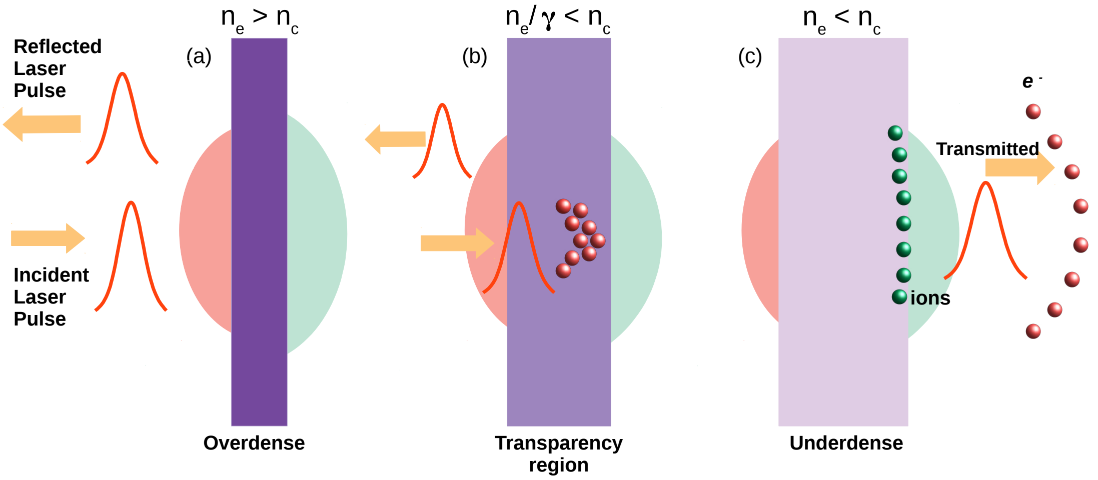

Figure 2.4: *Diagrammatic illustration of processes in RSIT mechanism. (a) When a part of a laser pulse reflects while interaction with overdense plasma target. (b) Now the transparent region, where the relativistic factor γ decreases the target density, for laser pulse to penetrate and (c) making the target underdense for laser pulse to completely propagate through the target.*

$$k^2c^2 = \omega^2 - \omega_p^2/\gamma \tag{2.16}$$

The graphical illustration for RSIT is shown in Fig. 2.4. The dependency on laser intensity to achieve transparency regime was investigated by PIC simulations in Ref. [179]. The density threshold value has a dependency on electron density and ion mass with no effect of ramp density profile. The given dispersion relation [Eq. 2.16] predicts the maximum value of phase velocity but the difference arises due to reflected waves which effectively lowers the plasma frequency.

For the stationary cold plasma model for RSIT mechanism the stationary solutions were obtained by solving the relativistic equation of motion for electrons, continuity equation and Maxwell's equation as studied in Refs. [32, 180–182]. The complete analysis of the same is presented in Appendix A. Due to the action of laser ponderomotive force, all the electrons are pushed into the target, as a result. the electron boundary shifts. The shift of the electron boundary can be calculated by the cold fluid plasma equations for charge separation layer (CSL) $0 \leq x \leq x_d$ (in case of total reflection) and compressed electron layer (CEL)$x \geq x_d$. The boundary condition to hold the transition for plasma density $n_0 \leq 1.5n_c$ and $n_0 > 1.5n_c$, the threshold amplitude of incident laser pulse is found to be [180];

$$a_{th}^2 = 2n_0(n_0 - 1) \quad for \quad n_0 \leq 1.5n_c \tag{2.17}$$

$$a_{th}^2 = n_0(1 + a_B^2)(\sqrt{1 + a_B^2} - 1) - a_B^4/2 \quad for \quad n_0 > 1.5n_c \tag{2.18}$$

where

$$a_B = n_0\left(9/8n_0 - 1 + 3/2\sqrt{9/16n_0^2 - n_0 + 1}\right)$$

is the maximum evanescent field at the threshold.

Tushentov et al. [181] referred the soliton like formation for plasma density $< 1.5n_c$ which then propagates into the plasma and for $> 1.5n_c$ the laser pulse can only penetrate over a finite thickness. A study as reported in Ref. [182] showed that the stationary solution existed for both semi-infinite and finite layer. It was observed that at even part of the region, a stationary solution exists and it might be the region of transparency. Also, there are regions where both opaque and transparecy can occur, which depend on electron density, laser amplitude and target thickness. The threshold plasma density was studied in Ref. [30], even in the presence of electron heating. The proton acceleration from thin foil is reported in Refs. [33, 81, 82, 183–185], and from nanotargets in Ref. [175]. The advantage of using multilayer target geometry is studied by Refs. [85, 186]. The effect of polarization dependence is explored in Refs. [90, 91]. The effect of chirped laser pulses on the RSIT and associated acceleration is presented in Ref. [89].

CHAPTER 3

Ion Acceleration by Relativistic Self-Induced Transparency

In previous Chapters 1 and 2, we have seen the generation of the intense laser pulse, laser-plasma interaction concepts with various particle acceleration mechanisms and applications. In this chapter, we would like to focus on scheme of the relativistic self induced transparency (RSIT) for ion acceleration. The objective of this chapter is to understand the formation of electrostatic fields using the RSIT and to explore the application of the same in accelerating protons from a secondary layer behind the main target.

In Section 3.1 we briefly discuss the RSIT, along with a theoretical and simulation model. Section 3.2 details the differences between LS and RSIT according to the electrostatic field formation from the main layer, also the ion acceleration and optimization of target parameters are discussed, followed by the summary of the chapter in Section 3.3.

3.1 Model for Study

3.1.1 Relativistic cold fluid model

The propagation of electromagnetic (EM) waves in plasmas has been investigated quite extensively in Refs. [49, 187]. The dispersion relation for EM waves propagation in plasmas, derived in chapter 1(2) is expressed as

$$\omega^2 = \omega_p^2 + k^2c^2, \tag{3.1}$$

where ω, and k are respectively the frequency and wave propagation vector of EM waves, c is the speed of light in vacuum and $\omega_p = \sqrt{n_e e^2/\varepsilon_0 m_e}$ is the natural frequency of the plasma oscillations. Here e, m_e and n_e are respectively the electron charge, electron mass, and electron density.

It can be understood from the dispersion relation [Eq. 3.1] that the EM waves can not propagate beyond the point where $\omega_p > \omega$ as the wave vector is imaginary, which in turn would be responsible for the attenuation of EM waves. In terms of plasma density, it translates to the fact that the EM waves cannot propagate in plasma beyond a critical density n_c. However, for densities $n_e < n_c$, the EM wave can propagate without much of attenuation. The interaction of very intense laser fields can change the above mentioned criteria with regard to the critical density. Therefore, the relativistic mass of the electrons needs to be taken into account, which in principle decreases the effective plasma frequency and as a result the threshold density for the complete reflection of the pulse also increases. This effect is known as RSIT. The interaction of ultraintense laser pulses with plasma can be modeled by solving the wave propagation equation in Couloumb gauge, continuity equations, Poisson's equation and relativistic Lorentz force equations. The analytical treatment of RSIT, based on a relativistic *stationary plasma model* (cold fluid theory with steady-state solutions), is discussed in Refs. [32, 180, 181]. In this work, we have attempted to solve the set of dynamical equations in *space and time* which govern the plasma response to intense laser fields. We restrict ourselves to the one-dimensional scenario where the laser is considered to be propagating along the z direction. The detailed derivation describing the plasma response (electron + ion) to intense laser fields is described in Appendix A. With no ionic motion the closed set of equations describing the plasma response reduces to

$$\frac{\partial \varphi}{\partial z} = -E_z \tag{3.2}$$

$$\frac{\partial E_z}{\partial z} = Zn_i - n_e \tag{3.3}$$

$$\frac{\partial E_z}{\partial t} = n_e \frac{p_z^e}{\gamma_e} \tag{3.4}$$

$$\frac{\partial^2 \mathbf{a}}{\partial z^2} - \frac{\partial^2 \mathbf{a}}{\partial t^2} = \frac{n_e}{\gamma_e} \mathbf{a} \tag{3.5}$$

$$\frac{\partial p_z^e}{\partial t} = -E_z - \frac{\partial \gamma_e}{\partial z} \tag{3.6}$$

$$\frac{\partial n_e}{\partial t} + \frac{\partial}{\partial z}\left(n_e \frac{p_z^e}{\gamma_e}\right) = 0 \tag{3.7}$$

$$\gamma_e = \sqrt{1 + \mathbf{a}^2 + (p_z^e)^2} \tag{3.8}$$

where, Z is atomic number of the ionic species, n_e and n_i are electron and ion densities in units of critical density, p_z^e is longitudinal electron momentum, E_z is longitudinal electrostatic field created by charge separation, γ_e is relativistic factor of electron, and **a** is vector potential associated with laser pulse. It should be noted that the motion of the electrons Eq. A.41 is governed by the electrostatic field and the ponderomotive force ($\partial\gamma_e/\partial z$) of the laser pulse, which in turn manifests the lowering of the target density, and hence assisting the laser in propagating deeper into the target (Eq. 3.5). Furthermore, it can also be seen from Eq. 3.5 that the limit $n_e/\gamma_e \rightarrow 0$ yields the EM wave propagation equation for free space. On the other hand, the condition $n_e/\gamma_e < 1$ is essential for wave propagation in the RSIT regime because otherwise the laser would be reflected from the overdense plasma. As can be seen from Eq. 3.8, in principle one needs to solve for p_z^e to know the γ_e, and hence the threshold plasma density where RSIT ceases to exist. From this, one can infer that the electron heating (p_z^e) plays quite a crucial role in RSIT.

In order to investigate the interaction dynamics in RSIT regime, we have solved these equations numerically in space and time with following initial/boundary conditions,

$$\mathbf{a}(0,t) = a_0 exp\left(\frac{-4t^2}{T^2}\right)\left[\delta\cos(t)\mathbf{e_x} + \sqrt{1-\delta^2}\sin(t)\mathbf{e_y}\right] \tag{3.9}$$

where, T is FWHM pulse duration, and δ is a constant which is either 1 for linearly polarized (LP) laser pulse or $\frac{1}{\sqrt{2}}$ for circularly polarized (CP) laser pulses. In this chapter, we have used only CP laser pulses. In order to benchmark the results of this analytical framework, we have simulated the interaction of 5 cycle Gaussian laser pulse (a_0 = 20) with semi-infinite plasma. The laser is allowed to incident normally from vacuum ($z < 12\lambda$) to a semi-infinite plasma slab ($z \geq 12\lambda$) with density $n_i = n_e = 2n_c$.

In Fig. 3.1, we have compared the longitudinal electrostatic field (E_z) as calculated by numerically solving Eq. 3.2 to Eq. 3.8 with 1D PIC simulation, and

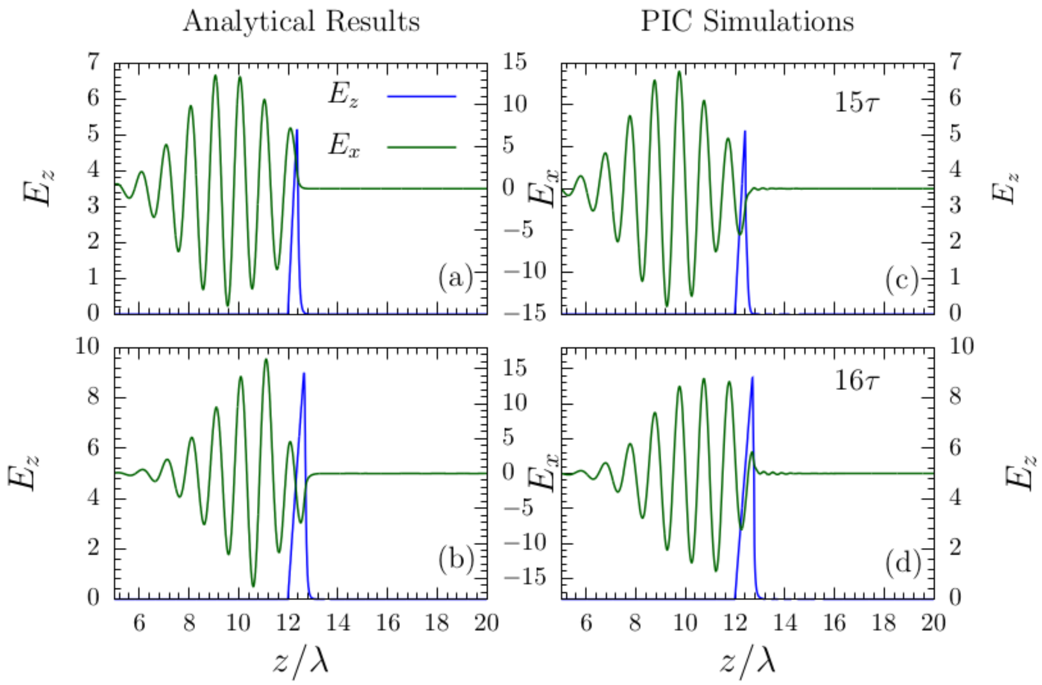

Figure 3.1: *The component of the laser field along x direction (E_x) and electrostatic field (E_z) created by charge separation is presented by numerically solving Eqs. 3.2 - 3.8 (left panel) and compared with 1D PIC simulations (right panel).*

as can be seen from the same that the outcome of theoretical formulation is reasonably in good agreement with PIC simulation. However, in order to study the laser interaction with target of finite thickness, one needs to incorporate the plasma expansion in vacuum [134] with above set of equations.

In order to have some qualitative understanding of the effect of finite target thickness and corresponding threshold density (beyond which the target will not be transparent for a given laser intensity), one can, in principle, seek a steady state solution in the transparency regime. Another case might be the reflection of the incident laser pulse by overdense plasma. We study the interaction of the flat-top laser pulse (a_0) of duration 6 cycles with rise and fall of 1 cycle each, with a target of thickness d and density n_e. The pulse profile is considered to be flat-top, such that the condition for RSIT ($n_e/\gamma_e < 1$) can be met from the instant the laser hits the target. Recently in Ref. [30], the relativistic cold fluid model with stationary solutions has been used for semi-infinite plasma, and an expression for threshold plasma density has been reported.

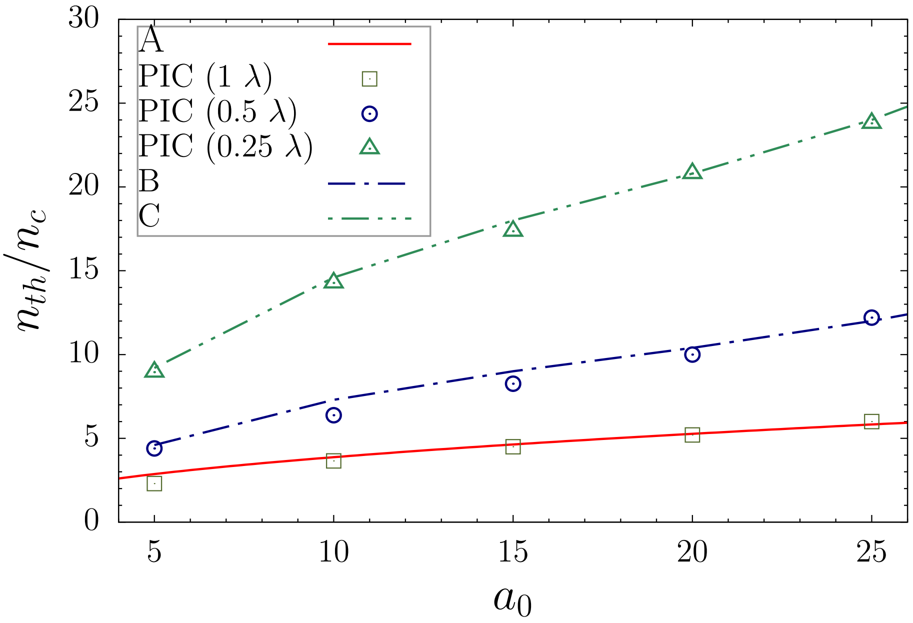

Figure 3.2: *Variation of threshold electron density (n_{th}) with laser amplitude is presented. Curve 'A' shows the expression given by Eq. 3.10. Points denote the results obtained by the 1D fully relativistic PIC simulation for a target thickness of 1λ (square), 0.5λ (circle) and 0.25λ (triangle). Curves 'B' and 'C' respectively show the qualitative estimate of threshold density for $d = 0.5\lambda$ and $d = 0.25\lambda$ using Eq. 3.11.*

The threshold density for RSIT for high laser intensities is given by [30]

$$n_{th} \simeq \frac{2}{9}\left[3 + \sqrt{9\sqrt{6}a_0 - 12}\right] n_c. \tag{3.10}$$

We are mainly interested in having the relativistic transparency in a target with finite thickness. The thickness of the target is such that the laser can pass through the target without much attenuation.

Though the dependence of the target thickness does not explicitly appear in Eq. 3.10, we have tested this expression against a target thickness of 1λ using 1D PIC simulation, and results are presented in Fig. 3.2. It can be seen from Fig. 3.2 that the threshold plasma density for a target of thickness 1λ is in good agreement with Eq. 3.10, which indicates that the laser of amplitude a_0 may be sufficient to sweep out all the electrons from a target of thickness 1λ, with maximum density n_{th} as expressed by Eq. 3.10. A total number of electrons present in a plasma slab (1D scenario) of density n_e and of thickness d should be $n_e d$, so the agreement of Eq. 3.10 and the PIC simulation would dictate

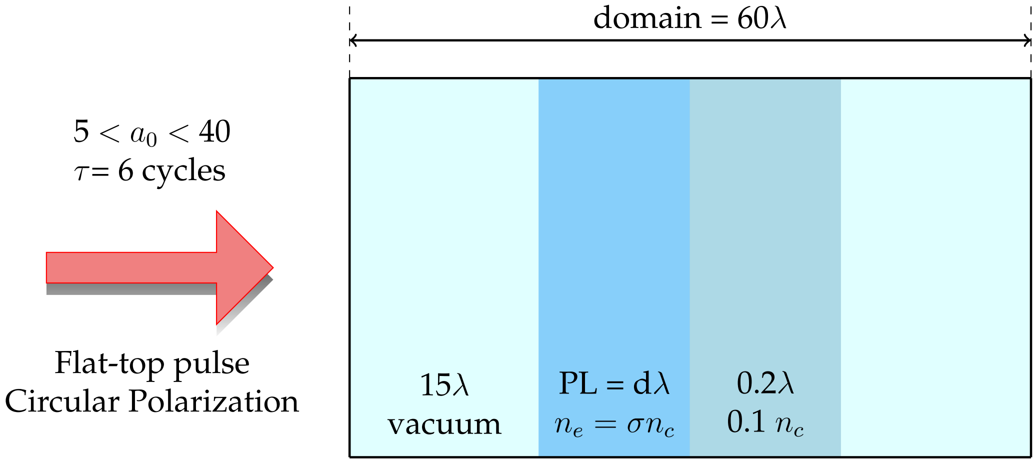

Figure 3.3: *A schematic illustration of simulation domain (60 λ) where double layer target geometry place at 15λ. d and σ corresponds to different primary layer target thickness and density. A Flattop laser pulse is incident on the target with $\tau = 6cycles$ (rise and fall = 1cycle) from left side of domain.*

that laser of amplitude a_0 would be sufficient to sweep out $n_e d$ electrons. We can extend this idea to subwavelength targets, and alternatively write Eq. 3.10 such that for $d = 1\lambda$ the threshold density is given by Eq. 3.10. The corrected expression for threshold density for a target of thickness d should read as,

$$n_{th} \simeq \frac{2\lambda}{9d}\left[3 + \sqrt{9\sqrt{6}a_0 - 12}\right] n_c. \tag{3.11}$$

The results obtained by this simple scaling law given by Eq. 3.11 is also presented in Fig. 3.2, and compared with PIC simulation for the same. It can be seen that the threshold density predicted by Eq. 3.11 is in reasonably good agreement with PIC simulation. It should be noted that, in Fig. 3.2, the region below the data points for particular target thicknesses would be transparent and the region above it would be opaque.

3.1.2 PIC Simulation

We have used the 1D3V fully relativistic PIC code LPIC++ [188] to carry out the studies. The dimensionless electric fields are normalized as $a_0 = eE/m_e\omega c$, where ω is the frequency of the laser pulse, and E is the electric field amplitude in SI units. Time and space are normalized by one laser cycle and wavelength, respectively. The PIC code is modified to study the laser interaction with a multilayer target structure. A figurative illustration of the simulation domain is shown in Fig. 3.3. The laser pulse is considered to be a flat-top of duration 6 cycles with rise and fall of 1 cycle each, propagating along the z direction, and incidents normally on the target. For the complete study, we have used a simulation domain of length 60λ (unless otherwise stated) and the Hydrogen plasma is considered to be located in the region $15\lambda \leq z \leq d$, where d is the target thickness. The remaining space of domain is treated as vacuum. The target density will be chosen such that RSIT will enable the laser to pass through. An extra layer of thickness 0.2λ, with a density of $0.1n_c$, is placed behind the main target. The density of the second layer is kept low so that the laser can also pass through this layer as well, and the ions from this layer will then experience the electrostatic field created by RSIT, and will accelerate as a bunch.

3.2 Results and Discussion

3.2.1 Difference between Light Sail (LS) and Induced Transparency (RSIT) Regime

Although both ion acceleration mechanims are for "thin" targets but the difference lies between the conditions that influence the change in parameteric study of laser and plasma target. In light sail regime the target thickness plays a vital role along with a phenomenon of "perfect" plane mirror i.e. total reflection[28]. Thereby, manifesting the conditions as, R$\simeq$1, $a_0 \leq \xi$ and $d < d_{opt}$. Now taking in consideration the RSIT regime these conditions varies as $a_0 \geq \xi$ and R$\simeq$0. The subtle condition $a_0 \simeq \xi$ discusses another mechanism known as phase stable acceleration mechanism, where protons within the skin depth of laser pulse are synchronously accelerated and bunched like in "radio frequency accelerators" [189]. The parameters are defined as follows: R is reflection coefficient, a_0 is normalized laser pulse amplitude, $\xi = \pi(\frac{n_e}{n_c})(\frac{d}{\lambda})$, d is plasma thickness, n_e as target density, n_c critical density and d_{opt} is optimum target thickness obtained at $a_0 \simeq \xi$.

3.2.2 Formation of electrostatic field

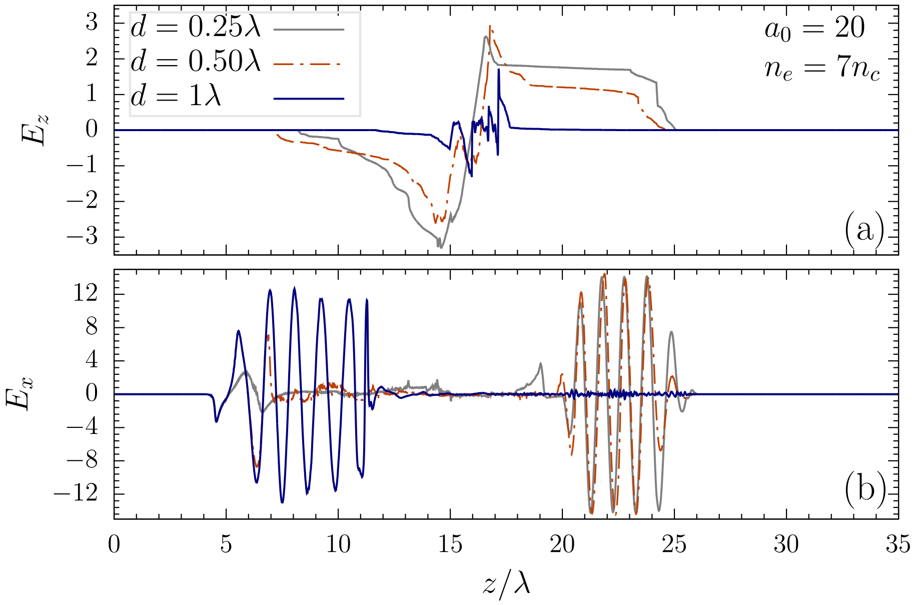

Figure 3.4: *The spatial profile of electrostatic field (E_z) and laser field (E_x) is plotted at 26τ for three different target thicknesses having density 7n_c.*

Above mentioned sections shed light on the theory used to model RSIT mechanism. The balance between the ponderomotive force of the laser and the electrostatic force of the charge separation is the key minimum criterion for the RSIT mechanism. This balance of the forces plays a paramount role, especially in case of finite length plasma. The charge separation electrostatic force have dependency on target thickness and density. For example in Fig. 3.2 we have presented the threshold density for RSIT as obtained by the PIC simulation for three different target thicknesses. It is observed that the thin target supports comparatively larger target density compare to the thicker target as far as RSIT is concerned.

In order to see the effect of target thickness on the formation of the electrostatic field, we have simulated the interaction of the laser with a target of thicknesses 0.25λ, 0.5λ and 1λ. The laser conditions are the same as in Fig. 3.2 (circularly polarized, 6 cycle flat-top with rise and fall of 1 cycle) with $a_0 = 20$ and target density for all three cases considered to be 7n_c. Figure 3.4 shows the spatial profile of the electrostatic field (a) and laser field (b) at 26τ. Here, τ is one laser cycle, and in vacuum laser propagates a distance of 1λ in time 1τ. As can be seen from Fig. 3.4(a), for the case of 0.25λ the electrostatic field is almost flat in the region just behind the target ($15\lambda \leq z \leq d$), while for the target with thickness 1λ, the strength of the electrostatic field is not prominent. This can be explained on the basis of threshold density for different target thicknesses as shown in Fig. 3.2. It can be seen from Fig. 3.2 that, for a target which is 1λ thick, the threshold density for $a_0 = 20$ lies slightly below the density used in this case (Fig. 3.4). However, for 0.25λ and 0.5λ, it is higher than 7n_c. This yields the target with thickness 0.25λ and 0.5λ in the RSIT regime, which in principle is responsible for sweeping all the electrons and creating a strong electrostatic field. The transparency of the target can also be seen from Fig. 3.4(b), where the reflection of a laser pulse for 1λ thickness, and transmission for 0.25λ and 0.5λ thick target, is clearly seen. It should be also noted that the parameter ξ as defined earlier is about 5.5 and 11 respectively for 0.25λ and 0.5λ target thicknesses, and hence the interaction with $a_0 = 20$ brings it in to the RSIT regime. However, 1λ thick target ($\xi \sim 22$) is opaque for the laser with $a_0 = 20$. In Fig. 3.4, we have shown the spatial profile of E_z and E_x only at 26τ. However, in order to see the spatio-temporal evolution of the electrostatic field, the electron density and corresponding electrostatic field for the case with $d = 0.25\lambda$ and $d = 0.5\lambda$ are presented in Fig. 3.5. Because we use the same density ($7n_c$) for thicknesses 0.25λ and 0.5λ, we expected that the electrostatic force would be weaker (compared with ponderomotive force) in the case of 0.25λ as compared to 0.5λ. This is so, because effectively the target with thickness 0.25λ would have less charge particles compared to the case when thickness is 0.5λ. The weaker electrostatic force in the case of 0.25λ manifests a stronger push on the electrons by CP laser pulse as can be seen in Fig. 3.5(b). On the other hand, in the case of 0.5λ, the ponderomotive force of the laser is not strong enough to sweep the electrons to large distances, as can be seen from Fig. 3.5(a). However, in both cases, the electrons are pushed away from the target, lowering the density of the target, and hence enabling the target to be transparent for the laser to pass through. When the laser is passed through the target, the electrons are pulled toward the target because of the electrostatic force created by the charge separation of electrons and ions. As can be seen from Fig. 3.5(a), for $d = 0.5\lambda$, the electrons oscillate at higher frequency

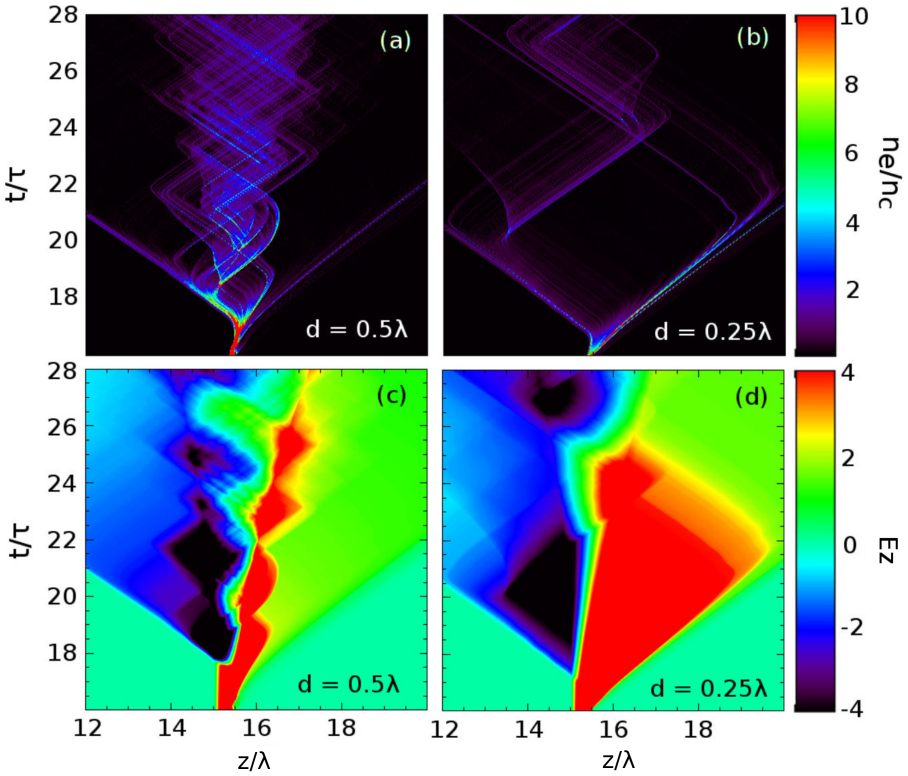

Figure 3.5: *Space-time dependence of electron density for target thickness* 0.5λ *(a) and* 0.25λ *(b) along with longitudinal electrostatic field* (E_z) *for these two cases respectively are presented in (c) and (d).*

compared to the case when $d = 0.25\lambda$, as in Fig. 3.5(b). This can be understood from the lower excursion of the electrons in the 0.5λ case compared to that of the 0.25λ case. It can be summarized as follows, in case of the interaction of a laser with some given density target, the thin (thick) target will manifest weak (strong) electrostatic force and hence large (small) excursions of the electrons by ponderomotive force will take place, which in principle results in low (high) frequency electron oscillations by electrostatic force created by charge separation. The low frequency oscillations of the electron in the case of a thin target manifests the kind of constant electrostatic field which can be harnessed to accelerate ions to very high energies.

3.2.3 Ion acceleration

So far in this chapter, we have discussed the formation of the electrostatic field using the RSIT mechanism. Now we can exploit these fields to accelerate pro-

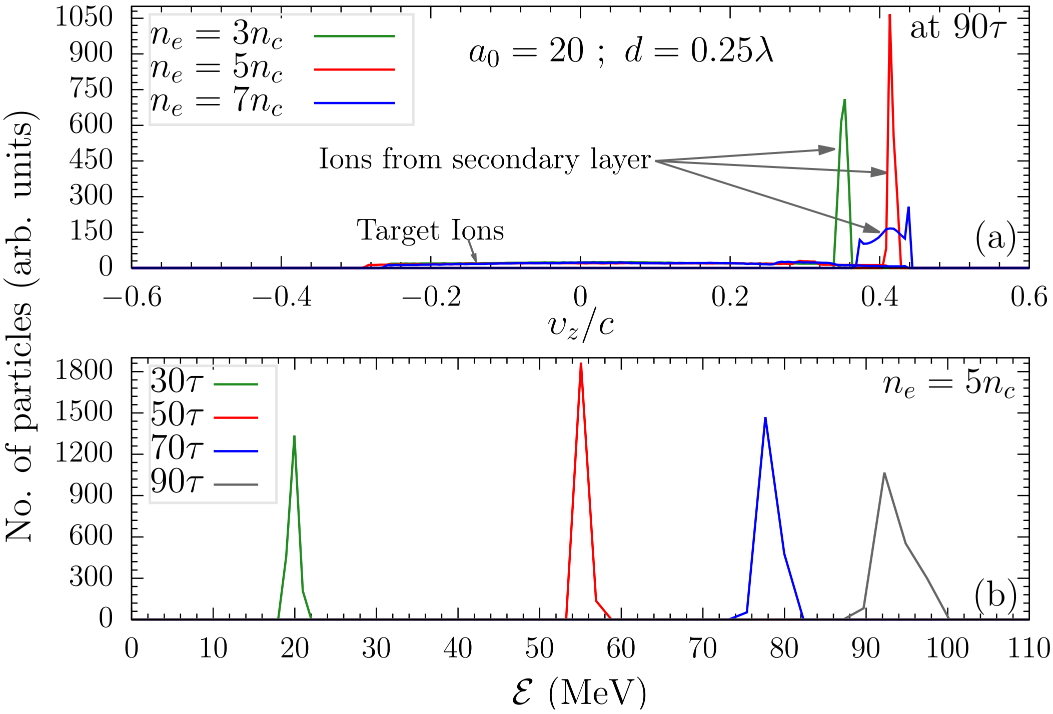

Figure 3.6: *Velocity spectrum (a) of target ions and ions from secondary layer is measured at* 90τ *for the case* $a_0 = 20$, $d = 0.25\lambda$, $n_e = 3n_c$, $5n_c$ *and* $7n_c$. *The energy spectrum (b) for* $n_e = 5n_c$ *at different time steps is also presented.*

tons to very high energies. It is clear that once the electrons are swept out from the target, the ion core undergoes Coulomb explosion, resulting into a cloud expanding predominantly in the laser's propagation direction [87]. The Coulomb explosion of the ion core because of excessive positive charges will not yield a mono-energetic proton beam. In order to achieve the efficient acceleration using the electrostatic field created by RSIT, we have introduced a secondary layer of thickness 0.2λ with density 0.1n_c, just behind the main target (laser incidents on the main target). The density of this extra layer is considered to be low enough such that electrostatic field created by the RSIT mechanism is not affected by the presence of the secondary layer. Secondly, as a consequence of low target density, the laser will not have any direct effect on the energetics of the protons in this layer.

The velocity spectrum of the ions from the main target and the ions from the secondary layer for the case $a_0 = 20$, $d = 0.25\lambda$, and $n_e = 3n_c$, $5n_c$ and $7n_c$, as evaluated at 90τ, are presented in Fig. 3.6(a). As can be seen from this figure, ions from the secondary layer are accelerated as a bunch. On the

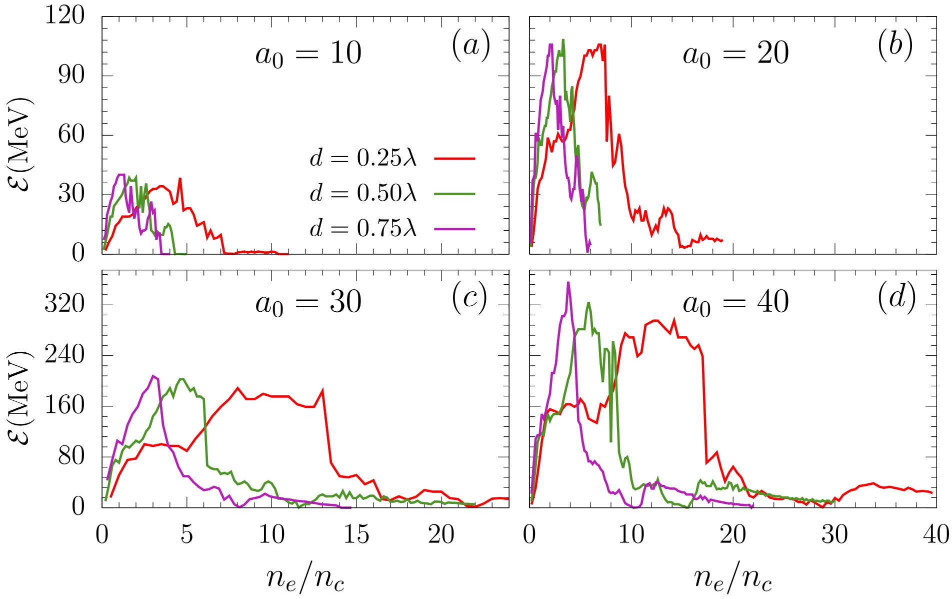

Figure 3.7: *Variation of maximum energy of accelerated ions (from secondary layer) with density and thickness of primary layer for different laser amplitudes.*

other hand, the ions from the main target expands in either direction because of the space charge effect, resulting in large energy spread. This clearly shows the advantage of using an secondary layer behind the target for generating a mono-energetic ion bunch. In this case the target ions are only responsible for creating an electrostatic field which is exploited by an additional thin layer of low density, resulting in a mono-energetic ion bunch. As far as the quality of the bunch is concerned, it can be seen that the spectrum for the case $5n_c$ is much sharper than the one for the cases $3n_c$ and $7n_c$, which in fact signals that there should be an optimum target density for a particular target thickness in order to have very efficient proton acceleration. The details regarding the optimum conditions for given laser and target conditions is discussed in a later part of this section.

The energy spectrum of the accelerated protons from the secondary layer for the case $n_e = 5n_c$, as evaluated at different times, are presented in Fig. 3.6(b). It can be seen that at the early stage of acceleration, the protons gain energy at faster rate, and later the rate of acceleration decreases. This is mainly because of the weakening of the electrostatic force over a period of time. It is observed that the ions from the secondary layer are accelerated to $\sim$ 100 MeV.

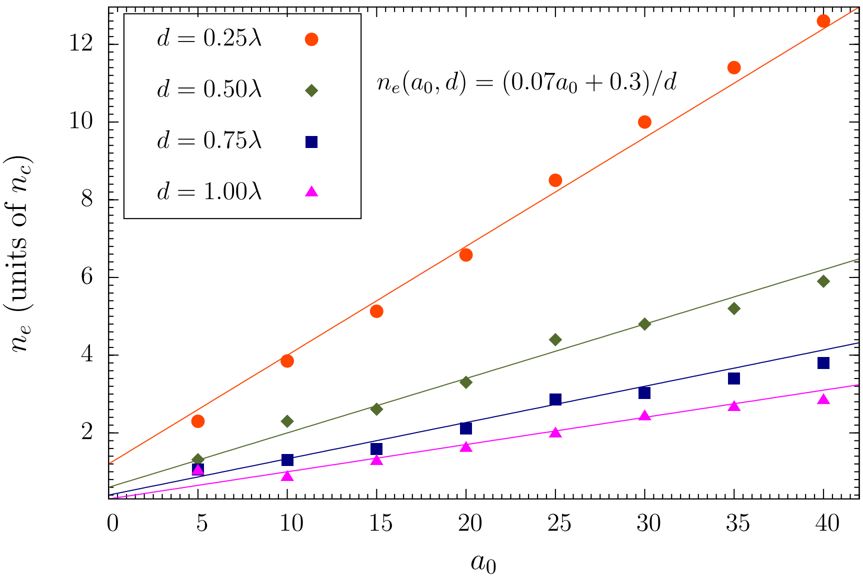

Figure 3.8: *Optimum density of primary target is presented as a function of it's thickness and laser amplitude. The solid line represents the scaling law for optimum density as a function of laser amplitude and target thickness (Eq. 3.12). At these optimum densities ions from the secondary layer attains maximum energy.*

3.2.4 Optimization

As is shown in Fig. 3.6, depending on laser and target conditions, there should be some optimum conditions in order to accelerate the ions most efficiently. In view of this, we have presented the variation of maximum kinetic energy of the secondary ions with the density and thickness of the primary layer for different laser amplitudes in Fig. 3.7. The maximum value of the energy is evaluated at 90τ. It can be observed that there is an optimum density at which the ions can be accelerated most efficiently. This can be explained on the basis that, for low densities overall charge present itself is low enough resulting in weaker electrostatic field by primary target. On the other hand, for higher densities the RSIT mechanism ceases to exist because of reflection of the laser pulse, resulting in a poor longitudinal electrostatic field behind the target. In view of this, it can be understood that there should be some optimum target density for a particular target thickness. The interplay between laser ponderomotive force, and the electrostatic forces by charge separation, results in an ambient condition for the ions from the secondary layer to be accelerated. The optimization of target thickness for RSIT is also being reported in an experimental paper by Henig et. al. [82].

The optimum density corresponding to particular laser and target conditions can be obtained from Fig. 3.7; e.g. for $a_0 = 20$, $d = 0.25\lambda$ the optimum density is about $\sim 6n_c$. In Fig. 3.8 we have presented the optimum density as calculated by PIC simulation. In this figure we have presented the optimum density corresponding to particular thickness and density of primary layer, and laser amplitude. It has been observed that the optimum density for a particular laser amplitude (a_0) and target thickness (d) can be fitted with the following scaling law:

$$n_e(a_0, d) = (0.07a_0 + 0.3)/d. \tag{3.12}$$

It can be seen that Eq. 3.12 fits very well with the predictions of the PIC simulation. The linear relation again points towards the balance between the ponderomotive force ($\propto a_0$) and the electrostatic force ($\propto n_e d$) for maximum energy, which in principle depends on the electrostatic force created by the charge separation in the primary layer. In this study we have kept the thickness and density of the secondary layer as 0.2λ and $0.1n_c$ respectively. In principle one should also have some optimum conditions for the secondary layer, but we reserve that for the future. The multiparametric two-dimensional particle-in-cell study of ion acceleration using a double layered target has been investigated in Ref. [190]. They have observed that the maximum ion energy gain corresponds to a certain optimal electron areal density depends almost linearly on the square root of the the laser intensity. The linear dependence of the target density on a_0 (Eq. 3.12) is in qualitative agreement with the scaling presented in Ref. [190], because the laser intensity I and a_0 is related as $I = 1.3678 \times 10^{18} a_0^2 (\mu m/\lambda)^2$.

3.2.5 Ion energy comparison

We have seen that ions from the secondary layer are accelerated to $\sim$ 100 MeV using 6 cycle flat top, circularly polarized laser with $a_0 = 20$. It would be interesting to know how these energies are comparable to the those obtained using LS or DCE regimes of acceleration. In Ref. [87] the authors have considered the double layer geometry. The primary layer is Al^{13+} plasma with $n_e = 400n_c$ and thickness 0.1λ, however the secondary layer is comprised of Hydrogen plasma with $n_e = 30n_c$ and thickness 0.05λ. This double layer target is irradiated by a 30 fs ($\sim$ 11 cycles) laser with peak intensity of 2.7×10^{22} W/cm^2 ($a_0 \sim 112$ for $\lambda = 0.8\mu$m). These parameters would yield the ratio $a_0/\xi \sim 0.89$, which effectively brings the interaction in the regime where the electrons are pushed by LS but ions from secondary layer are predominantly accelerated by the electrostatic field created by Al^{13+} ions. They have reported that using a super-gaussian laser pulse protons from the secondary layer can be accelerated to ~ 210 MeV. On similar ground, acceleration using a nano-structured double layer targets is reported in Ref. [76]. They also relied on RPA ($a_0 \sim 100$) to remove all electrons from the primary Carbon target, and then accelerate protons from the secondary layer as a bunch to a few hundreds MeV. However, in RSIT enabled acceleration, this energy range is accessible using $a_0 \sim 40$ (see Fig. 3.7) as compare to $a_0 \sim 112$ [87] and $a_0 \sim 100$ [76].

Recently Robinson et. al. [23] have demonstrated ion acceleration in the HB-RPA regime, where they have obtained the proton energies ~ 150 MeV by irradiating a laser with peak amplitude $a_0 \sim 90$. In the HB-RPA regime, the target is opaque to the incident laser, and in this context the acceleration is not very sensitive to the contrast ratio of the laser pulses. Similarly, under the RPA regime, ion acceleration to ~ 150 MeV with $a_0 = 108$ has also been reported in Ref. [191]. However, it can be seen that the RSIT enabled acceleration would yield similar energies with lower laser peak intensities (Fig. 3.7).

Recent development in the field of high power lasers have made it feasible to generate hundreds of MeV of proton beam with low energy spread enabled via RSIT mechanism. A few of the recent experimental studies [33, 84, 90] have demonstrated the use of solid nm targets to generate high energetic proton beams when interacts with ultra intense laser pulses. Furthermore, gas based near critical density targets for RSIT based proton acceleration is recently reported in [184, 192].

3.3 Summary

We have studied the RSIT using a stationary plasma model, and predicted that for subwavelength targets the threshold target density for a particular laser amplitude and target thickness increases. We have also discussed the role of target density and target thickness on accelerating fields, and observed that the protons from the secondary layer behind the target are accelerated most efficiently to a few hundreds MeV by electrostatic fields formed by the RSIT. The role of target ions in this process is to create the electrostatic fields using the RSIT mechanism, which will eventually accelerate the protons from the thin and low density layer placed behind the target. A suitable scaling law connecting the optimum target density for maximum energy, target thickness and laser amplitude is also deduced. Furthermore, it is also observed that the laser intensities required to access the similar energy range in an LS or RPA regime is around 2.5 times the values used here. It should also be noted that the efficient ion acceleration by thin targets is always subject to very high contrast laser pulses.

CHAPTER 4

Chirp Assisted Ion Acceleration Through Relativistic Self-Induced Transparency

In the previous chapter [Chapter 3], the detailed analysis of RSIT was studied using a relativistic cold fluid model along with the PIC simulations. It was observed that the use of the secondary layer was more advantageous to accelerate ions in mono-energetic bunches to MeVs of energy. However, this was not the case for single layered target because the ions from this layer undergoes expansion in either direction due to complete removal of electrons from the target, hence resulting in large energy spread.

In this chapter, we explore the effect of the chirped laser pulse on the transmission and associated ion acceleration by the sub-wavelength target. For negatively (positively) chirped pulses, the high (low) frequency component of the pulse interacts with the target initially followed by the low (high) frequency component. The threshold plasma density for the transmission of the pulse is found to be higher for the negatively chirped laser pulses as compared to that for the unchirped or positively chirped pulses. The enhanced transmission of the negatively chirped pulses for higher densities ($6n_c$) results in very efficient heating of the target electrons, creating a very stable and persistent longitudinal electrostatic field behind the target. The void of the electrons results in expansion of the target ions in either direction, resulting in the broad energy spectrum. We have introduced a very thin, low density ($< n_c$) secondary layer behind the primary layer. The ions from the secondary layer are then found to be accelerated as a mono-energetic bunch under the influence of the electrostatic field created by the primary layer upon interaction by the negatively chirped pulse.

First and foremost in Section 4.1, we discuss the simplified wave propagation model for low laser amplitudes ($a_0 = 0.5$) and its utility to compute the

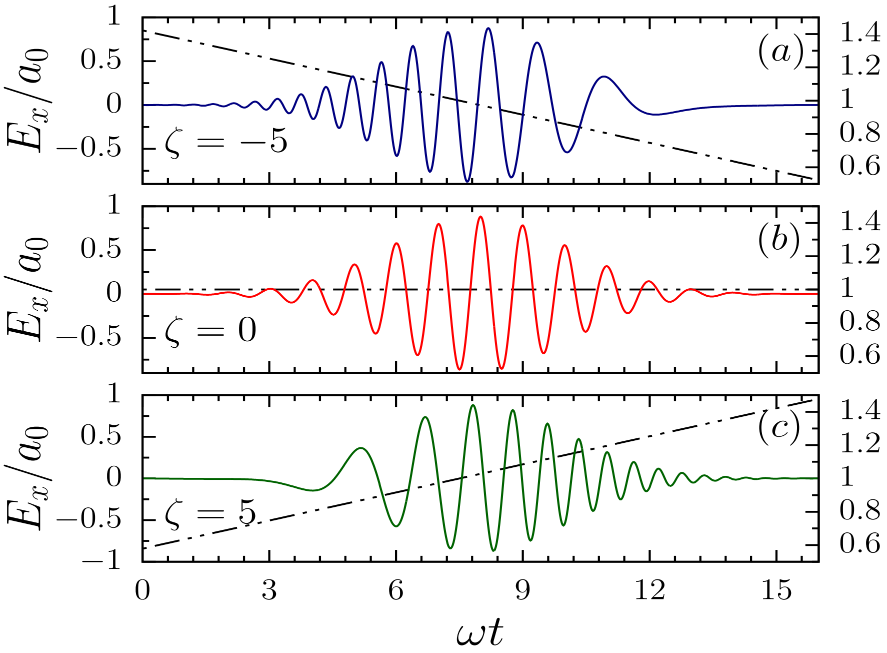

Figure 4.1: *Laser pulse profiles with negative (a), unchirped (b) and positive (c) chirp parameters. Time dependent frequency is also illustrated (dotted line) for each case as well.*

transmission coefficients for different chirp values. The results of the wave propagation model with the 1D PIC simulations are compared. In Section 4.2, we focus on the study of high intense lasers ($a_0 = 20$) with the target. The results showing the effect of the laser pulse chirp on the longitudinal electric field for different target parameters is discussed. Moreover, we consider the need for the second layer to obtain an energetic ion bunch. The optimization study for different target parameters is then carried out in Section 4.3, and finally summary in Section 4.4.

4.1 Theory and Simulation Model

The interaction of the intense laser beams with the overdense plasmas are in general modeled by the cold-relativistic fluid model [30–32, 180, 181]. The use of the cold-relativistic fluid model is justified, as the quiver velocity of the electrons involved in laser-plasma interaction exceeds the electron temperatures, and ions are considered as immobile in the time scales of the interests. The

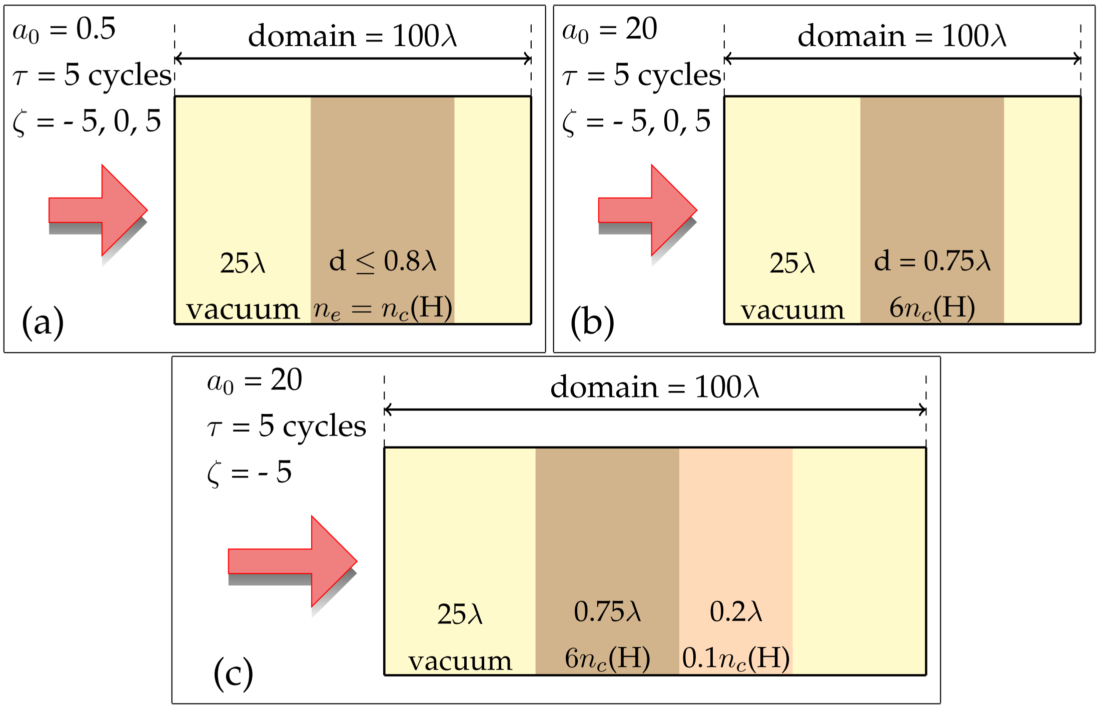
a_0 = 0.5
τ = 5 cycles
ζ = - 5, 0, 5
domain = 100λ
25λ
d $\leq$ 0.8λ
vacuum
$n_e = n_c$(H)
(a)
a_0 = 20
τ = 5 cycles
ζ = - 5, 0, 5
domain = 100λ
25λ
d = 0.75λ
vacuum
6n_c(H)
(b)
a_0 = 20
τ = 5 cycles
ζ = - 5
domain = 100λ
25λ
0.75λ
0.2λ
vacuum
6n_c(H)
0.1n_c(H)
(c)

Figure 4.2: *(a), (b) and (c) represents the diagrammatic representation of simulation domain with different laser and target parameters used throughout the chapter. Here, domain(a) corresponds to Fig. 4.3 - Fig. 4.4, (b) discusses about Fig. 4.6 - Fig. 4.7 and (c) domain is used for Fig. 4.8 - Fig. 4.12. The simulation domain is considered of 100λ and plasma target is placed at a distance of 25λ in both the target geometry. The laser pulse used for interaction is circularly polarized with Gaussian envelope.*

threshold plasma densities for RSIT as obtained by seeking the stationary solutions of the cold relativistic fluid model for a semi-infinite plasma slab is reported in Refs. [30, 31, 180].

The set of relativistic cold fluid equations are in general challenging to solve for very thin targets, and hence kinetic simulations are routinely used for studying the laser interaction with thin overdense plasma layers [182, 186, 193, 194]. In this Chapter, rather than obtaining the stationary solutions for a threshold plasma density, we studied the effect of pulse chirp on the transmission coefficient of the target for a given laser and target parameters. We have used the sub-wavelength target as it allows the transmission from the slightly overdense plasmas as well. The transmission coefficients are calculated by numerically solving the wave propagation equation along with the corrected

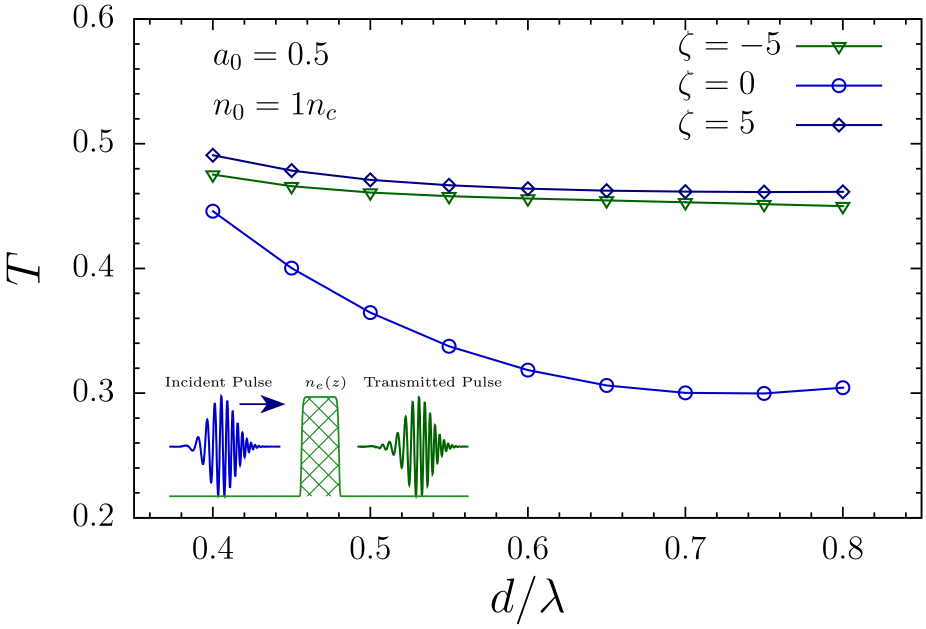

Figure 4.3: *Transmission coefficient of the laser pulse* ($a_0 = 0.5$, $\tau = 5$ *cycles) for chirp parameters* $\zeta = -5, 0, 5$ *for different target thickness of density* $n_0 = 1n_c$ *is compared. The schematic diagram representing the target geometry (Eq. 4.4), incident pulse and transmitted pulse is illustrated as an inlet.*

electron density, taking into account the time-dependent frequency and amplitude of the circularly polarized chirped laser pulse. In the following, we present our simplified wave propagation model to study the effect of the pulse chirping on the transmission coefficient, followed by the comparison with the 1D PIC simulation.

4.1.1 Wave propagation model

Throughout the chapter, we have used the dimensionless units. The laser amplitude is normalized as $\mathbf{a} = e\mathbf{A}/m_e c$, where $\mathbf{A}$ is the vector potential associated with a laser, e and m_e are charge and mass of the electron. The time and space are normalized against the laser frequency (ω) and wave number ($\omega t \rightarrow t$ and $kx \rightarrow x$) respectively. The electron density is normalized against the critical density $n_c = \varepsilon_0 \omega^2 m_e / e^2$. In the dimensionless form the EM wave propagation in plasma can be written as [85],

$$\frac{\partial^2 \mathbf{a}}{\partial z^2} - \frac{\partial^2 \mathbf{a}}{\partial t^2} = \frac{n_e}{\gamma_e}\mathbf{a} \tag{4.1}$$

where, γ_e is the relativistic factor for the electron, and n_e is the electron density. Using the definition of canonical momentum, the γ_e can be expressed as,

$$\gamma_e = \sqrt{1 + \mathbf{a}^2 + (p_z^e)^2} \tag{4.2}$$

here, p_z^e is the dimensionless ($p_z^e/m_e c \rightarrow p_z^e$) longitudinal component of the electron momentum. In general, the electron density will be a function of both z and t. The spatial dependence of the electron density is because of the finite target geometry, however the temporal dependence comes via the chirp of the laser pulse. In a chirped laser pulse the frequency varies with time and hence the associated critical density [$n_c(t) = \varepsilon_0 \Omega(t)^2 m_e/e^2$] for the laser pulse will also vary accordingly. It should be noted that, here we are not solving the full set of dynamical fluid equations, and hence the electron density is not going to evolve with time by continuity equation. In the later part we will see, that this approximation is valid if we intend to calculate the transmission coefficient of the target for the laser pulses with $a_0 < 1$. Furthermore, for $a_0 < 1$ one can ignore the longitudinal electron heating and so Eq. 4.2 reduces to,

$$\gamma_e \sim \sqrt{1 + \mathbf{a}^2}. \tag{4.3}$$

The electron density profile in space and time is then given by,

$$n_e(z,t) \equiv \frac{n_e(z)}{\Omega(t)} = \frac{n_0}{\Omega(t)} \exp\left[- 2^{24} \ln(2) \frac{(z - z_0)^{24}}{d^{24}} \right] \tag{4.4}$$

here, $\Omega(t)$ is a time dependent frequency of the chirped laser pulse (at the peak of the laser pulse $\Omega = 1$), n_0 is the peak target density, d is its thickness and z_0 is the location of the target center. The electron density profile (Eq. 4.4) serves the dual purpose, not only it mimics the thin layer target; rather it is a continuous function of z as well, which is desirable for numerical stability.

The details of simulation domain is presented in Fig. 4.2(a), where we considered to be $L = 100\lambda$ long, and the target (see Eq. 4.4) of thickness d is placed at 25λ ($z_0 = 25\lambda + d/2$). The transmission coefficient (T) is calculated by taking the ratio of transmitted pulse energy to the incident pulse energy. The boundary condition on the left of the simulation domain is precisely the temporal

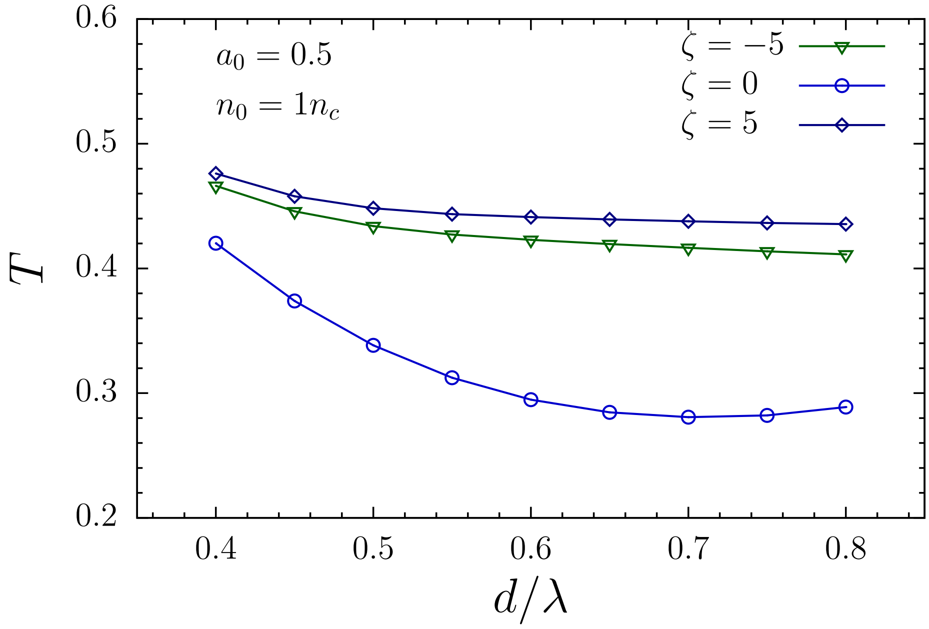

Figure 4.4: *PIC simulation for transmission coefficient of the laser pulse ($a_0 = 0.5$, $\tau = 5$ cycles) for chirp parameters $\zeta = -5, 0, 5$ for different target thickness of density $n_0 = 1n_c$ is compared.*

profile of the laser pulse. In this chapter, we have used the laser pulse model as proposed by Mackenroth et. al. [88], as it models the laser pulse chirp beyond the linear approximation [92, 195–197] and it is also in close analogy to the model of chirped pulse amplification [198]. The boundary conditions on left side of the simulation domain for $\mathbf{a} = a_x\hat{x} + a_y\hat{y}$ read as,

$$a_x(0,t) = \frac{a_0}{\sqrt{2}} \exp\Big[-4\ln(2)\frac{t^2}{\tau^2}\Big] \cos[t + g(t,\zeta)] \tag{4.5}$$

$$a_y(0,t) = \frac{a_0}{\sqrt{2}} \exp\Big[-4\ln(2)\frac{t^2}{\tau^2}\Big] \sin[t + g(t,\zeta)] \tag{4.6}$$

$$g(t,\zeta) = \zeta\Big[4\ln(2)\frac{t^2}{\tau^2} + \frac{\tau^2}{16\ln(2)(1+\zeta^2)}\Big] + \frac{\tan^{-1}(\zeta)}{2} \tag{4.7}$$

here, a_0 is peak laser amplitude in dimensionless units, τ is dimensionless FWHM of the laser pulse, and ζ is the chirp parameter. The laser pulse profiles of unchirped, positively and negatively chirped are illustrated in Fig. 4.1. The time dependent frequency of the laser pulse is then given by [88],

$$\Omega(t) = 1 + \zeta\frac{8\ln(2)}{\tau^2}t \tag{4.8}$$

For, $\zeta > 0$ ($\zeta < 0$) the low (high) frequency part interacts with the target first, followed by the high (low) frequency part. To understand how the chirp affects the transmission coefficient of the laser pulse, we have calculated the transmission coefficient for different chirp values by numerically solving the Eqs. 4.1, 4.3 - 4.8. The transmission coefficient of a positively, negatively and unchirped laser pulse ($a_0 = 0.5$, $\tau = 5$ cycles) for different target thickness with $n_0 = 1n_c$ is compared, and the results are presented in Fig. 4.3. It is observed from Fig. 4.3, that as we increase the target thickness the transmission coefficient for the unchirped pulse drops by $\sim 30\%$ with $\sim 100\%$ increase in the target thickness. However, for chirped pulses, the decrease in the transmission coefficient with target thickness is marginal ($\sim 5\%$) with the same variation in the target thickness. It can be understood by the nature of the chirped pulse itself. If the variation in the target thickness is smaller than the wavelength of the pulse, then, in that case, the transmission coefficient associated with the longer (smaller) wavelength (frequency) would not be affected. On the other hand for shorter (larger) wavelength (frequency) component, the skin depth is anyway much larger than the thickness of the target. The collective effect of the chirping would manifest in more or less similar transmission coefficients as we vary the target thickness in the sub-wavelength domain. In the following, we compare the results of this simplified wave propagation model with 1D PIC simulation.

4.1.2 Comparison with PIC simulations

Next, we turn to a comparison of the simplified wave propagation model (Fig. 4.3) with PIC-simulations where target geometry, laser parameters and simulation domain is considered from Fig. 4.2(a) . The 1D Particle-In-Cell simulation (LPIC++) [188] is carried out to study the effect of target thickness on the transmission coefficient for different chirped values. We have modified this open-source 1D-3V PIC code, to include the multilayer targets, chirped Gaussian laser pulses, and associated diagnostics. In this code the electric fields are normalized as we earlier discussed ($a_0 = eE/m_e\omega c$). However space and time are taken in units of laser wavelength (λ) and one laser cycle $\tau = \lambda/c$ respectively, mass and charge are normalized with electron mass and charge respectively.

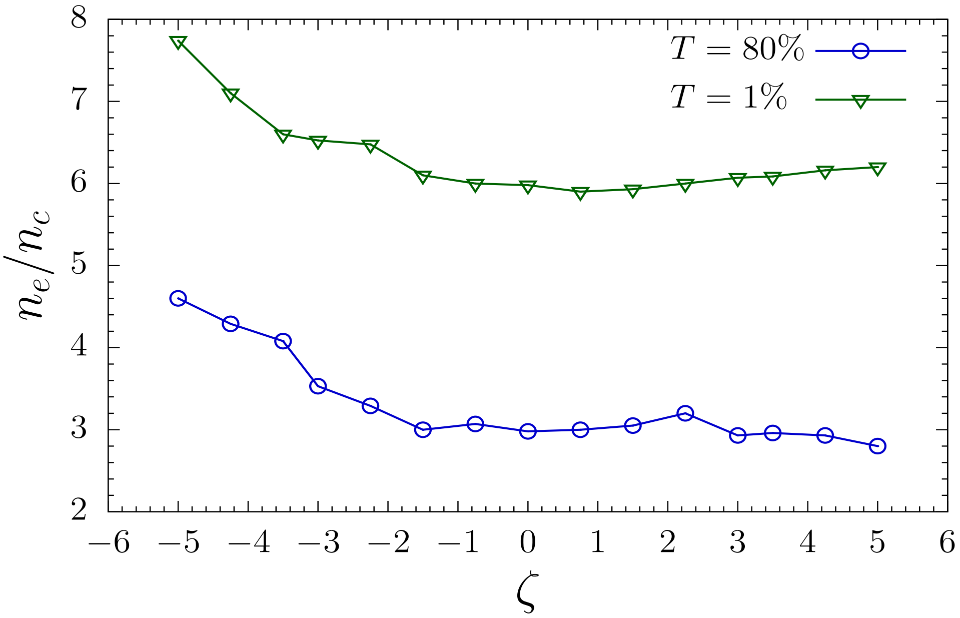

Figure 4.5: *Variation of threshold target density for* 80% *and* 1% *transmission with chirp parameter.*

We have used 100 cells per laser wavelength with each cell having 50 electron and ion macroparticles. The spatial grid size and temporal time step for the simulation are considered to be 0.01λ and 0.01τ respectively.

In Fig. 4.4, we present the transmission coefficient dependence on the target thickness for different chirped values as calculated by the PIC simulations. The agreement with the simplified wave propagation model (Fig. 4.3) is found to be excellent. It is clear that for $a_0 = 0.5$, the electron heating is not very pronounced, or we would have observed the effect of the positive (low frequency interacts first) and negatively (high frequency interacts first) chirped pulses. The approximation we made in wave propagation model regarding the p_z^e, and $\Omega(t)$ are found to be consistent with the PIC simulations as well.

4.2 Results and Discussion

As we have seen, the chirp of the laser pulse can enhance the effective transmission of the laser pulse over unchirped laser pulses. For $a_0 = 0.5$, we did not observe a very prominent difference between the positively and the negatively chirped pulses. This is so, as the interaction dynamics is mostly governed by

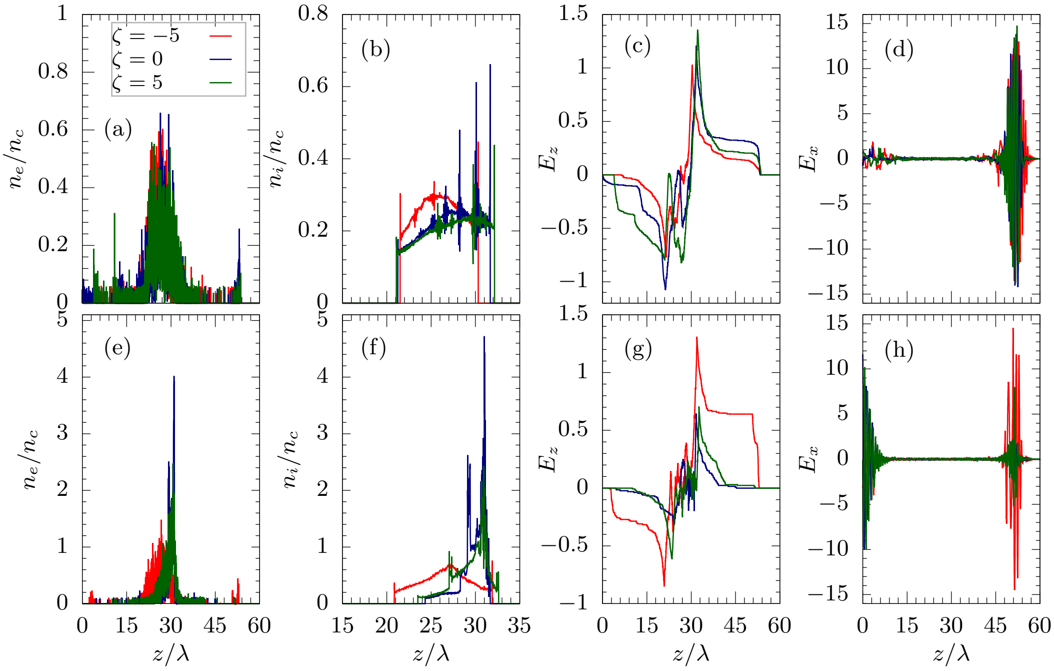

Figure 4.6: *The effect of pulse chirp is illustrated for two different target densities,* $3n_c$ *(upper panel) and* $6n_c$ *(lower panel). The spatial snapshot at* 60τ *for the electron density (a,e), ion density (b,f), longitudinal electric field (c,g) and transverse laser profile (d,h) is presented for* $a_0 = 20$, $\tau = 5$ *cycles and* $d = 0.75\lambda$ *(the target is placed at* 25λ*) .*

the transverse motion of the electrons. The omission of the p_z^e in our simplified wave propagation model seems to be consistent with the fully relativistic 1D PIC simulation. However, for $a_0 \gg 1$, this might not be true, as the process is too non-linear to be approximated by this simple wave propagation model.

The chirp effect on the transmission coefficient and the interaction in general would be much pronounced for $a_0 \gg 1$, as the positively chirped pulse tends to compress the target initially, increasing the target density for the high-frequency part to interact. To study the interaction of the high intense ($a_0 \gg 1$) chirped laser beams with thin targets in RSIT regime, the kinetic simulations are essential, as the fluid model can no longer be used for such scenarios.

Now, we study the interaction of the Gaussian, Circularly polarized laser pulse having peak amplitude $a_0 = 20$, and FWHM duration of 5 cycles with a target of thickness 0.75λ as shown in Fig. 4.2(b). The 1D-3V PIC code LPIC++ is used for this purpose [188]. The simulation domain is considered to be 100λ and the target (protons + electrons) of thickness 0.75λ is placed at 25λ. The laser incidents on the target from the left side. It should be noted that for the cases when $a_0/[\pi(n_e/n_c)(d/\lambda)] < 1$, the ion acceleration is mainly dominated by the Ligh Sail mechanism [28, 29]. On the other hand, the RSIT mechanism begins to prevail in the regime where the ratio $a_0/[\pi(n_e/n_c)(d/\lambda)] \gtrsim 1$. The parameters used in the current study ($a_0 = 20$, $d = 0.75\lambda$ and $n_e \lesssim 8n_c$) clearly indicates that the RSIT regime would prevail. The laser parameters used i.e. $a_0 = 20$, Circularly Polarized are routinely accessible in ELI laser facility [1].

4.2.1 Chirp effect on threshold plasma density

We present the variation of the threshold plasma density with chirp parameter (ζ) in Fig. 4.5. Here, "*threshold plasma density*" is the target density which allows some percentage fraction of the incident pulse to pass through the target for a given chirp parameter. The threshold plasma density for 80% and 1% transmission coefficients are presented for $-5 \leq \zeta \leq 5$ (see, Fig. 4.5). We observe that the threshold plasma density increases for negatively chirped laser pulses in either scenario (80% and 1% transmission). In case of the positively chirped ($\zeta > 0$) pulses, the low-frequency part interacts with the target initially followed by the high-frequency component. The low-frequency component tends to compress the electron layer, increasing the electron density for the high-frequency component to interact. However, in case of negatively chirped pulses ($\zeta < 0$) the high-frequency component interact with the target initially followed by the low-frequency part. For high-frequency EM wave, corresponding critical density is also high, which enable it to transmit through the target without much of attenuation.

In Fig. 4.6, the spatial snapshots (as evaluated at 60τ) of the electron density, ion density, longitudinal field and laser field for different chirp values are shown. The snapshots are also compared for two different target densities, viz $3n_c$ (upper panel) and $6n_c$ (lower panel). We observe that for $3n_c$ case all the quantities are showing the similar characteristics for different chirp values. However, for $6n_c$ case, we can see the distinctive spike of the electron density [see, Fig. 4.6(e)] at $\sim 50\lambda$ for $\zeta = -5$, this manifests in enhanced flat longitudinal electrostatic field [see, Fig. 4.6(g)]. This can be understood from the fact that the transmission coefficient of the target with density $3n_c$ is $\gtrsim 80\%$

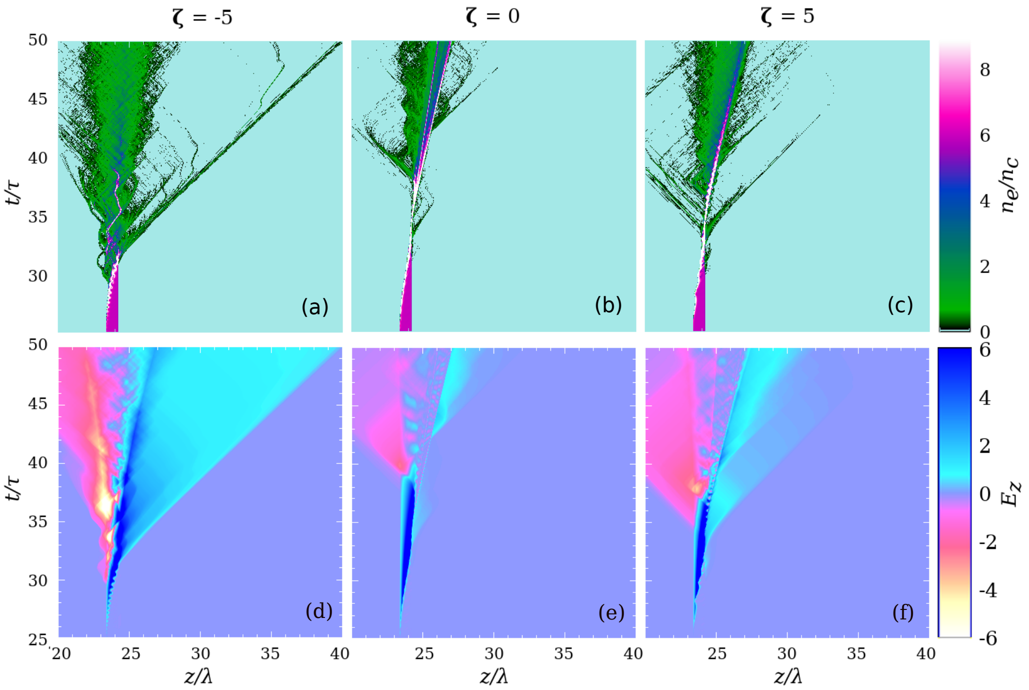

Figure 4.7: *Spatio-temporal profile of the electron density (upper panel) and the longitudinal electrostatic field (lower panel) are presented for chirp parameters* $\zeta = -5$ *(left column),* $\zeta = 0$ *(center column) and* $\zeta = 5$ *(right column). The laser parameters are same as Fig. 4.6 with target density* $n_e = 6n_c$.

for $-5 \leq \zeta \leq 5$ (see, Fig. 4.5). Moreover, for $6n_c$ case only the negatively chirped pulse will be having the $\gtrsim 1\%$ transmission (see, Fig. 4.5), in fact the pulse with $\zeta = -5$ can have $\sim 1\%$ transmission for the target with density $\sim 8n_c$. The transmission of the negatively chirped pulse can be observed in Fig. 4.6(h). Furthermore, for $\zeta = 0$ and $\zeta = 5$, the transmission is $< 1\%$, as a consequence, the associated pondermotive force of the laser pulse tend to push the electrons inside the target, increasing the electron density [see, Fig. 4.6(e)]. The electrostatic field formed by the compressed electron layer tend to pull the target ions, increasing the ion density as well [see, Fig. 4.6(f)]. Now, on the contrary for $\zeta = -5$, the transmission coefficient is $> 1\%$, and hence as the pulse exits the target it drags the electrons with it as well. This motion of the electrons can be observed in the Fig. 4.6(e), as a small spike in electron density around $\sim 50\lambda$ coincides with the location of the pulse after transmission, Fig. 4.6(h). From the above analysis, one can deduce that even 1% transmission of intense laser beams is strong enough to heat the electrons to relativistic energies. As the electrons escape the target for $\zeta = -5$ case, it leaves the tar-

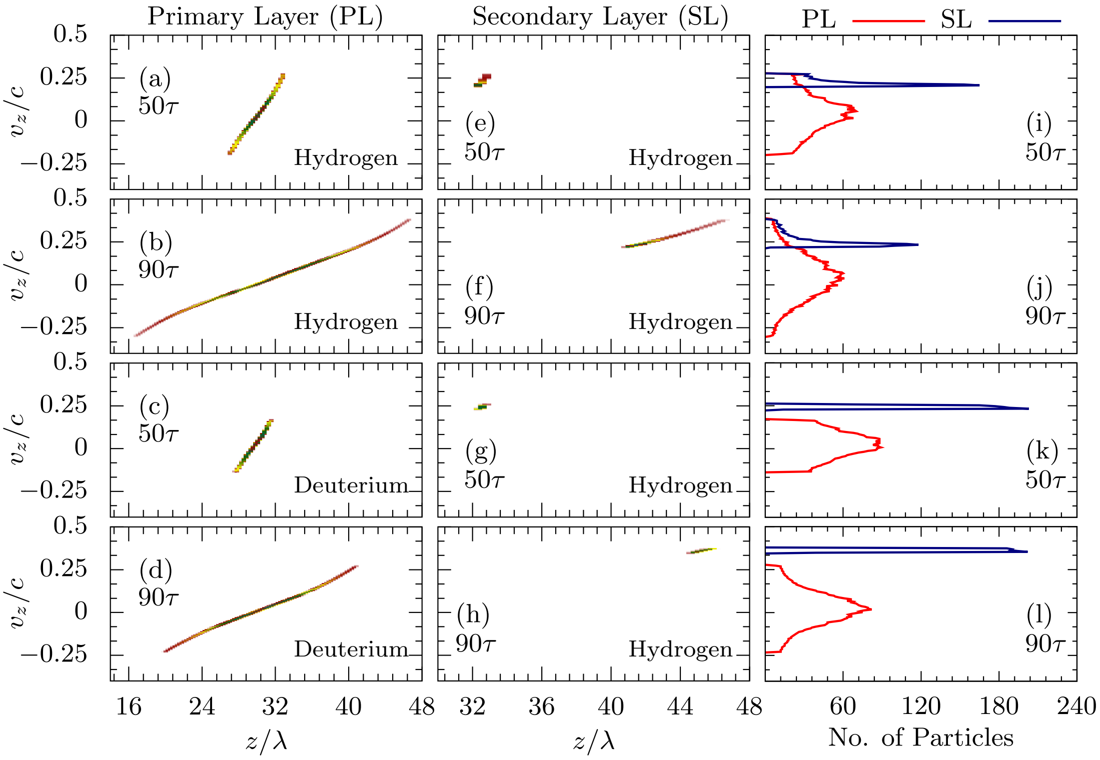

Figure 4.8: *Phasespace plots for the ions from the primary layer* ($d = 0.75\lambda$, $n_e = 6n_c$) *for Hydrogen (a,b) and Deuterium (c,d) at* 50τ *and* 90τ *are presented. The ions from the secondary layer* ($0.2\lambda, 0.1n_c$) *are presented in center column. The secondary layer in both the cases is considered to be of Hydrogen plasma. The velocity spectrum for the ions from primary and secondary layers are illustrated in right column. Here, we have considered a circularly polarized, Gaussian, 5 cycle laser pulse with* $\zeta = -5$ *and* $a_0 = 20$.

get positively charged, resulting in the expansion of the target ions in either direction, as seen in Fig. 4.6(f).

4.2.2 Spatio-temporal evolution of electrostatic field

So far, we have learned that the transmission of the pulse for $\zeta = -5$ results in efficient heating of the electrons followed by a very persistent electrostatic field, a few electrons are dragged away from the target. The rapid heating and excursion of the electrons from the target leaves the target charged, as a consequence the target ions expand under its own coulomb repulsion. To further elucidate this fact, in Fig. 4.7, we present the spatial and temporal evolution of the electron density and longitudinal electrostatic field for $\zeta = -5$, 0 and 5 for the case when target density is $6n_c$, all other laser parameters are same as Fig. 4.6. The compression of the target can be seen for unchirped and positively chirped laser pulses. However, for the negatively chirped pulse ($\zeta = -5$), some electrons are accelerated by the transmitted pulse and starts co-moving with the laser pulse, this is mainly due to the nature of the circularly polarized pulse. For circularly polarized pulse the suppression of $\mathbf{J}\times\mathbf{B}$ heating of the electrons leads the push along the direction of the pulse propagation. This excursion of the electrons is the reason; we can see the approximately constant longitudinal electrostatic field configuration for $z \geq 25\lambda$ in Fig. 4.7(d). We will see in the following how this kind of constant electrostatic field can be harnessed to obtain a mono-energetic proton bunch.

4.2.3 Need for secondary layer

We have seen, that the negatively chirped pulse efficiently create a very stable electrostatic field, as it transmits through the target. However, the excursion of the electrons leaves the target positively charged, as a consequence the target ions expand in either direction because of the Coulomb repulsion of the ions itself. The expansion of the target ions in either direction manifests in very broad energy distribution, on the contrary for any practical applications, a *mono-energetic* ion bunches are desirable. To have a mono-energetic ion bunches from the current setup, a very thin, low density ($< n_c$) secondary layer is introduced just behind the primary layer. The low density of the secondary layer ensures that the interaction dynamics and in general the formation of the electrostatic field by the primary layer remains mostly unaffected even by the presence of the secondary layer. As the laser passes through this composite target (primary + secondary), the electrons are dragged away with the laser pulse, and the ions from the secondary layer experience a very persistent electrostatic field, leading to their acceleration as a mono-energetic ion bunch. The acceleration of the secondary layer can be thought as a slingshot effect, wherein the secondary layer works like a projectile.

Next, we study the interaction of the negatively chirped ($\zeta = -5$), Gaussian, circularly polarized, 5 cycle laser pulse having peak amplitude $a_0 = 20$ with the composite target. The schematic of the simulation domain is repre-

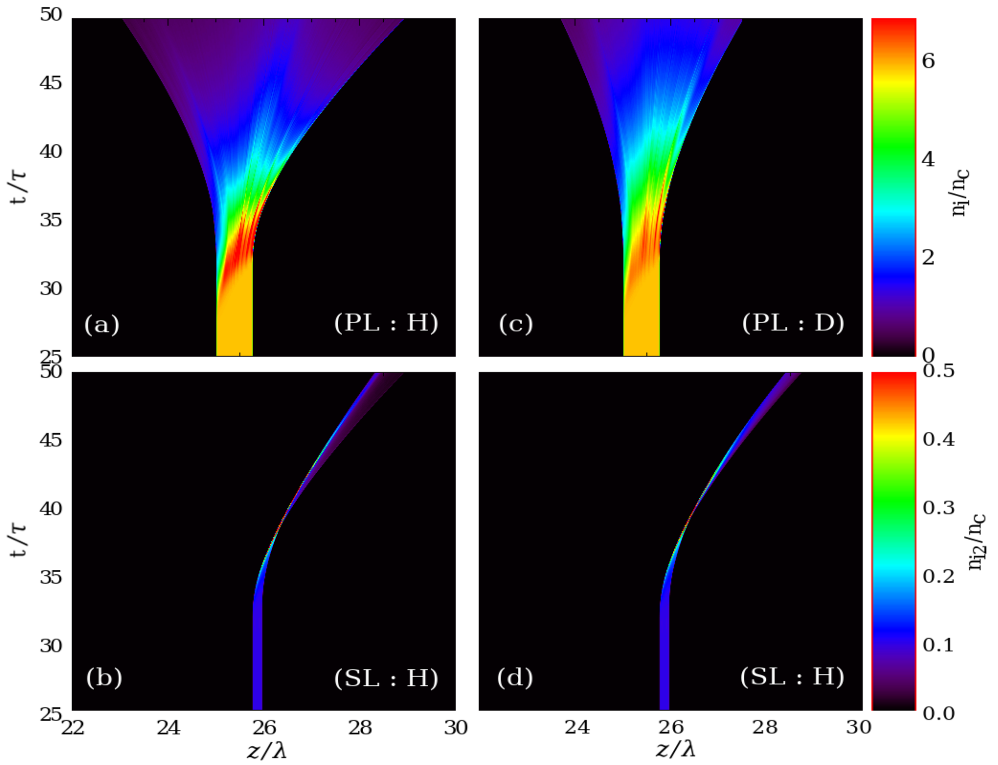

Figure 4.9: *Spatio-temporal evolution of the ion density of PL (upper panel) and SL (lower panel) are presented for* **H+H** *(a,b) and* **D+H** *(c,d) cases. The laser and target conditions are same as in Fig. 4.8.*

sented in Fig. 4.2(c). The thickness (density) of the primary layer (PL) is considered to be $d = 0.75\lambda$ ($n_e = 6n_c$). However, for the secondary layer (SL) the thickness and density are considered to be 0.2λ and $0.1n_c$ respectively. Here, we have examined two cases (a) when the both, primary and secondary layers are made of Hydrogen plasma [refer it as **H+H** case], and (b) when the primary layer is of Deuterium plasma however secondary layer is of Hydrogen plasma, [refer it as **D+H** case]. In Fig. 4.8, the phasespace plots of ions from PL and SL are presented at 50τ and 90τ. The phasespace plots of primary layer for **H+H** case are illustrated in Fig. 4.8(a,b) and for **D+H** case are illustrated in Fig. 4.8(c,d). Furthermore, the phasespace plots of secondary layer are for **H+H** and **D+H** cases are respectively presented in Fig. 4.8(e,f) and (g,h). The velocity spectrum of both PL and SL for **H+H** and **D+H** cases are shown in Fig. 4.8(i,j) and (k,l).

In both the cases, the expansion of the ions from the PL in either direction is visible in Fig. 4.8(a,b,c,d). However, the ions from the SL are found to be

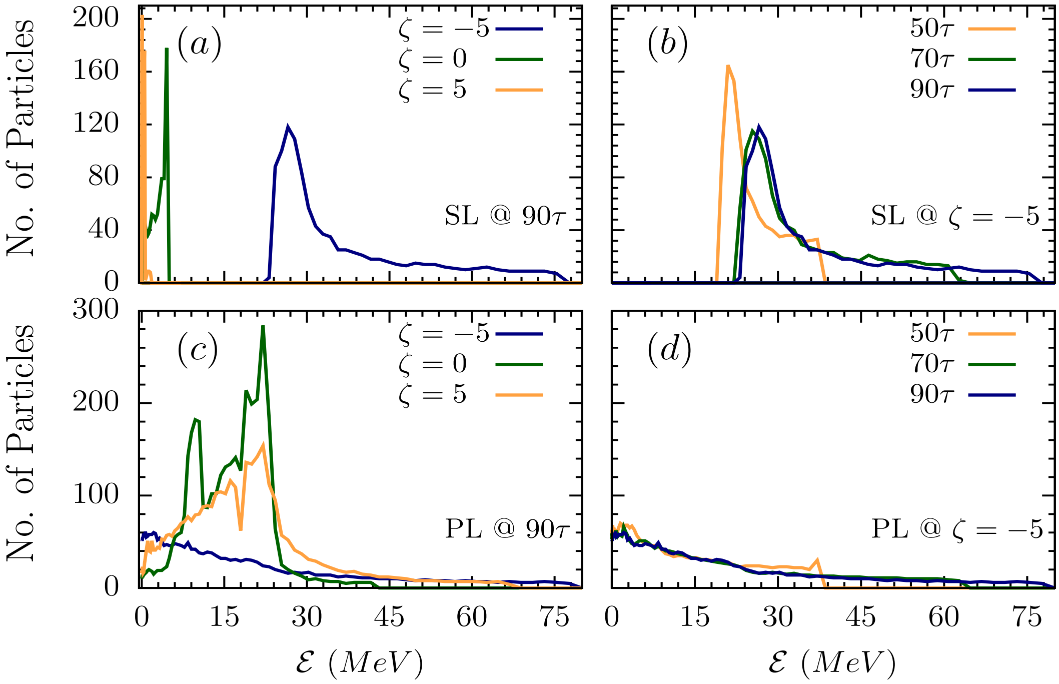

Figure 4.10: *The energy spectrum of primary and secondary ions are evaluated at* 90τ *for different chirp parameters (a) and (c). Moreover, the energy spectrum of the ions from the primary (d) and secondary (b) layer are presented at different time instances for* $\zeta = -5$. *All other laser parameters are same as Fig. 4.8.*

accelerated as a bunch, Fig. 4.8(e,f,g,h). It can be inferred from this figure that in **H+H** case the maximum velocity of the ions from both primary and secondary layer are the same, this is so because the ions at the edge of the primary layer would experience the same longitudinal field as the secondary layer ions would experience. Furthermore, the density of the PL is 60 times to that of the SL, causing more noticeable space-charge effect as compare to that of SL, this results in more rapid expansion of the PL as compared to the SL.

On the other hand, we do observe different velocities of PL and SL in **D+H** case. This is expected as the Deuterium ions are massive as compared to the Hydrogen, this results in slower expansion of the PL, and as a consequence the electrostatic field is persistently maintained for the longer duration, manifesting the mono-energetic acceleration of the ions (i.e., Hydrogen) from the SL. The energy spread of the accelerated ions from the SL in case of **D+H** case is smaller as compared to the **H+H** case. This is mainly because of the persistent electrostatic field created by the Deuterium plasma by virtue of the slower expansion. The spatiotemporal evolution of the ions from PL and SL are compared for the **H+H** and **D+H** cases in Fig. 4.9. The slower expansion of the Deuterium ions (PL) can also be observed by comparing the Fig. 4.9(a) and (c).

The objective of this section is actually to present the scenario wherein the ions from the SL can be accelerated to *almost* mono-energetic energies by the stable electrostatic field created (for negatively chirped pulses) behind the PL. We have discussed the possibility to obtain a high energy proton bunches with lower energy spread in **D+H** case, though the electron density in **D+H** case is same as **H+H** case, the higher mass density in **D+H** case causes the slower expansion of the ions from PL. Here, we do not wish to explore the effect of the pulse chirp on the target comprising of different ionic species other than Hydrogen. Moreover, before this section (Section III-C), we studied the interaction dynamics with the different laser, and target conditions for the Hydrogen plasma only. Given this, in the following we would restrict ourselves with **H+H** case just.

The energy spectrum of the ions from the PL and SL (**H+H** case) are presented in Fig. 4.10 at 50τ, 70τ and 90τ for different chirp values. We observe that for the negatively chirped pulse with given laser and target parameters, the maximum number of ions from the SL are accelerated to ~ 30 MeV, however, the maximum energy ($\mathcal{E}_{max}$) of the bunch is observed to be ~ 75 MeV, as evaluated at 90τ. For the sake of completeness, the effect of the pulse chirp on the energy spectrum of the SL is also illustrated in Fig. 4.10(a). For the positively and unchirped laser pulses the target density $6n_c$ will be in the opaque regime, as a consequence the laser is reflected from the PL. The heating of the electrons at the rear side of the PL is not very efficient, and hence the ions from the SL are not very efficiently accelerated for the positively and unchirped laser pulses. Furthermore, the energy spectrum of the PL is also illustrated in Fig. 4.10(c). It can be seen from this figure that the ions from the PL are accelerated to ~ 20 MeV for $\zeta = 0$ and $\zeta = 5$, this is because of the fact that the target is opaque for positively and unchirped pulses, and hence the acceleration of the ions in here is mainly by the RPA mechanism [22, 91]. On the contrary, the PL would be transparent for the negatively chirped pulse, as a consequence, the acceleration of the ions from the PL is not prominent [see, Fig. 4.10(d)]. Furthermore, the space-charge effect associated with the high density ($\sim 6n_c$) of

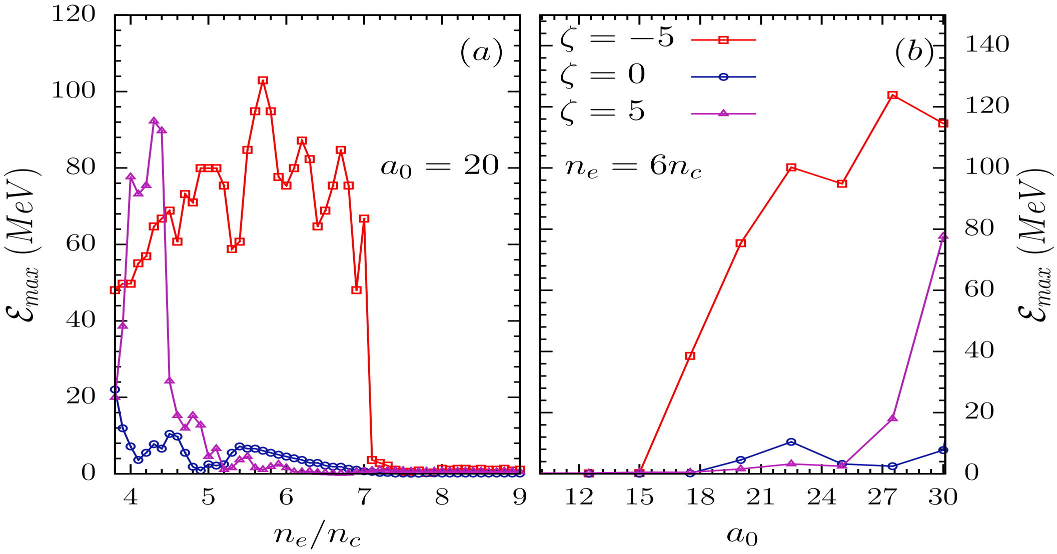

Figure 4.11: *The effect of the pulse chirping on the maximum energy of the ions from the secondary layer is presented for different primary target density (a). The thickness of the primary layer is* 0.75λ *and peak laser amplitude is* $a_0 = 20$. *The variation of the maximum ion energy with* a_0 *is presented in (b), here we have fixed the density of the primary layer to* $6n_c$.

the PL manifests in higher energy spread of the ions.

4.3 Optimization

In the previous section, we have witnessed the *quasi* mono-energetic acceleration of the ions from the SL with lower energy spread. Given this here we study the effect of the density and thickness of the PL on the final energies of the ions from the SL.

In Fig. 4.11 , the variation of the maximum energy of the ions from the SL is presented for different chirp parameters. The effect of the pulse chirp is illustrated for fixed laser amplitude $a_0 = 20$ and different primary target densities (a), and for fixed primary target density and different laser amplitudes (b). As the target density for $a_0 = 20$ is varied, we observe that for $\zeta = -5$, the maximum energy of ~ 105 MeV is obtained for $\sim 6n_c$. The threshold plasma density for $a_0 = 20$ and $\zeta = -5$ is $\sim 7n_c$ [see, Fig. 4.5] and hence the transmission of the pulse for $6n_c$ is $> 1\%$, leading towards the stable electrostatic formation as we discussed in the previous sections. However, for $\zeta = 5$ case, the target with

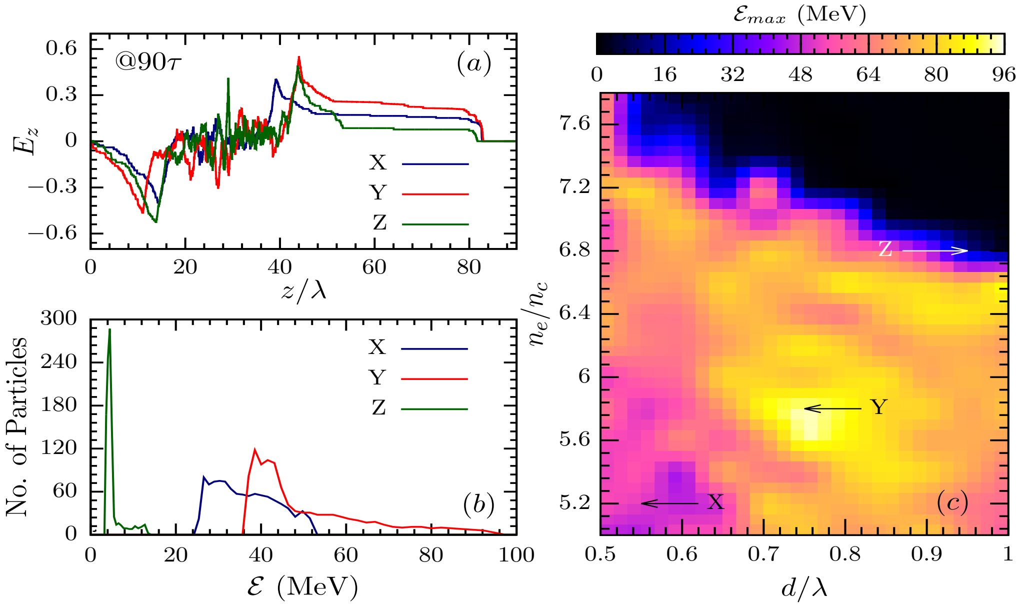

Figure 4.12: *The longitudinal electrostatic field (a) and energy spectrum of the ions from secondary layer (b) are presented for three different primary target conditions. However, the maximum ion energy of the secondary layer is also presented for different thicknesses and densities of the primary layer (c). The laser pulse with peak amplitude* $a_0 = 20$*, duration 5 cycles and chirp parameter* $\zeta = -5$ *is considered. The target conditions* $(d/\lambda, n_e/n_c)$ *are X (0.55,5.2), Y (0.75,5.8), and Z (0.95,6.8). All the quantities are evaluated at* 90τ*.*

density $6n_c$ would be opaque, and hence ions from SL will not be efficiently accelerated. We further observe that for $\zeta = 5$ the maximum ion energy is seen to be for the case when target density is $\sim 4n_c$. As we discussed earlier, the leading low-frequency component of the positively chirped pulse tends to compress the target density by the radiation pressure, as a consequence the following high-frequency component interacts with the high-density target, resembling a similar scenario as negatively chirped pulse interacting with the high-density target. We have also studied the effect of the laser intensity on the maximum ion energy from the secondary layer for fixed target density of $6n_c$. It can be seen from Fig. 4.11(b) that for $a_0 \lesssim 15$, the target with density $6n_c$ and thickness 0.75λ would be opaque, and hence the electrostatic field generation is suppressed and so the acceleration of the ions from the secondary layer. However, as the a_0 increases an efficient acceleration is observed for the negatively chirped pulse.

So far we have seen that the negatively chirped pulses are efficient in generating very persistent and stable electrostatic field behind the target. The effect of the thickness and density of the PL on the maximum ion energy by the negatively chirped pulse is presented in Fig. 4.12. We have varied the thickness of the PL from $0.5\lambda - 1\lambda$, and density from $5n_c - 8n_c$, and maximum ion energy (as evaluated at 90τ) of the ions from SL $(0.2\lambda, 0.1n_c)$ are calculated for $a_0 = 20$, $\zeta = -5$, 5 cycles, circularly polarized, Gaussian laser pulse. In Fig. 4.12, we have also presented the electrostatic field and energy spectrum of the ions from the secondary layer as evaluated at 90τ for three different target parameters $(d/\lambda, n_e/n_c)$ namely X (0.55,5.2), Y (0.75,5.8), and Z (0.95,6.8). In all of the three cases we observe very stable flat electrostatic field behind the primary layer [see, Fig. 4.12(a)]. The optimum target parameters for given laser conditions are found to be Y (0.75,5.8) where maximum ion energy is observed to be ~ 100 MeV. We have fixed the parameters of the SL throughout the simulations. The main purpose of the SL is to have an accelerated proton bunch. The parameters of the SL neither alter the electrostatic field formed by the primary layer nor affects the laser pulse propagation, and hence the ions of SL mere serve as test particles.

4.4 Summary

In this chapter, we have studied the effect of the laser chirping on the acceleration of the protons via RSIT. The effect of the pulse chirp on the transmission of the laser pulse through the sub-wavelength target and associated ion acceleration. The transmission coefficient for $a_0 = 0.5$ is estimated by a simplified wave propagation model which takes into account the time dependent critical density of the target. The results of this simplified wave propagation model are found to be consistent with the 1D fully relativistic PIC model. In this work, we have used the chirp model which is beyond the linear approximation. The chirp model used in this study is in close analogy of the idea of the Chirped Pulse Amplification. Furthermore, we studied the interaction of the intense laser pulse with $a_0 = 20$ with the target having the thickness 0.75λ and density $6n_c$ for different chirp parameters. It has been observed that the negatively chirped laser pulse is very efficient in creating a stable and persistent electrostatic field behind the target. The electrostatic field created behind the target can be harnessed by a low density, thin secondary layer behind the target. The optimization of the target parameters is finally carried out to have a maximum energy of the accelerated ions of the secondary layer.

Under optimum conditions the maximum energy of the ions from the secondary layer is found to be ~ 100 MeV for circularly polarized, Gaussian, 5 cycles FWHM, negatively chirped ($\zeta = -5$), laser with peak amplitude $a_0 = 20$. These parameters for 800 nm laser would translates to ~ 10 fs (intensity FWHM) pulse with peak intensity $\sim 8.5 \times 10^{20}$ W/cm^2. However, similar energies are reported in the past, but with much higher a_0 values. For example, in Ref. [27] the authors have demonstrated the ion acceleration in the HB-RPA regime and reported the proton energies ~ 150 MeV by irradiating a laser with peak amplitude $a_0 \sim 90$. Similarly, under the RPA regime, ion acceleration to $\sim$ 150 MeV with $a_0 = 108$ has also been reported in Ref. [191].

CHAPTER 5

Laser Pulse Dispersion in Underdense Plasma and Associated Ion Acceleration

In previous chapters 3 and 4 we have seen the use of composite two-layer target geometry and effect of pulse chirping on the ion acceleration using RSIT. To further elaborate the study in this chapter our focus is to study the evolution of the laser pulse as it propagates in the underdense plasmas.

There are two regimes of laser propagation in plasma, one with $a_0 < 1$ and other with $a_0 \gtrsim 10$. For the moderate laser intensities ($a_0 < 1$) we invoke the 1D relativistic cold fluid model, avoiding some of the common approximations relevant for underdense plasmas. The results for this case are then compared with the 1D PIC simulations and agreement is found to be excellent. The evolution of the ultraintense ($a_0 > 1$) laser pulses is studied by PIC simulations only. The effect of the plasma density, and other laser parameters is also explored. Furthermore, the dispersed ultraintense laser pulse is then used to study the acceleration of the ions via RSIT.

The chapter is organized as follows, in Section 5.1 we have discussed about the governing equations for 1D wave propagation along with the details of the PIC simulations. Next in Section 5.2 the pulse dispersion for $a_0 < 1$ followed by the dispersion of the ultraintense pulses ($a_0 \geq 10$) is studied. The ion acceleration by the RSIT mechanism via the dispersed pulses is also discussed in the Section 5.3, followed by the conclusion in Section 5.4.

5.1 Theory and Simulation Model

The objective of this chapter is to study the dispersion of the electromagnetic (EM) waves as it propagates in an underdense plasma and the use these dispersed pulses to enhance the ion acceleration through RSIT. The propagation

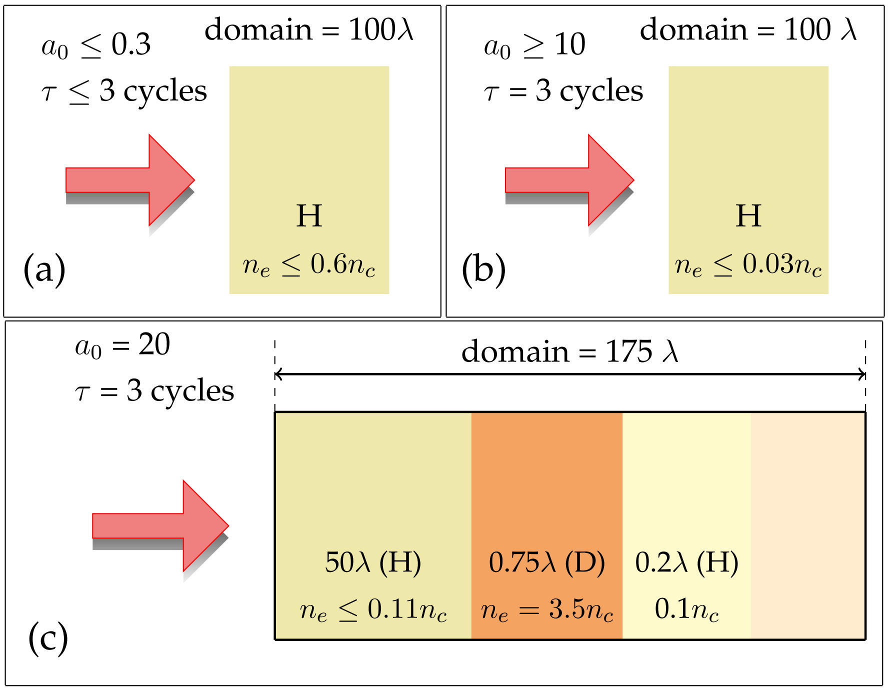
$a_0 \leq 0.3$
$\tau \leq 3$ cycles
domain = 100λ
H
$n_e \leq 0.6n_c$
(a)
$a_0 \geq 10$
τ = 3 cycles
domain = 100 λ
H
$n_e \leq 0.03n_c$
(b)
a_0 = 20
τ = 3 cycles
domain = 175 λ
50λ (H)
$n_e \leq 0.11n_c$
0.75λ (D)
$n_e = 3.5n_c$
0.2λ (H)
$0.1n_c$
(c)

Figure 5.1: *(a), (b) and (c) corresponds to various simulation domain taken into account for different laser and target parameters. Here, domain (a) is taken into consideration for Fig.* 5.2 *- Fig.* 5.6*. Similarly, domain (b) corresponds to Fig.* 5.7 *- Fig.* 5.9 *and domain (c) discusses Fig.* 5.10 *- Fig.* 5.12 *For all the cases linearly polarized, Gaussian laser pulse is taken into account.*

and the dispersion of the EM waves can be understood by the relativistic cold fluid model. Recently a model was developed in Refs. [105, 199] to study the transition from the wakefield generation to the soliton formation. However, for the sake of completeness in this work we elaborated the cold fluid model with immobile ions, as approximation.

The normalized laser parameters are as follows, $\mathbf{a} = e\mathbf{A}_\perp/m_e c$ as normalized laser pulse amplitude, scalar potential as $\varphi = e\phi/m_e c^2$, time and space with laser frequency and wave vector ($\omega t \to t$ and $kx \to x$) respectively, velocity as $\beta = v/c$, momentum is normalized $\mathbf{p} = \mathbf{P}/m_e c$, charge and mass are normalized by electron charge and mass, the electron density is normalized by critical density $n_c = \varepsilon_0 \omega^2 m_e/e^2$. By using these normalization the following set of equations are deduced;

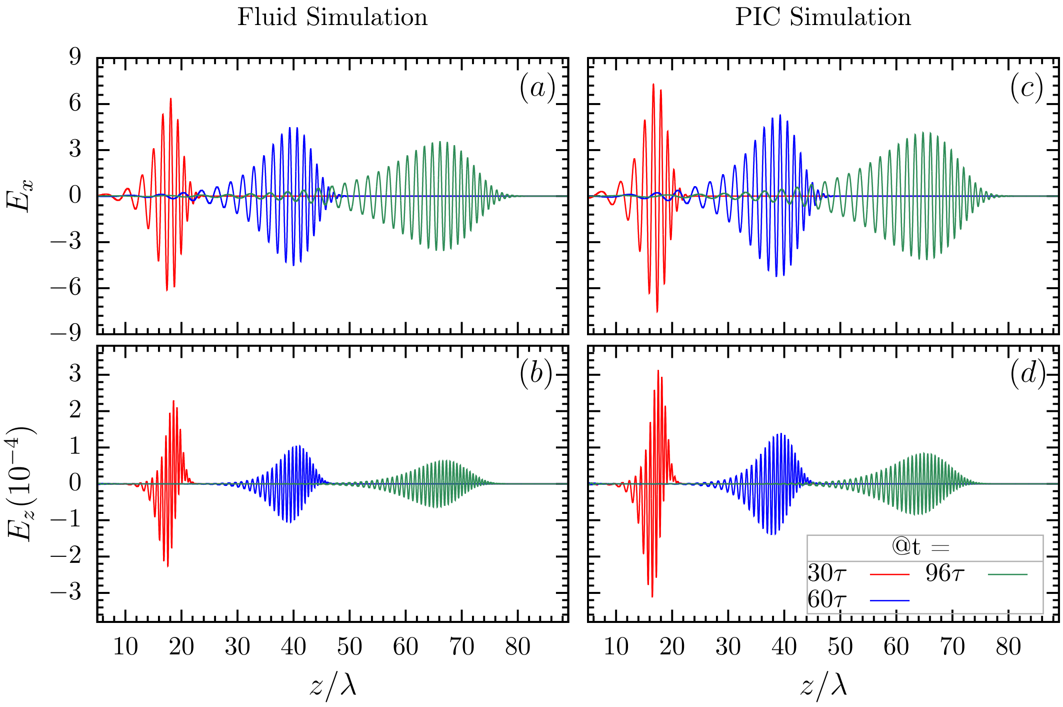

Figure 5.2: *The spatial profile of the electromagnetic (transverse) fields (a,c) and electrostatic (longitudinal) fields (b,d) is presented at different time instances using fluid simulation (left panel) and PIC simulation (right panel). Here, we modeled the interaction of the 800 nm, 3 cycles (FWHM) Gaussian laser pulse* ($a_0 = 0.1$) *with plasma having density* $0.5n_c$.

$$\frac{\partial^2 \mathbf{a}}{\partial z^2} - \frac{\partial^2 \mathbf{a}}{\partial t^2} = n_e \frac{\mathbf{a}}{\gamma} \tag{5.1}$$

$$\frac{d\beta}{dt} = \frac{(1-\beta^2)}{\gamma}\frac{\partial \varphi}{\partial z} - \frac{1}{2\gamma^2}\left(\frac{\partial \mathbf{a}^2}{\partial z} + \beta \frac{\partial \mathbf{a}^2}{\partial t}\right) \tag{5.2}$$

$$\frac{\partial n_e}{\partial t} + \frac{\partial}{\partial z}\Big(n_e \beta\Big) = 0 \tag{5.3}$$

$$\gamma = \sqrt{\frac{1+a^2}{1-\beta^2}} \tag{5.4}$$

$$\frac{\partial^2 \varphi}{\partial t \partial z} = -n_e \beta \tag{5.5}$$

The above set of equations are the basis of our analysis of the dispersion of the EM wave in the underdense plasma. In order to validate the results of our fluid model, we used a 1D particle-in-cell (PIC) simulation, the details of the PIC simulations are as follows: The 1D Particle-In-Cell simulation (LPIC++)

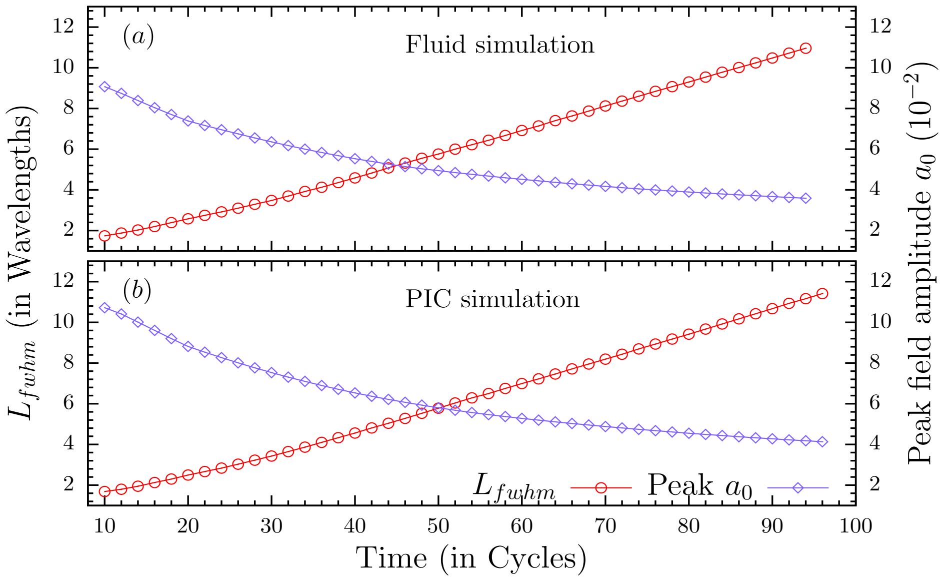

Figure 5.3: *The temporal evolution of the pulse length (red circle, left axis) and the peak field amplitude (blue filled circles, right axis) as it propagates in the underdense plasma is compared by fluid (a) and PIC simulations (b). The pulse length L_{fwhm} is estimated in units of the fundamental wavelength of the laser pulse, similarly time is presented in units of fundamental laser cycle. The laser and plasma conditions are same as Fig. 5.2.*

[188] is carried out to compare the results of the cold fluid model. In this code the electric fields are normalized as we earlier discussed ($a_0 = eE/m_e\omega c$). However space and time are taken in units of laser wavelength (λ) and one laser cycle $\tau = \lambda/c$ respectively, mass and charge are normalized with electron mass and charge respectively. We have used 100 cells per laser wavelength with each cell having 50 electron and ion macro-particles. The spatial grid size and temporal time step for the simulation are considered to be 0.01λ and 0.01τ respectively.

5.2 Results and Discussion

We have numerically solved the Eqs. (5.1)-(5.5) in the same sequence to study the evolution of the laser pulse entering the simulation box from the left side as shown in Fig. 5.1. The simulation box of length $100\ \lambda$ is considered, with a constant unperturbed plasma density n_0 throughout the simulation domain (Fig. 5.1(a) and (b)), the linearly polarized Gaussian laser pulse of wavelength

800 nm has a full width half maximum (FWHM) duration of 3 cycles ($\tau_{fwhm} = 3 \times 2\pi$). The normalized amplitude a_0 is varied in the different simulations shown in Fig. 5.1, and the boundary conditions on the left side read as:

$$\mathbf{a}(0,t) = a_0 \exp\Big(- \frac{4\log(2)t^2}{\tau_{fwhm}^2}\Big) \cos(t) \;\; \hat{\mathbf{x}} \tag{5.6}$$

$$n_e(0,t) = n_0 \tag{5.7}$$

$$\beta(0,t) = \varphi'(0,t) = 0 \quad (\varphi' \equiv \partial\varphi/\partial z). \tag{5.8}$$

It should be noted that the cold fluid relativistic model is only valid for the cases when the laser pulse amplitude is a_0 is less than unity ($a_0 < 1$) or for that matter the dispersion is in the linear regime. For ultraintense laser pulses $a_0 > 1$, the phenomenon of the wave breaking and other non-linearities limit the applicability of the fluid approach in describing the density modulations. The results in this sections are divided in for the cases when $a_0 < 1$ wherein we compared the results of the fluid and PIC simulations along with the effects of the laser and plasma parameters on the dispersion of EM waves. On the contrary the dispersion of the ultraintense laser pulses ($a_0 > 1$) is studied by only using PIC simulations.

5.2.1 Pulse dispersion for $a_0 < 1$

As shown in Fig. 5.1(a), we consider the propagation of the 800 nm, 3 cycles (FWHM), linearly polarized, Gaussian laser pulse ($a_0 = 0.1$) in the plasma with an unperturbed plasma density of $0.5n_c$. The spatial profiles of the transverse EM fields and longitudinal electrostatic fields are illustrated at different time instances in Fig. 5.2 both by using fluid simulation (left panel) as well as PIC simulations (right panel), and apparently the agreement between the two is found to be good. The dispersive nature of the laser pulse can be seen by increased pulse length and decreased peak amplitudes as estimated at different time instances. As it propagates deeper into the plasma the pulse tend to broaden. Furthermore, it can be seen from Fig. 5.2(b) that the wakefield or longitudinal field generation is suppressed for the chosen laser and plasma parameters and on the contrary a kind of a localized structure is co-propagating

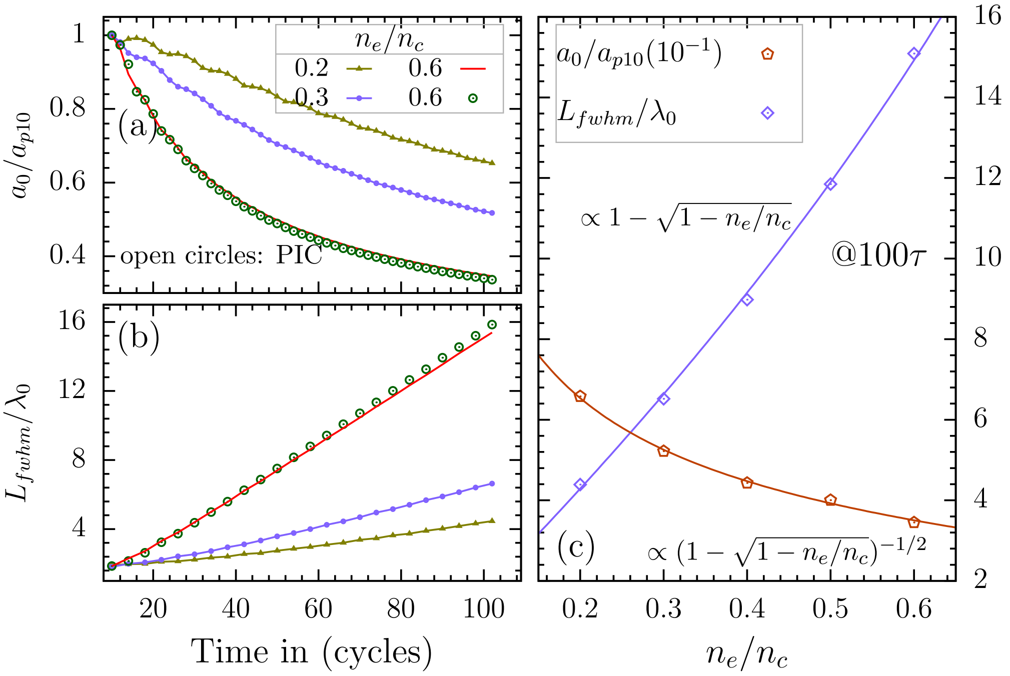

Figure 5.4: *Temporal evolution of the peak laser amplitude (a) and pulse length (b) is presented for different plasma densities. The results of the PIC simulations are also shown with open circles in both (a) and (b). The peak amplitude is normalized to the peak value of the pulse at* $t = 10\tau$ (a_{p10}). *The value of these parameters are evaluated at 100*τ *are also presented in (c) for different* n_e/n_c. *The* $a_0 = 0.1$ *and* $\tau_{fwhm} = 3$ *cycles is considered for this case.*

with the laser pulse [see Fig. 5.2(a)]. The suppression of the wakefield happens mainly when the length of the laser pulse ($c\tau_L$) is larger than the equivalent length of the plasma oscillations ($\upsilon_g\tau_p$), here υ_g is the group velocity of the plasma waves and τ_p is the duration of the one plasma cycle. In Ref. [105], we have presented the detailed analysis of the transition from the wakefield to the soliton formation.

For the same laser and plasma parameters ($a_0 = 0.1, \tau_{fwhm} = 3$ cycles, $n_e = 0.5n_c$) the time evolution of the peak field amplitude and the pulse length is presented in Fig. 5.3, the agreement between the fluid and PIC simulations is found to be excellent. It can be observed from Fig. 5.3, that the pulse length increases almost linearly with time as the pulse propagates deeper into the plasma, on the other hand, the peak field amplitudes decreases. As we discussed earlier, for this laser and plasma parameters the wakefield generation is suppressed and the modulation in plasma density actually co-moves with

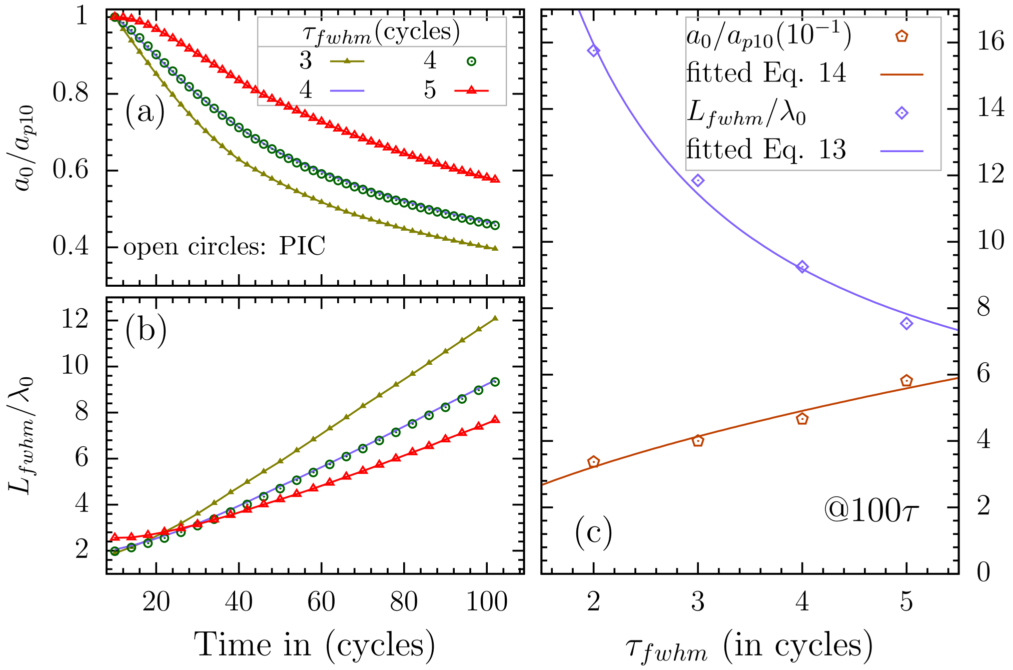

Figure 5.5: *Temporal evolution of the peak laser amplitude (a) and pulse length (b) is presented for different pulse duration. The results of the PIC simulations are also shown with open circles in both (a) and (b). The peak amplitude is normalized to the peak value of the pulse at it would be at* $t = 10\tau$ *(*a_{p10}*). The value of these parameters are evaluated at 100*τ *and are presented in (c) for different* τ_{fwhm}*. The* $a_0 = 0.1$ *and* $n_e = 0.5n_c$ *is considered for this case.*

the laser pulse. The total energy content of the pulse is found to be almost constant during its passage in the plasma, as energy lost to the wakefield generation is almost negligible.

Next, we present the effect of the plasma density on the temporal evolution of the pulse length and the peak field amplitude of the laser pulse, during its passage to the uniform density plasma. For this we have used the same laser parameters ($a_0 = 0.1$ and $\tau_{fwhm} = 3$ cycles) as in Fig. 5.2 and 5.3 with simulation domain presented in Fig. 5.1(a). The peak field amplitude is normalized to its value at $t = 10\tau$ (a_{p10}), this has been done to iron out a slight discrepancy with PIC simulations because anyway here we are more interested in the rate change of the peak amplitude as the pulse propagates through the plasma. The constant plasma density is varied from $0.2 - 0.6n_c$. It can be observed from Fig. 5.4(b) that the pulse length increases linearly with time and the rate at which it increases varies with the plasma density. We have compared the results of our

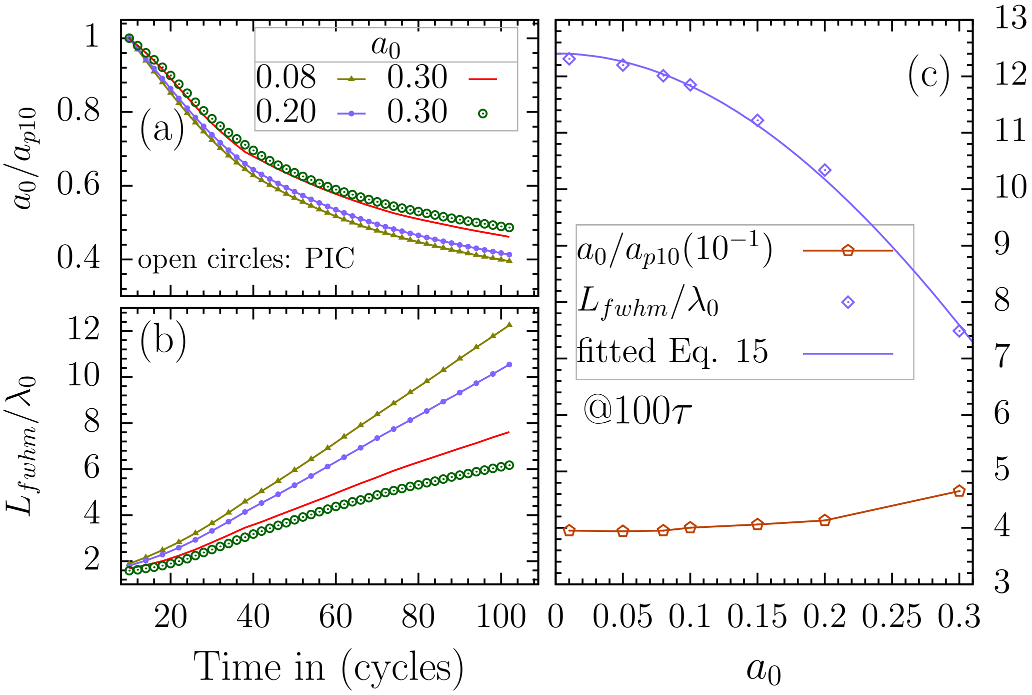

Figure 5.6: *Temporal evolution of the peak laser amplitude (a) and pulse length (b) is presented for different laser amplitudes. The results of the PIC simulations are also shown with open circles in both (a) and (b). The peak amplitude is normalized to the peak value of the pulse at it would be at* $t = 10\tau$ *(*a_{p10}*). The value of these parameters are evaluated at 100*τ *and are presented in (c) for different* a_0*. The* $n_e = 0.5n_c$ *and* $\tau_{fwhm} = 3$ *cycles is considered for this case.*

fluid simulation with the PIC simulation for the case with $n_e = 0.6n_c$ and the agreement is found to be excellent. In Fig. 5.4(c) we present the pulse length and the peak amplitude as evaluated at $t = 100\tau$ for different plasma densities.

The linear broadening of the laser pulse with time can be understood in terms of the group velocity of the pulse in the plasma. In the linearized theory the group velocity (normalized to c) can be calculated as:

$$\upsilon_g = \sqrt{1 - \omega_p^2/\omega^2} = \sqrt{1 - n_e/n_c} \tag{5.9}$$

then the time evolution of pulse length (L) can be expected to follow the relation,

$$L(t) = L_0 + (1 - \upsilon_g)t \tag{5.10}$$

such, that in case of vacuum ($\upsilon_g = 1$) the pulse length remains constant, say

L_0. As we have pointed out that for this cases the wakefield generation is almost suppressed and the energy content of the laser pulse is almost constant, this indicates toward the fact that as the pulse broadens, the respective peak amplitude should drop accordingly. The energy of the pulse will scale as $\propto a_0^2 L$, which indicates the drop in the peak amplitude scales as $\propto 1/\sqrt{L(t)}$.

The scaling is found to be in accordance with the results presented in Fig. 5.4(a). Furthermore, the variation of the pulse length (as evaluated at $t = 100\tau$) with the plasma density is presented in Fig. 5.4(c). As expected from Eq. 5.10, the pulse length and pulse amplitude would scale as:

$$L(n_e) \propto 1 - \sqrt{1 - n_e/n_c} \quad ; \quad a_0 \propto \frac{1}{\sqrt{L(n_e)}} \tag{5.11}$$

the fitted Eq. 5.11 is also illustrated in Fig. 5.4.

The effect of the pulse duration on the dispersion is presented in Fig. 5.5. Here, again we studied the time evolution of the pulse length and the peak field amplitude during the passage of the pulse through the plasma. We varied the τ_{fwhm} for fixed $a_0 = 0.1$ and $n_e = 0.5n_c$, for simulation domain shown in Fig. 5.1(a). The results are also compared with the PIC simulations as well and an agreement is found to be excellent. It can be seen from Fig. 5.5(c) that the length of the pulse at say $t = 100\tau$ decreases as we increase the laser pulse duration. It can be understood as follows, we know the shorter the pulse higher would be the bandwidth, that translates to the fact that a different portion of the pulse will propagate with the different velocity and as a result the larger broadening of the pulse. On the other hand for longer pulses the bandwidth is small, and so the associated dispersion. We can compare the time scales of the laser pulse duration with the time scales typically involved in the plasma oscillations $\tau_{fwhm} \propto 1/\omega_p \sim 1/\sqrt{n_e}$ for a rough estimates related to the dispersive nature of the plasma.

$$\tau_{fwhm} \propto \frac{1}{\sqrt{n_e}} \tag{5.12}$$

however, as we saw earlier the pulse length is related to the plasma density as given by Eq. 5.10, so in a sense $n_e \propto L^2$, this implies

$$\tau_{fwhm} \propto \frac{1}{L} \implies L \propto \frac{1}{\tau_{fwhm}} \tag{5.13}$$

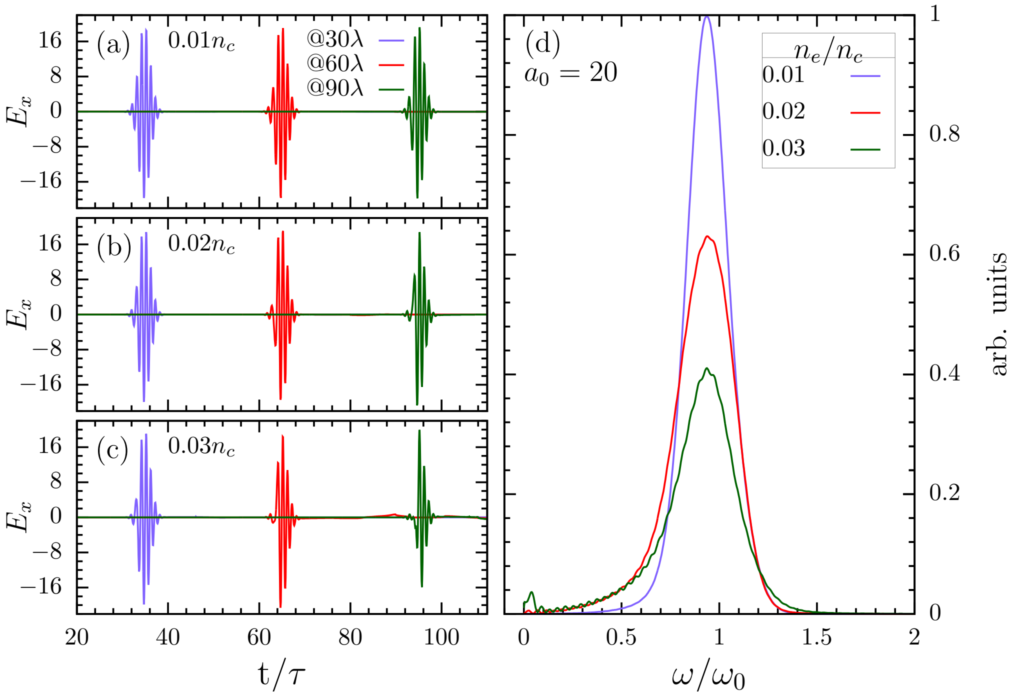

Figure 5.7: *The temporal snapshots of the laser field as evaluated at 30, 60 and 90*λ *is illustrated for the case when 3 cycle laser with* $a_0 = 20$ *is propagating in the plasma with density 0.01*n_c *(a), 0.02*n_c*(b) and 0.03*n_c*(c). The Fourier spectrum of the laser pulse as evaluated at* 90λ *is also compared for different plasma densities (d).*

and peak amplitude would be,

$$a_0 \propto \frac{1}{\sqrt{L}} \propto \sqrt{\tau_{fwhm}} \tag{5.14}$$

Next, we further study the effect of the laser amplitude on the dispersion of the laser pulse with the same simulation domain as shown in Fig. 5.1(a). For this purpose we fixed the pulse duration to $\tau_{fwhm} = 3$ cycles and the plasma density to $0.5n_c$ and varied the peak laser amplitude. The time evolution of the peak field amplitude and length of the laser pulse is presented in Fig. 5.6. Again as expected the linear dispersion law is found to be consistent for the laser and plasma parameters presented. Though for $a_0 = 0.3$ case, we found a bit of discrepancy with fluid simulation for pulse length evolution, otherwise the rate change of the field amplitude is consistent with the findings of the PIC simulations. The value of the field amplitude and pulse length as evaluated at 100τ is also illustrated in Fig. 5.6(c). It is understood that high intensity laser pulses tend to disperse less as compare to the low amplitude pulses, as a consequence the pulse length of the intense pulses is smaller than then their low intensity counterpart after certain time of propagation. As we discussed earlier, the pulse length can be estimated by Eq. 5.10, however with the relativistic corrections the Eq. 5.10 is modified as,

$$L(t) = L_0 + \left(1 - \sqrt{1 - \frac{n_e}{\gamma' n_c}}\right)t \quad ; \quad \gamma' \equiv \sqrt{1 + a_0^2} \tag{5.15}$$

here, γ' is relativistic factor (Eq. 5.4), we ignored the longitudinal motion of the electrons. The scaling of the pulse length with the initial laser amplitude is carried out using Eq. 5.15 and the fitted curve is also presented in Fig. 5.6(c).

5.2.2 Pulse dispersion for $a_0 > 1$

In the previous section, we discussed the dispersion of the laser pulses with $a_0 < 1$. We developed an analytical framework based on the cold relativistic fluid model and benchmarked the results with the 1D PIC simulations. However, for high intense laser pulses, the cold fluid model is no longer valid, as for intense laser fields the nonlinear phenomenon like wave-breaking would prevail, which indeed is outside the purview of the fluid approach. In order to study the dispersion of the intense laser pulses ($a_0 > 1$) we would be using the PIC simulations alone.

We consider the propagation of 3 cycles (τ_{fwhm}), linearly polarized, Gaussian pulse with the peak field amplitudes as $a_0 = 10, 15$ and 20 in the plasma with uniform density $\lesssim 0.03 n_c$ as shown in Fig. 5.1(b). The reason to consider the lower plasma density (as compared to the previous section) for $a_0 > 1$ is to mitigate the formation of the overdense plasma ($n_e > n_c$) caused by the ponderomotive force exerted by intense laser pulses $a_0 \gtrsim 10$. The overdense plasma then prohibits the further propagation of the laser pulses, till it becomes sufficiently underdense (by space-charge effect) to allow the passage of the laser pulse. For this kind of scenario we might have the reflections of the laser pulse from the different part of the plasma, where it turns overdense. In order to avoid any reflections by the formation of the overdense plasma, in this section we would be considering the plasma densities $\lesssim 0.03 n_c$.

We compared the time evolution of the laser ($a_0 = 20$) electric field for

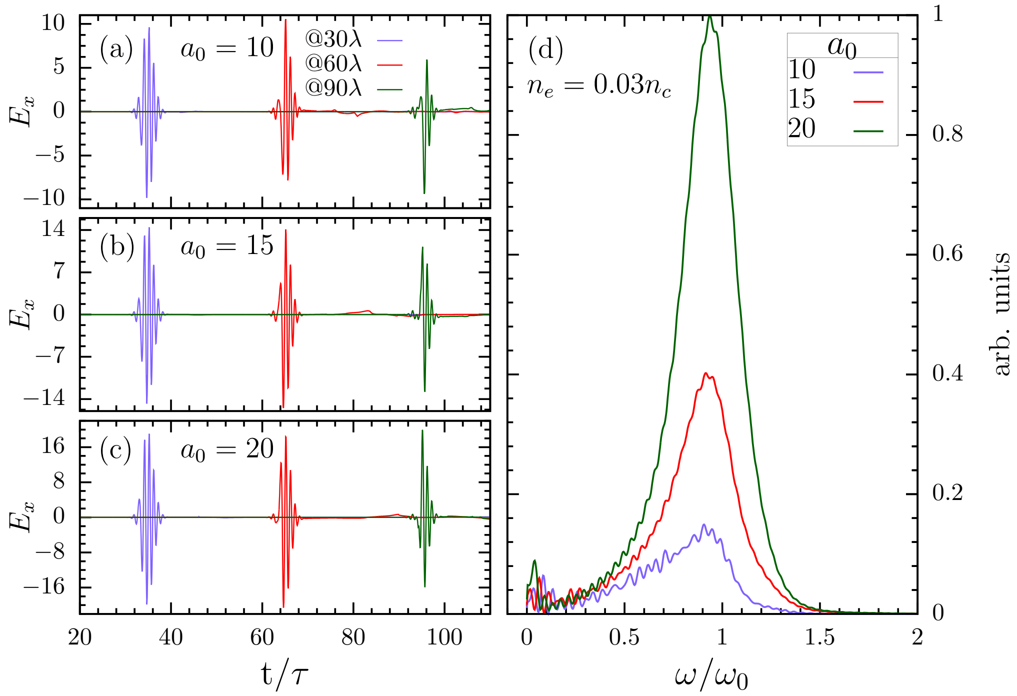

Figure 5.8: *The temporal snapshots of the laser field as evaluated at 30, 60 and 90λ is illustrated for the 3 cycle laser propagating in the plasma with density 0.03*n_c*. The laser amplitude* $a_0 = 10$ *(a), 15(b) and 20(c) are considered. The Fourier spectrum of the laser pulse as evaluated at* 90λ *is also compared for different laser amplitudes (d).*

three different plasma densities in Fig. 5.7. The field profiles are evaluated after the laser propagated the distances 30λ, 60λ and 90λ in the plasma. It can be observed from this figure that the peak of the envelope moves roughly with the same velocity for different plasma densities, this indicates that the group velocity of the laser is more or less unaffected for the considered laser and plasma parameters, or maybe it would require longer simulation to see any prominent effect on propagation. We have also presented the Fourier spectrum of the laser pulse in Fig. 5.7(d). It can be seen that for higher densities the broadening of the frequency spectrum is larger because of the stronger plasma wave generation. The spectrum is found to be red shifted in direct correlation with the plasma density [200]. The red shifting and broadening of the spectrum generally accounts for the stronger plasma wave generation, because of the energy transformation from the laser to the plasma. This fact can also be observed from the Fig. 5.7(d), wherein the red shift for higher density plasma is larger as compared to the lower density plasma. In order to elucidate the effect of the laser pulse amplitude on the dispersion of the laser pulse, in Fig.

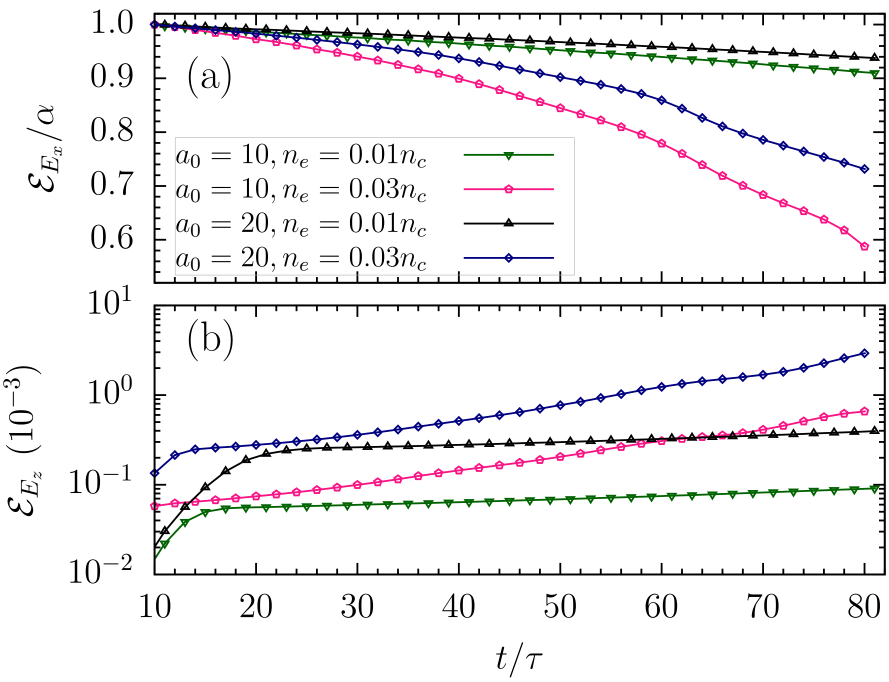

Figure 5.9: *Temporal evolution of the laser pulse energy (a) and the longitudinal field energy (b) is presented for 3 cycle Gaussian pulse with* $a_0 = 10,\ 20$ *when it propagated in the plasma with density* $0.01,\ 0.03n_c$*. The laser pulse energy in (a) is normalized to maximum value at* $t = 10\tau$*, as we are interested in the depletion rate of the laser pulse energy for different laser and plasma parameters.*

5.8 we have varied the laser pulse amplitude while keeping the plasma density fixed at $0.03n_c$. The broadening of the spectrum is seen to be prominent for the $a_0 = 10$ as compare to $a_0 = 20$, because the rate at which the energy is depleted for lower laser amplitudes would be larger as compared to higher laser amplitudes.

The time evolution of the electromagnetic and electrostatic field energies are presented in Fig. 5.9. Here, again we have considered the propagation of the 3 cycle, linearly polarized laser pulse with $a_0 = 10, 20$ in the plasma having densities $0.01, 0.03n_c$ presented in Fig. 5.1(b). As time progress the decrease in the electromagnetic field energy and increase in the electrostatic field energy is observed which indicates toward the stronger plasma wave generation at the cost of the electromagnetic energy. As expected it is further observed that the depletion rate of the electromagnetic field energy is larger for the laser with peak amplitude $a_0 = 10$ as compare to $a_0 = 20$. This is so because the dispersion of the high intensity laser pulses would be relatively slower than the laser pulses with lower intensity. The direct correlation of the plasma density can also be seen on the depletion rate of the electromagnetic field energy, and so the growth in the longitudinal field energy.

5.3 Ion Acceleration by Intense Dispersed Pulses

In the previous section, the dispersion of the laser pulse as it propagates in the underdense plasma was discussed. Here, the main focus was to study the dispersion of pulse as it propagates in the underdense plasma, therefore, the plasma densities are restricted to $\lesssim 0.03n_c$. Otherwise, some reflections were observed during the passage of the pulse, which might affect the Fourier spectrum of the pulse. Nevertheless, in this section our main focus is not to study the fourier spectrum of the pulse but rather the application of the dispersed pulses in accelerating the ions, and for that we have varied the plasma densities till $\sim 0.2n_c$.

We have recently demonstrated the use of the negatively chirped laser pulses to accelerate the ions to a few hundreds of the MeV by using a double layer (Hydrogen plasma) target [89]. The primary layer having density $6n_c$ is found to be transparent for the negatively chirped laser pulse with $a_0 = 20$, creating a persistent electrostatic field which actually accelerates the ions from the secondary layer ($0.1n_c$).

We deploy the similar geometry of two layer target just after the low density plasma. The propagation of the laser pulse in underdense plasma actually causes the dispersion of the pulse, as a result the pulse would be chirped [201]. The dispersed or the chirped pulse then incidents on the two-layer target. In Fig. 5.10, the energy spectrum of the ions from the secondary layer is compared for the cases when there is no underdense plasma and when the laser propagated through the underdense plasma. We present the energy spectrum of the ions from the secondary layer as evaluated at 170τ. For this, the diagrammatic representation of simulation domain is presented in Fig. 5.1(c). Here, we considered the interaction of a 3 cycle, linearly polarized Gaussian laser pulse with $a_0 = 20$. The pulse propagates in the 50λ long underdense Hydrogen plasma having density n_0 and then interacts with the two-layer composite target, the

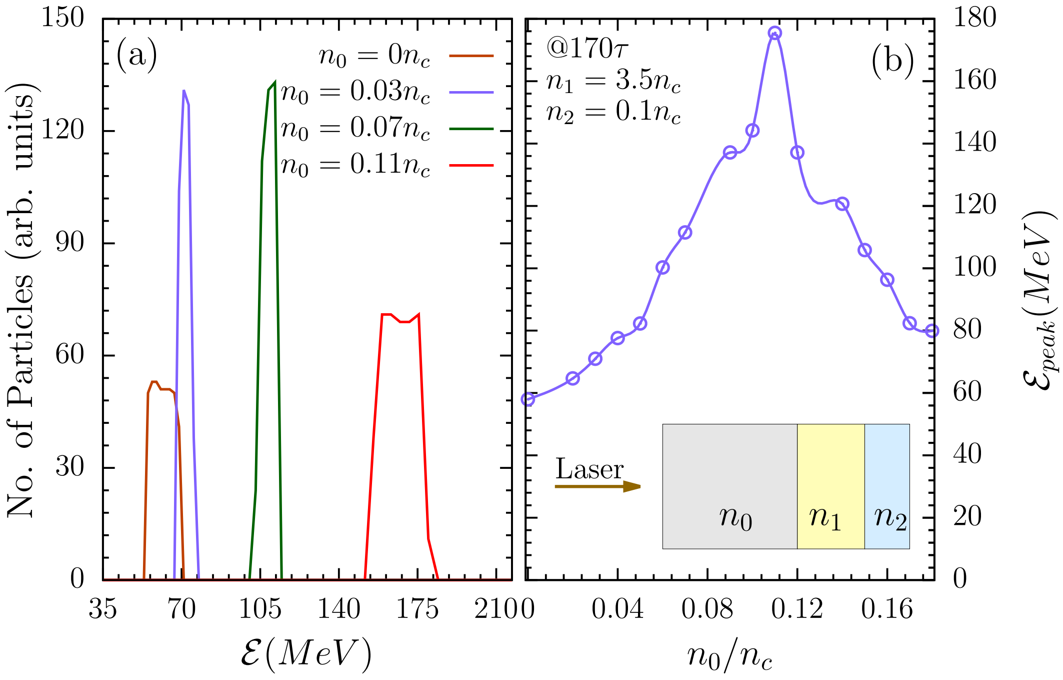

Figure 5.10: *The energy spectrum of the ions from the secondary layer as evaluated at 170τ are presented for different pre-target plasma densities (a). The variation in the peak energy of the ions from the secondary layer with pre-target plasma density (n_0) is illustrated (b). We have used 3 cycles, Gaussian, linearly polarized laser with peak amplitude $a_0 = 20$. The geometry of the setup is also illustrated as an inlet, here n_0, n_1 and n_2 respectively represents the pre-target plasma density, density of the primary layer and secondary layer.*

first layer is considered to be 0.75λ thick with density $n_1 = 3.5n_c$ (Deuterium) and adjacent secondary layer is 0.2λ thick with density $n_2 = 0.1n_c$ (Hydrogen) [see Fig. 5.10(b). It can be observed from Fig. 5.10(a) that the energy of the ions from the secondary layer in the absence of any underdense plasma ($n_0 = 0n_c$) is $\sim$ 60 MeV, which increases to $\sim$ 75 MeV and $\sim$ 170 MeV respectively for $n_0 = 0.03n_c$ and $n_0 = 0.11n_c$. The effect of the underdense plasma (pre-target plasma) density on the peak energy of the ions from the secondary layer is also illustrated in Fig. 5.10(b), where an optimum underdense plasma density for the efficient acceleration of the ions from the secondary layer is presented.

The enhanced acceleration of the ions from the secondary layer is basically due to the dispersion of the laser pulse, wherein the frequency of the pulse undergone the modulation in space and time. The critical density for the transmission gets modified for the chirped laser pulses, assisting the transmission

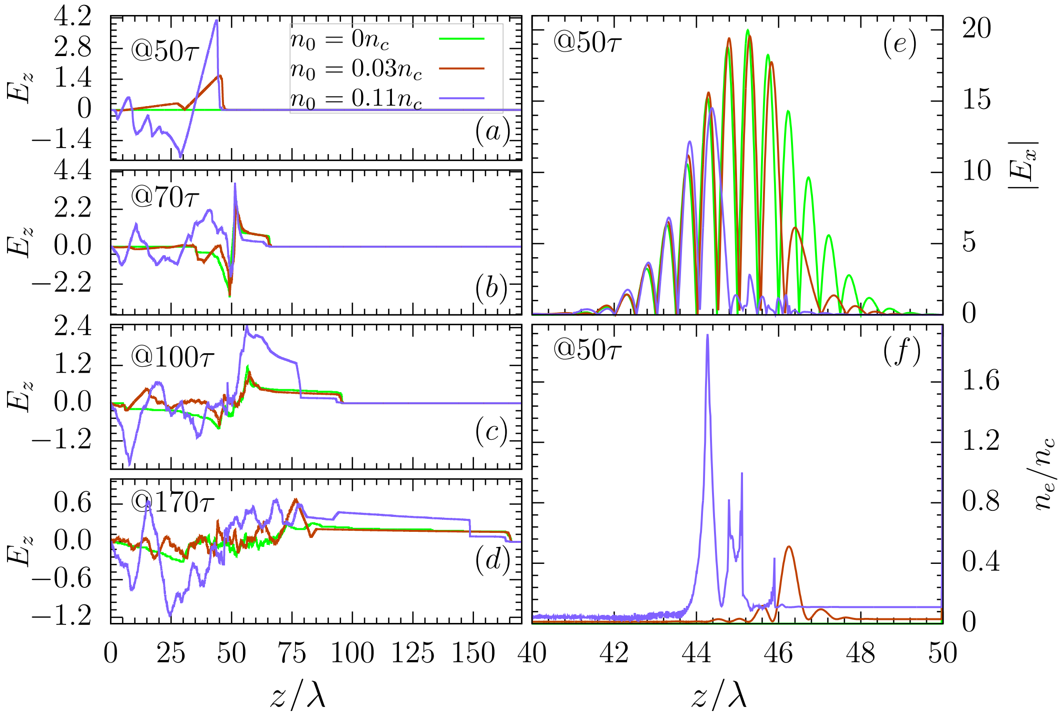

Figure 5.11: *The spatial profile of the longitudinal electrostatic field is presented at different time instances for different underdense plamsa densities. The spatial profile of the transverse electric field (e) and electron density (f) profiles are also presented as evaluated at 50τ. The laser and target parameters are same as mentioned in Fig. 5.10.*

of the pulse through the two-layer targets, despite the reduction in the laser pulse energy through wakefield generation in underdense plasma. The transmitted pulse drags the electrons from the underdense plasma in addition to electron from both the layers, creating a very persistent longitudinal electrostatic field behind the target [89]. The electrostatic field created behind the target then pulls the ions from the secondary layer, forming the mono-energetic ion bunch. The density of the underdense plasma (n_0) plays a crucial role in determining the dispersion and so the effective chirping of the laser pulse, as a result, the ion acceleration mechanism as a whole would be affected by the density of the underdense plasma. It can be understood that if $n_0/n_c \rightarrow 0$ i.e. the pre-target plasma density is too low, then in that case the frequency shift and the dragged electrons would be too marginal to account for any significant formation of the electrostatic field behind the composite target. On the other hand if $n_0/n_c \rightarrow 1$, then the fraction of the laser pulse energy which interacts with the primary layer would itself be low enough to cause any significant

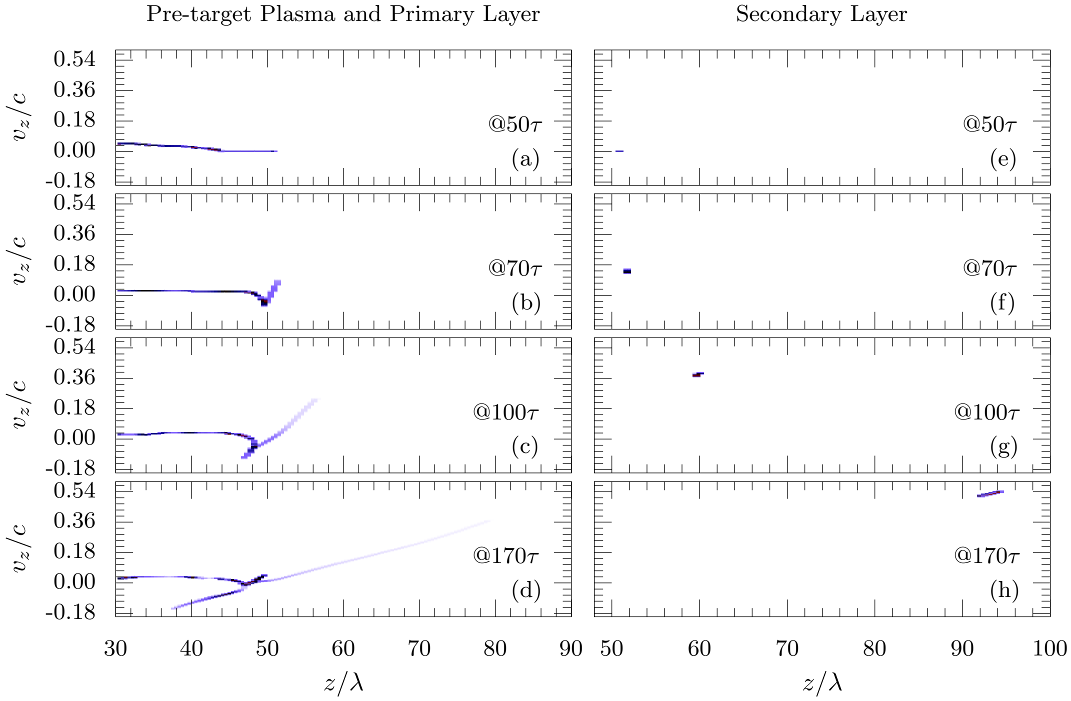

Figure 5.12: *The phasespace plots of ions from the pre-target plasma along with the primary layer (left column) and the secondary layer (right column)are presented at different time instances from* 50τ *to* 170τ*. The pre-target layer is of Hydrogen with thickness of* 50λ *and density* $n_0 = 0.11n_c$ *. The primary layer is comprised of Deuterium plasma of* 0.75λ *and* $n_1 = 3.5n_c$*; along with the secondary layer Hydrogen having thickness and density respectively* 0.2λ*,* $0.1n_c$*.*

heating of the electrons of primary layer. This indicates toward an optimum pre-target plasma density, which would introduce the necessary chirp to the laser pulse and at the same time will retain the appropriate intensity of the pulse to benefit from the RSIT, and in return will cause efficient acceleration of the ions from the secondary layer. If the laser pulse suffers the complete reflection at the primary layer then acceleration of the ions is mostly caused by the radiation pressure mechanism, resulting in a lower energy yield for the same laser intensity [87].

In order to shed some light on the mechanism of the ion acceleration, the longitudinal and transverse field profiles along with the electron density are illustrated in Fig. 5.11. The laser pulse profile as evaluated at 50τ is illustrated in Fig. 5.11(e), along with the respective electron density in Fig. 5.11(f). It can be understood from this figure that for $n_0 = 0.11n_c$, the dispersion of the laser pulse is strong as compared to lower densities which also manifests in enhanced electron density just before the primary layer target. As the laser pulse transmits through the target, it drags the electrons from the underdense plasma region, which further boosts the longitudinal electrostatic field as can be seen from Fig. 5.11(a), (b) and (c). However, if the pre-target plasma density is further increased, then the pulse energy would be dissipated before it can reach the target. This very fact can be also seen in Fig. 5.10(b), where we obtained the optimum pre-target plasma density for efficient acceleration.

The phase space of the ions from the primary and secondary layer at different time instances are presented in Fig. 5.12. The laser pulse propagates in 50λ thick underdense plasma region ($n_0 = 0.11 n_c$), as a result, we do not see any motion of the ions from the primary and pre-target layer. As the pulse interacts with the primary layer, the electrons from the pre-target plasmas are also dragged along [refer, Fig. 5.11(f)], as a result, a strong electrostatic field created [refer, Fig. 5.11(c)] which eventually accelerates the ions of the secondary layer mono-energetically. The ions from the primary layer are also seen to be accelerated to higher energies, however the density of the primary layer ($n_1 = 3.5 n_c$) is responsible for the prominent space charge effect, and as a result, they expand under their own coulomb repulsion. The ions from the secondary layer are seen to be accelerating with ~ 170 MeV [refer, Fig. 5.10(a)], and the rapid broadening of the bunch is prevented by the initial lower density of the secondary layer ($n_2 = 0.1 n_c$).

As we have seen, the ions from the secondary layer are found to be accelerated to $\sim$ 170 MeV using 3 cycle Gaussian, linearly polarized laser with $a_0 = 20$ [see, Fig. 5.10(a)]. In Ref. [87], the authors have also considered the double layer geometry. They have reported the proton acceleration to $\sim$ 210 MeV using a super-gaussian laser pulse with $a_0 \sim 112$. The acceleration using a nano-structured double layer targets is reported in Ref. [76]. They have relied on the Radiation Pressure of the laser with $a_0 \sim 100$ to remove all the electrons from the primary Carbon target and the protons from the secondary layer are found to be accelerated to a few hundreds of MeV. Robinson et. al. [27] have demonstrated the ion acceleration in the HB-RPA regime, where the proton energies ~ 150 MeV is obtained by laser with $a_0 \sim 90$. In the RPA regime, ion acceleration to ~ 150 MeV with $a_0 = 108$ has been reported in Ref. [191]. On the contrary, as we have observed [see, Fig. 5.10], these energy ranges are accessible using $a_0 \sim 20$ (with discussed dispersion and associated ion acceleration through RSIT) as compare to $a_0 \sim 112$ [87] and $a_0 \sim 100$ [76].

5.4 Summary

We have studied the dispersion of the laser pulse as it propagates in the underdense plasma. For the moderate laser intensities ($a_0 < 1$) we invoked a 1D relativistic cold fluid model to evaluate the spatial and temporal evolution of the laser as it propagates in the plasma with density $\lesssim 0.6n_c$. Apart from the immobile ions, no further approximations are made. The effect of the laser pulse amplitude, pulse duration and the plasma density is explored using the fluid model and the results are compared with the 1D PIC simulations along with the expected scaling laws. The agreement between fluid model and the PIC simulations are found to be excellent. Furthermore, in order to study the interaction of highly intense laser pulses $a_0 \gtrsim 10$, we only relied on the PIC simulations as the nonlinear nature of the interaction process is beyond the validity of the cold relativistic fluid model. For these cases, we restricted to the plasma density $\lesssim 0.2n_c$, or the strong ponderomotive force of laser pulses tend to make plasma overdense ($n_e > n_c$) restricting the further propagation of the laser pulse. The conversion from the electromagnetic field energy to the electrostatic fields in the form of plasma waves results in the dispersion and so the red shift of the pump laser pulses. The dispersed pulse then allowed to incident on the sub-wavelength two-layer composite target. The underdense plasma before the target regulates the dispersion of the pulse. We observed an optimum pre-target plasma density ($n_0 = 0.11n_c$) which results in the acceleration of the ions from the secondary layer to ~ 170 MeV by a 3 cycle linearly polarized Gaussian laser pulse with $a_0 = 20$. For lower pre-target densities the dispersion is not prominent enough to cause significant electrostatic field formation, however for higher pre-target densities, the pulse itself will loose energy to the wakefields before it can interact with the target.

CHAPTER 6

Summary and Future Scope

Summary

The laser induced particle acceleration is a field of contemporary research, promising various applications in both fundamental and applied sciences. To understand the laser induced particle acceleration, different mechanisms have been proposed in the past like LWFA [2], SMLWFA [113], TNSA [16, 134], BOA [109], LS-RPA [28, 29], HB-RPA [163] etc. In this thesis, we have investigated the ion acceleration by intense laser pulse through Relativistic Self-Induced Transparency (RSIT) [79, 180] mechanism. The advantage of using this mechanism is that, it provides similar range of energy with comparably low laser intensity than relative acceleration mechanisms. This chapter summarizes the main results of our investigations on the process of RSIT enabled ion acceleration. Along with this we would like to acknowledge possible future directions in the area that can be pursed, in order to improve our understanding of the field.

In Chapter 2 we have discussed several acceleration mechanism that have been proposed over the decade, to obtain the significant ion or electron energies. Various parameters (such as laser and target conditions) have influenced the generation of high energetic proton beams or bunches. To have the basic understanding of the ion acceleration using ultra-intense laser pulses through relativistic self-induced transparency regime, we have numerically solved the cold relativistic fluid model and compared the results with the PIC simulations. In this regime of ion acceleration, an ultra-intense laser pulse causes the increase of the effective mass of the electrons via relativistic effects, which effectively lowers the threshold density of the plasma target, thereby making the target transparent for the laser pulse. It is being observed that for subwavelength targets the threshold target density for a particular laser amplitude and

target thickness increases as compare to thick targets. The relativistic factor γ_e plays a vital role in predicting the target threshold density, due to its dependence on laser pulse amplitude a_0 and longitudinal electron momentum p_z^e. From this, it can be inferred that electron heating (p_z^e) too plays a very vital role in RSIT. The dimensionless parameter $\zeta = (n_e/n_c)(d/\lambda)$ is defined in Refs. [28], is composed of the plasma target density and critical density (n_e, n_c) for laser wavelength(λ) and target thickness (d). The interplay between laser pulse amplitude (a_0) and ζ is of great significance in order to understand the regime of ion acceleration (i.e., LS or RSIT). If the ratio of $a_0/\zeta \gtrsim 1$ the RSIT mechanism dominates, on the contrary, LS regime of ion acceleration prevails for $a_0/\zeta < 1$
.

We also observed that the use of composite two-layer target is more favorable than the single layer, in order to have an efficient ion acceleration. This is so, because in a single layer all the electrons are expelled from the target thereby leaving it positively charged, which further manifests in the coulomb explosion. The target ions expand in either the direction, resulting in the broad energy spectrum. Whereas, with the double layer target geometry the mono-energetic ion bunches of the order of few hundreds of MeV are obtained. The optimization of the target parameters is a very crucial aspect in order to have maximum ion energy. The balancing of the laser ponderomotive force and the electrostatic forces is the requirement for the RSIT to prevail. The suitable scaling law was obtained for maximum ion energy by varying the target density, thickness and laser pulse amplitude. Furthermore, it was observed that the RSIT could cause the ions of the similar energy with comparatively lower intensity (around 2.5 times less) than other acceleration mechanisms such as, Radiation Pressure Acceleration, Direct Coloumb Explosion mechanism [27, 76, 202].

Next, we have studied the effect of laser pulse chirp on the acceleration of protons from similar composite two-layer target geometry through RSIT. The chirped pulses are those pulses, which shows the temporal variation about its fundamental frequency. In the negatively (positively) chirped pulse, the high (low) frequency component of the pulse interacts with the target initially followed by the low (high) frequency component. The temporal variation of the frequency in the chirped laser pulse manifests in the associated time-dependent critical density; as a consequence, the threshold plasma density of the negatively chirped laser pulse is found to be comparatively higher than the unchirped and positively chirped laser pulses. The initial low-frequency interaction of the positively chirped pulse with the target tends to compress the target layer by the radiation pressure; as hence the target is found to be opaque for positively chirped pulses.

Furthermore, as the negatively chirped pulse transmits through the target, the suppression of the $\mathbf{J} \times \mathbf{B}$ heating by the circularly polarized laser results in longitudinal push on the electrons; as a result, few electrons get dragged away and start co-moving with the laser pulse. This imbalance leaves the target positively charged followed by the expansion of the target ions under its own coulomb repulsion. However, the removal of the electrons also generates a very stable and persistent electrostatic field behind the primary layer which can be harnessed by the composite target geometry, comprised of the low density, thin secondary layer adjacent to the primary layer. The ions from the secondary layer are found to be accelerated as a bunch under the effect of the longitudinal field created by the primary layer. For the analysis we have used the chirp model which is beyond linear approximation. The chirped laser pulse results in the enhanced effective transmission of laser pulses for $a_0 < 1$ and $a_0 \gg 1$. The transmission coefficient for $a_0 < 1$ is calculated by the simplified wave propagation model, where the effect of longitudinal electron momentum was neglected. The results of the wave propagation model are compared with the PIC simulations and agreement is found to be excellent. However, for intense laser pulses ($a_0 \gg 1$), the wave propagation model cease to valid due to different non-linearities involved in the interaction processes, e.g. longitudinal electron heating, and hence we relied on the PIC simulations for $a_0 \gg 1$ case.

We studied the interaction of highly intense laser pulse ($a_0 \gg 1$) with the subwavelength targets under RSIT regime. It was seen that the threshold target density increases for the negatively chirped laser pulse rather than unchirped and positively chirped laser pulse. The electrostatic field created by this negatively chirped pulse for target thickness 0.75λ and density $6n_c$ is found to very stable and persistent for the time scales of the interest. We have also carried out the optimization of the target parameters and the maximum energy of the protons from the thin, low density layer is found to be 100 MeV for 10 fs (intensity FWHM); Circularly Polarized; Gaussian; negatively chirped laser pulse with peak intensity $\sim 8.5 \times 10^{20} W/cm^2$.

Furthermore, we studied the propagation of laser pulse in an underdense plasma and the resultant ion acceleration due to this dispersed laser pulse. The propagation of laser pulse is investigated in two regimes, one is non-relativistic for the moderate laser intensities ($a_0 < 1$); and other is relativistic regime $a_0 \gtrsim 10$ for highly intense laser pulses. We have invoked a 1D relativistic cold fluid model to evaluate the spatial and temporal evolution of the laser as it propagates in the thick underdense plasma target of density $\lesssim 0.6 n_c$. For this model the ions are considered to be immobile and no further approximations are made. The effect of the laser pulse amplitude, pulse duration and the plasma density is explored using the fluid model and 1D PIC simulation code. The results obtained were very well fitted to the expected scaling laws and the agreement between fluid model and the PIC simulations are found to be excellent. The interaction of highly intense laser pulses $a_0 \gtrsim 10$ is studied via PIC simulations only, as the nonlinear nature of the interaction process is beyond the validity of the cold relativistic fluid model. The interaction of highly intense laser pulse with underdense plasma is restricted to the non-linear phenomenon such as wave breaking. The dispersion of pulse as it propagates in the underdense plasma is restricted to $\lesssim 0.03 n_c$, in order to avoid reflections during the passage of the pulse, which might affect the Fourier spectrum of the pulse. The conversion from the electromagnetic field energy to the electrostatic fields in the form of plasma waves, results in the dispersion and so the redshift of the pump laser pulses. The underdense plasma before the target regulates the dispersion of the pulse. Also, we have studied the role of these dispersed pulse to accelerate the ions to high energies when it is allowed to be incident on the sub-wavelength two-layer composite target. For this application, we have varied the underdense plasma density till $\sim 0.2 n_c$. Otherwise, the strong ponderomotive force of laser pulses tend to make plasma overdense, thereby restricting the propagation of the laser pulse. It was observed that for a given laser parameters there is an optimum pre-target plasma density ($n_0 = 0.11 n_c$), which assist the acceleration of the ions from the secondary layer to ~ 170 MeV by a 3 cycle linearly polarized Gaussian laser pulse with $a_0 = 20$. It is observed that for low pre-target densities the dispersion is not prominent enough to cause significant electrostatic field formation. On the contrary, for higher pre-target densities, the pulse looses its energy to the wakefields before it can interact with the main double layer target . In case of dispersed pulses, the ion energies are found to be significantly higher for a_0 = 20, against other acceleration mechanisms which uses a_0 = 112[87] and a_0 = 100 [76].

Future Scope

In this work we have only used one-dimensional fluid and PIC simulations to understand the underlying physics aspects of the Relativistic Self-Induced Transparency and associated ion accelerations. However, for experimental realizations of the idea it is expected to have the higher dimensional simulation results, which would perfectly complement the experimental needs. In view of this it will be interesting to observe and study the RSIT in more depth using the PIC codes such as EPOCH [203] or PICCANTE [204]. Furthermore, the optimization of the laser and target parameters will also crucial for the from the experimental design perspective. The study of the higher-order harmonics generation (HHG) via laser-solid interaction [205], the phenomenon of radiation reaction [206] caused by the sufficiently intense laser pulses can also be explored in future.

Appendix A

Relativistic Cold-Fluid Model - RSIT Mechanism

In coulomb gauge the Maxwell's equations will take the following form for vector potential $\mathbf{A}$ and scalar potential ϕ,

$$\nabla^2\phi = -\rho/\epsilon_0 \tag{A.1}$$

$$\nabla^2\mathbf{A} - \frac{1}{c^2}\frac{\partial^2\mathbf{A}}{\partial t^2} = -\mu_0\mathbf{J} + \frac{1}{c^2}\nabla\left(\frac{\partial\phi}{\partial t}\right) \tag{A.2}$$

$$\mathbf{J} = -en_e\mathbf{v_e} + Zen_i\mathbf{v_i} \tag{A.3}$$

$$\mathbf{v_e} = v_z^e\hat{z} + \mathbf{v_\perp^e} \tag{A.4}$$

$$\mathbf{v_i} = v_z^i\hat{z} + \mathbf{v_\perp^i} \tag{A.5}$$

where, all the symbols have their usual meaning. The index e and i denote the corresponding quantity associated with electrons and ions respectively. The longitudinal motion is considered to be along the laser propagation direction (z), however transverse motion is associated along the direction of laser polarization.

Using 1D approximations the above equations can be written as (z is direction of laser propagation),

$$\frac{\partial^2\phi}{\partial z^2} = \frac{-\rho}{\epsilon_0} \tag{A.6}$$

from Eq. A.2 to A.5 after separating perpendicular and longitudinal component we can write [laser pulse corresponds to vector potential $\mathbf{A}$ (transverse) and electrostatic field will correspond to ϕ (longitudinal)],

$$\frac{\partial^2\mathbf{A}}{\partial z^2} - \frac{1}{c^2}\frac{\partial^2\mathbf{A}}{\partial t^2} = \mu_0(en_e\mathbf{v_\perp^e} - Zen_i\mathbf{v_\perp^i}) \tag{A.7}$$

$$\frac{1}{c^2}\frac{\partial^2 \phi}{\partial t \partial z} = \mu_0(en_e v_z^e - Zen_i v_z^i) \tag{A.8}$$

Now Consider the Lorentz force equations,

$$\frac{d\mathbf{P}}{dt} = q(\mathbf{E} + \mathbf{v} \times \mathbf{B}) \tag{A.9}$$

$$\frac{d\mathbf{P}}{dt} = q\bigg[-\nabla\phi - \frac{\partial \mathbf{A}}{\partial t} + \mathbf{v} \times (\nabla \times \mathbf{A})\bigg] \tag{A.10}$$

$$\frac{d\mathbf{P}}{dt} = q\bigg[-\frac{\partial \phi}{\partial z} - \frac{\partial \mathbf{A}}{\partial t} - v_z\frac{\partial \mathbf{A}}{\partial z} + \bigg(\mathbf{v}_\perp . \frac{\partial \mathbf{A}}{\partial z}\bigg)\hat{z}\bigg] \tag{A.11}$$

and again comparing longitudinal and transverse components,

$$\frac{d\mathbf{P}_\perp}{dt} = q\bigg(-\frac{\partial \mathbf{A}}{\partial t} - v_z\frac{\partial \mathbf{A}}{\partial z}\bigg) = -q\frac{d\mathbf{A}}{dt} \Longrightarrow \mathbf{P}_\perp = -q\mathbf{A} \tag{A.12}$$

$$\mathbf{v}_\perp = \frac{-q\mathbf{A}}{m\gamma}; \gamma = \sqrt{1 + \frac{\mathbf{P^2}}{m^2c^2}} \tag{A.13}$$

$$\frac{dP_z}{dt} = -q\frac{\partial \phi}{\partial z} + q\bigg(\mathbf{v}_\perp . \frac{\partial \mathbf{A}}{\partial z}\bigg) \tag{A.14}$$

$$\frac{dP_z}{dt} = -q\frac{\partial \phi}{\partial z} - \frac{-q^2}{2m\gamma}\frac{\partial A^2}{\partial z} \tag{A.15}$$

$$\frac{\partial P_z}{\partial t} + \frac{P_z}{m\gamma}\frac{\partial P_z}{\partial z} = -q\frac{\partial \phi}{\partial z} - \frac{q^2}{2m\gamma}\frac{\partial A^2}{\partial z} \tag{A.16}$$

for electrons q = -e and for ions q = Ze.

Now considering below mentioned dimensionless units,

(a) $\mathbf{a} = e\mathbf{A}/(m_e c); \varphi = e\phi/(m_e c^2)$

(b) $n_{e,i} = n_{e,i}/n_c; n_c = \epsilon\omega^2 m_e/c^2$ (critical density)

(c) $\mathbf{p} = \mathbf{P}/(m_e c); x = kx; t = \omega t; v = v/c; m/m_e; q = q/e$

The following equations in dimensionless units can be written as,

$$\frac{\partial^2 \varphi}{\partial z^2} = n_e - Zn_i; \frac{\partial \varphi}{\partial z} = -E_z \tag{A.17}$$

$$\frac{\partial^2 \mathbf{a}}{\partial z^2} - \frac{\partial^2 \mathbf{a}}{\partial t^2} = \frac{n_e \mathbf{p^e_\perp}}{\gamma_e} - \frac{Z n_i \mathbf{p^i_\perp}}{\gamma_i m_i} \tag{A.18}$$

$$\frac{\partial^2 \varphi}{\partial t \partial z} = \frac{-\partial E_z}{\partial t} = -\left(n_e \frac{p_z^e}{\gamma_e} - Zni \frac{p_z^i}{\gamma_i m_i} \right) \tag{A.19}$$

now changes to,

$$\frac{\partial E_z}{\partial t} = \left(n_e \frac{p_z^e}{\gamma_e} - Zni \frac{p_z^i}{\gamma_i m_i} \right) \tag{A.20}$$

$$\mathbf{p^e_\perp} = a; \mathbf{p^i_\perp} = -Z\mathbf{a} \tag{A.21}$$

$$\frac{\partial^2 \mathbf{a}}{\partial z^2} - \frac{\partial^2 \mathbf{a}}{\partial t^2} = \left(\frac{n_e}{\gamma_e} + \frac{Z^2 n_i}{\gamma_i m_i} \right) \mathbf{a} \tag{A.22}$$

$$\gamma_e^2 = 1 + \mathbf{a}^2 + (p_z^e)^2; \gamma_i^2 = 1 + \frac{Z^2}{m_i^2} \mathbf{a}^2 + (p_z^i / m_i)^2 \tag{A.23}$$

$$\frac{\partial p_z^e}{\partial t} = \frac{\partial \varphi}{\partial z} - \left(\frac{1}{2\gamma_e} \frac{\partial \mathbf{a}^2}{\partial z} + \frac{p_z^e}{\gamma_e} \frac{\partial p_z^e}{\partial z} \right) \tag{A.24}$$

$$\frac{\partial p_z^i}{\partial t} = -Z \frac{\partial \varphi}{\partial z} - \left(\frac{Z^2}{2 m_i \gamma_i} \frac{\partial \mathbf{a}^2}{\partial z} + \frac{p_z^i}{m_i \gamma_i} \frac{\partial p_z^i}{\partial z} \right) \tag{A.25}$$

from Eq.A.23 it can be proved that,

$$\frac{\partial \gamma_e}{\partial z} = \frac{1}{2\gamma_e} \frac{\partial \mathbf{a}^2}{\partial z} + \frac{p_z^e}{\gamma_e} \frac{\partial p_z^e}{\partial z} \tag{A.26}$$

$$\frac{\partial \gamma_i}{\partial z} = \frac{Z^2}{2 \gamma_i m_i^2} \frac{\partial \mathbf{a}^2}{\partial z} + \frac{p_z^i}{\gamma_i m_i^2} \frac{\partial p_z^i}{\partial z} \tag{A.27}$$

equations for p_z will then be written as,

$$\frac{\partial p_z^e}{\partial t} = -E_z - \frac{\partial \gamma_e}{\partial z}; \frac{\partial p_z^i}{\partial t} = Z E_z - m_i \frac{\partial \gamma_i}{\partial z} \tag{A.28}$$

The above set of equations can be closed with continuity equations,

$$\frac{\partial n_e}{\partial t} + \frac{\partial}{\partial z} \left(n_e \frac{p_z^e}{\gamma_e} \right) = 0; \frac{\partial n_i}{\partial t} + \frac{\partial}{\partial z} \left(n_i \frac{p_z^i}{\gamma_i} \right) = 0 \tag{A.29}$$

Now the final closed set of equations to be solved are,

$$\frac{\partial E_z}{\partial z} = Zn_i - n_e \tag{A.30}$$

$$\frac{\partial E_z}{\partial t} = \left(n_e \frac{p_z^e}{\gamma_e} - Zn_i \frac{p_z^i}{\gamma_i m_i}\right) \tag{A.31}$$

$$\frac{\partial^2 \mathbf{a}}{\partial z^2} - \frac{\partial^2 \mathbf{a}}{\partial t^2} = \left(\frac{n_e}{\gamma_e} + \frac{Z^2 n_i}{\gamma_i m_i}\right)\mathbf{a} \tag{A.32}$$

$$\frac{\partial p_z^e}{\partial t} = -E_z - \frac{\partial \gamma_e}{\partial z} \tag{A.33}$$

$$\frac{\partial p_z^i}{\partial t} = ZE_z - m_i \frac{\partial \gamma_i}{\partial z} \tag{A.34}$$

$$\frac{\partial n_e}{\partial t} + \frac{\partial}{\partial z}\left(n_e \frac{p_z^e}{\gamma_e}\right) = 0 \tag{A.35}$$

$$\frac{\partial n_i}{\partial t} + \frac{\partial}{\partial z}\left(n_i \frac{p_z^i}{m_i \gamma_i}\right) = 0 \tag{A.36}$$

$$\gamma_e = \sqrt{1 + \mathbf{a}^2 + (p_z^e)^2}; \gamma_i = \sqrt{1 + \frac{Z^2}{m_i^2}\mathbf{a}^2 + \frac{\left(p_z^i\right)^2}{m_i}} \tag{A.37}$$

If we consider the steady ionic background, then the closed set of equations reduces to,

$$\frac{\partial E_z}{\partial z} = Zn_i - n_e \tag{A.38}$$

$$\frac{\partial E_z}{\partial t} = n_e \frac{p_z^e}{\gamma_e} \tag{A.39}$$

$$\frac{\partial^2 \mathbf{a}}{\partial z^2} - \frac{\partial^2 \mathbf{a}}{\partial t^2} = \frac{n_e}{\gamma_e}\mathbf{a} \tag{A.40}$$

$$\frac{\partial p_z^e}{\partial t} = -E_z - \frac{\partial \gamma_e}{\partial z} \tag{A.41}$$

$$\frac{\partial n_e}{\partial t} + \frac{\partial}{\partial z}\left(n_e \frac{p_z^e}{\gamma_e}\right) = 0 \tag{A.42}$$

$$\gamma_e = \sqrt{1 + \mathbf{a}^2 + (p_z^e)^2} \tag{A.43}$$

These are complete set of equations in closed form which need to be solved numerically with appropriate boundary conditions.

APPENDIX B

Numerical Methods

In appendix A the close set of equation for relativistic cold fluid model are stated with fixed ionic background. Here, we have discussed the finite difference method to numerically solve cold fluid model and wave propagation model stated in chapter 5. The 1D wave propagation equation in z-direction:

$$\frac{\partial^2 \mathbf{a}}{\partial z^2} - \frac{\partial^2 \mathbf{a}}{\partial t^2} = \frac{n_e}{\gamma_e}\mathbf{a} \tag{B.1}$$

To solve Eq. B.1, one can use a central difference scheme shown in Fig. B.1on domain (0, z_L) with boundary conditions as,

$$a(0,t) = 0; a(z_L, t) = 0. \tag{B.2}$$

and initial condition as,

$$a(z,0) = f(z); \partial a/\partial t = g(z). \tag{B.3}$$

Thereby, second order derivative can be written as;

$$\frac{a_i^{n+1} - 2a_i^n + a_i^{n-1}}{\Delta t^2} = \frac{a_{i+1}^n - 2a_i^n + a_{i-1}^n}{\Delta z^2} - \frac{n_{ei}^n}{\gamma_{ei}^n}a_i^n + \mathcal{O}(\Delta z^2, \Delta t^2). \tag{B.4}$$

by approximating derivatives in space and time, where, i = 0,1,... and n = 0,1,2.....

$$a_i^{n+1} = 2a_i^n - a_i^{n-1} + \frac{\Delta t^2}{\Delta z^2}\left(a_{i+1}^n - 2a_i^n + a_{i-1}^n\right) - \Delta t^2 \frac{n_{ei}^n}{\gamma_{ei}^n}a_i^n. \tag{B.5}$$

$$a_i^{n+1} = h^2 a_{i+1}^n + 2(1 - h^2 - w\Delta z^2)a_i^n + h^2 a_{i-1}^n - a_i^{n-1}. \tag{B.6}$$

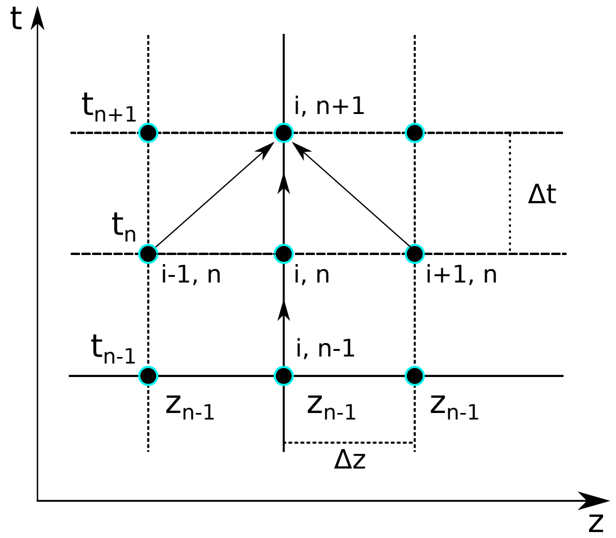

Figure B.1: *Central difference scheme for solving differential equations*

where, $w = n^n_{ei}/\gamma^n_{ei}$ and $h^2 = \Delta t^2/\Delta z^2$. Above Eq. B.5 have three nodes where data is transfered from step $n-1$ and n to $n+1$. Now solving the equation (B.5) where initial condition B.3 in central difference method is;

$$a' = \frac{a^1_i - a^{-1}_i}{2\Delta t} = g(z_i). \tag{B.7}$$

$$a^{-1}_i = a^1_i - 2\Delta t g(z_i). \tag{B.8}$$

Assuming, wave equation holds at t = 0 (n= 0), then Eq. B.6 can be written as,

$$a^1_i = h^2 a^0_{i+1} + 2(1 - h^2 - w\Delta z^2)a^0_i + h^2 a^0_{i-1} - a^{-1}_i \tag{B.9}$$

Substituting Eq. B.7 into Eq. B.9 one obtains,

$$a^1_i = \frac{1}{2}\left(h^2 a^0_{i+1} + 2(1 - h^2 - w\Delta z^2)a^0_i\right) + \Delta t g(z_i). \tag{B.10}$$

Similarly, all the coefficients can be obtained, since $a^0_i = f(z_i) = 0$ and $g(z_i) = 0$ for the Eq. B.1.

A complete set of equations A.38 - A.42 from appendix A and Eq. 5.1 - Eq. 5.5 from chapter 5 can be expressed as above solved wave equation.

APPENDIX C

Particle In Cell Simulations

C.1 Particle in cell (PIC) simulation method

Particle in cell (PIC) method came to use in early 1960s for computer simulation of plasmas. A compelling review by Dawson [207] thoroughly examines simulations of plasmas. This is straightforward method which solves equation of motion and Maxwell's equation (Coulomb's law, Poisson's equation). Instead of solving these equations in continuous space and time, the physical volume is discretized where each tiny space element is referred as a 'cell'. The intersection of lines are defined as set of points called mesh or grid points. In order to make simulation efficient macroparticles are considered which follows the same trajectory as the corresponding plasma particles. They represent fixed number or real particles and because the Lorentz force depends only on the charge-to-mass ratio, so a macroparticles will follow the same trajectory as a real particle.

Motion of macroparticles are governed in two steps. Firstly, by using Maxwell's equation or Poisson's equation (electromagnetic or electrostatic) fields are calculated from initial charge and current densities. Then the fields are used in Newton's equation of motion to move the particles on the mesh points. Now fields are recalculated from new particle positions and charge densities. The method also solves macro-quantities as density, current density etc, inside the cell and fields are calculated at the nodes. With basic computational cycle represented in Fig. C.1, the equations governing the calculations are as follows,

$$m_j \frac{d\mathbf{v_j}}{dt} = q_i \left(\mathbf{E} + \frac{\mathbf{v_j} \times \mathbf{B}}{c} \right) \tag{C.1}$$

for j = 1,2,3$\cdots$.

$$\frac{d\mathbf{x_j}}{dt} = \mathbf{v_j} \tag{C.2}$$

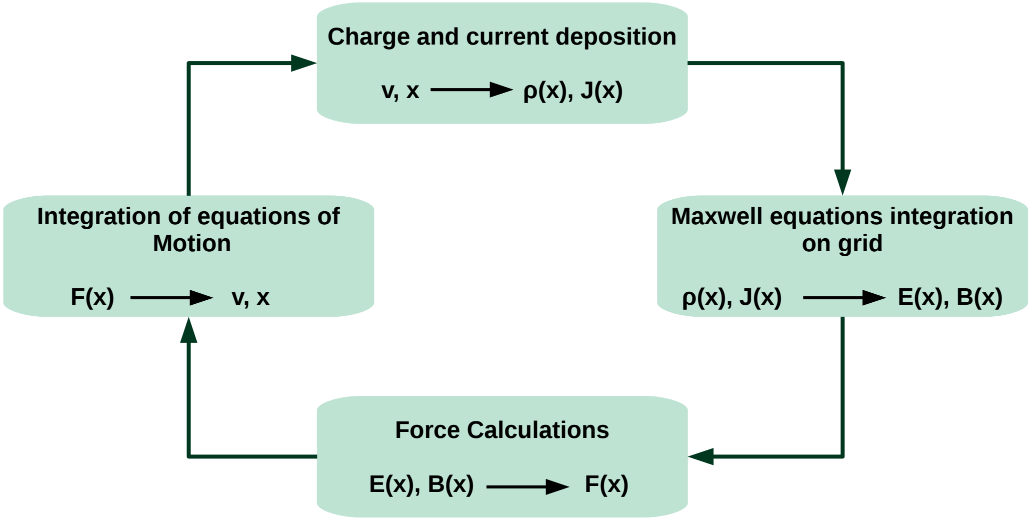
Charge and current deposition
v, x → ρ(x), J(x)
Maxwell equations integration on grid
ρ(x), J(x) → E(x), B(x)
Force Calculations
E(x), B(x) → F(x)
Integration of equations of Motion
F(x) → v, x

Figure C.1: *Particle-in-cell (PIC) simulation technique*

$$\nabla \times \mathbf{E} = -\frac{\partial \mathbf{B}}{\partial t} \tag{C.3}$$

$$\nabla \times \mathbf{B} = \mu_0 \mathbf{j} + \mu_0 \epsilon_0 \frac{\partial \mathbf{E}}{\partial t} \tag{C.4}$$

$$\nabla \cdot \mathbf{E} = \frac{\rho}{\epsilon_0} \tag{C.5}$$

$$\nabla \cdot \mathbf{B} = 0 \tag{C.6}$$

$$\rho(\mathbf{x}) = \sigma q_j \delta(\mathbf{x} - \mathbf{x_j}) \tag{C.7}$$

$$j(\mathbf{x}) = \sigma q_j \mathbf{v_j} \delta(\mathbf{x} - \mathbf{x_j}) \tag{C.8}$$

Here ρ and $\mathbf{j}$ are charge and current densities respectively. In each cell, time step Δt and thickness Δx are selected in such a way that it satisfies the CFL (Courant-Friedrichs-Lewy) condition, $c\Delta t < \Delta x$. In PIC, electromagnetic fields and current densities are calculated at cell boundaries, while charge density is calculated at the centre of the cell. Since simulation works in steps, so for small mass particle will have shorter Δt, whereas the heavier particle which can have a longer time step.

To calculate the particle push, i.e. advancing the particle in time, Boris scheme [208, 209] is found to be more viable. In this method the electric and magnetic fields are solved separately. The particle equation of motion using center-difference form is written as:

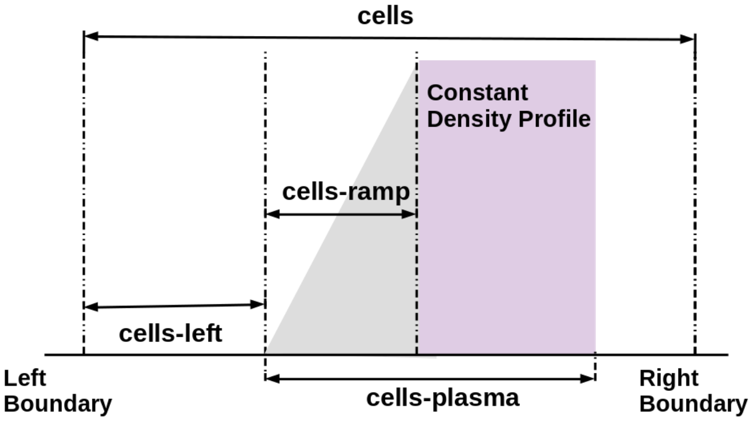

Figure C.2: *Simulation geometry of LPIC++, lables show the actual name of input parameter.*

$$m\frac{(\mathbf{v}_{t+\Delta/2}-\mathbf{v}_{t-\Delta/2})}{\Delta t}=q\left[\mathbf{E}_t+\frac{(\mathbf{v}_{\Delta+1/2}-\mathbf{v}_{\Delta-1/2})}{2}\times\mathbf{B}_t\right] \tag{C.9}$$

The magnetic term is centered at averaging of the particle velocity which is time-centered ($\mathbf{v}_{\Delta+1/2}$ and $\mathbf{v}_{\Delta-1/2}$). This results in the elimination of electric field. Since,

$$\mathbf{v}_{t-\Delta/2}=\mathbf{v}^- - \frac{q\mathbf{E}\Delta t}{2m} \tag{C.10}$$

$$\mathbf{v}_{t+\Delta/2}=\mathbf{v}^+ + \frac{q\mathbf{E}\Delta t}{2m} \tag{C.11}$$

$$\frac{\mathbf{v}^+-\mathbf{v}^-}{\Delta t}=\frac{q}{2m}(\mathbf{v}^++\mathbf{v}^-)\times\mathbf{B} \tag{C.12}$$

This scheme is time-reversible and semi-implicit.

C.2 LPIC++ - 1D Electromagnetic PIC Code

A parallel 1D, electromagnetic, relativistic PIC for simulating laser-plasma interactions developed by Richters, Pfund, and J. Meyer-Ter-Vehn for laser-plasma interaction studies [188]. The power of LPIC++ is mainly based on its clear program and data structure, which uses chained lists for the organization of grid cells and enables dynamic adjustment of spatial domain sizes in a very convenient way.

We have modified the program to include chirped function [88] to the Gaussian laser profile apart from standard field envelopes;

$$I = I_0 \exp\left(-\frac{4\ln(2)t^2}{\tau^2}\right)\cos[t + \zeta t^2] \tag{C.13}$$

$$I = I_0 \exp\left[-4\ln(2)\frac{t^2}{\tau^2}\right]\cos[t + g(t,\zeta)] \tag{C.14}$$

$$g(t,\zeta) = \zeta\left[4\ln(2)\frac{t^2}{\tau^2} + \frac{\tau^2}{16\ln(2)(1+\zeta^2)}\right] + \frac{\tan^{-1}(\zeta)}{2} \tag{C.15}$$

where, τ is FWHM pulse duration and ζ is the chirping parameter. The laser pulse can be incident from either side of the simulation domain. One can choose laser polarization between s-polarized, p-polarized and circularly polarized. The incident laser pulse can have mixture of frequencies and have provision for second and third harmonics. The incidence angle can be taken independently.

The appropriate simulation domain can be defined to have specific target size and density. The vacuum space can be left in front and rear side of the plasma. Plasma density is defined in the units of critical density. Along with it a linear ramp in plasma density can be introduced from the left side of the simulation domain. Simulation domain is discretized in number of cells. Further, number of cells per laser wavelength signifies the number of grid cells in x-direction per laser wavelength λ_0 in the laboratory frame.

The simulation box and plasma density profile for LPIC++ is shown in Fig. C.2. Number of microparticles per macroparticle is calculated automatically from the plasma density. Initial electron, ion temperatures and mass of ion species is also provided by input file.

LPIC++ is capable of calculating numerous physical parameters which can assist, to understand the field of laser-plasma interaction. As an example, time snapshots of electron densities, ion densities, electric and magnetic field components, current densities etc can be calculated. One can obtain velocity spectrum profile of electrons and ions along with the phase space diagrams. It can also calculate space time profile of various quantities like electron density, ion density, electric and magnetic field components etc. The velocity spectrum, electric and magnetic fields calculated by LPIC++ are space integrated, however one can obtain these parameters value at selected points as well in simulation domain with the use of traces. The particle energy can be obtained from the velocity spectrum itself which is explained below.

C.2.1 Kinetic energy of particles

The total energy of the particle moving with relativistic velocity is given as,

$$Total\ Energy(E)\ =\ Kinetic\ Energy\ (\mathcal{E})\ +\ Rest\ Mass\ Energy\ (m_o c^2)$$

$$\mathcal{E} = E - mc^2 \tag{C.16}$$

$$\mathcal{E} = \sqrt{p^2c^2 + m^2c^4} - mc^2 \tag{C.17}$$

$$p = mv = \frac{m\beta c}{\sqrt{1-\beta^2}} \equiv \gamma\ m\ \beta c \tag{C.18}$$

$$(\gamma = 1/\sqrt{1-\beta^2} \quad \text{and} \quad \beta = v/c)$$

$$\therefore\ \mathcal{E} = \sqrt{\gamma^2 m^2 \beta^2 c^4 + m^2c^4} - mc^2 \tag{C.19}$$

$$\mathcal{E} = \sqrt{m^2c^4(1+\gamma^2\beta^2)} - mc^2 \tag{C.20}$$

$$\mathcal{E} = (\sqrt{1+\gamma^2\beta^2} - 1)mc^2 \tag{C.21}$$

$$\mathcal{E} = (\gamma - 1)mc^2 \tag{C.22}$$

As an example, for an ion with $m_i/m_e = 1836$ the kinetic energy is comes out to be,

$$\mathcal{E} = 938.2\ (\gamma - 1) \quad MeV.$$

Bibliography

[1] A. Sharma. "High Energy electron and proton acceleration by circularly polarized laser pulse from near critical density hydrogen gas target". *Sci. Rep.*, **8**(1), 2191 (2018).

[2] T. Tajima and J. M. Dawson. "Laser Electron Accelerator". *Phys. Rev. Lett.*, **43**, 267–270 (1979).

[3] L. Karsch, E. Beyreuther, W. Enghardt, et al. "Towards ion beam therapy based on laser plasma accelerators". *Acta Oncologica*, **56**(11), 1359–1366 (2017).

[4] S. Bulanov, J. Wilkens, T. Esirkepov, et al. "Laser ion acceleration for hadron therapy". *Physics-Uspekhi*, **57**(12), 1149–1179 (2014).

[5] J. A. Cobble, R. P. Johnson, T. E. Cowan, et al. "High resolution laser-driven proton radiography". *J. Appl. Phys.*, **92**(4), 1775–1779 (2002).

[6] M. Barberio, M. Sciscció, S. Valliéres, et al. "Laser-accelerated particle beams for stress testing of materials". *Nat. Commun.*, **9**, 372 (2018).

[7] S. Bulanov and V. Khoroshkov. "Feasibility of using laser ion accelerators in proton therapy". *Plasma Phys. Rep.*, **28**(5), 453–456 (2002).

[8] G. A. Cirrone, M. Carpinelli, G. Cuttone, et al. "ELIMED, future hadrontherapy applications of laser-accelerated beams". *Nucl. Instrum. Methods Phys. Res.*, **730**, 174 – 177 (2013).

[9] K. Ledingham and W. Galster. "Laser-driven particle and photon beams and some applications". *New J. of Physics*, **12**, 045005 (2010).

[10] M. Roth, T. E. Cowan, M. H. Key, et al. "Fast Ignition by Intense Laser-Accelerated Proton Beams". *Phys. Rev. Lett.*, **86**, 436–439 (2001).

[11] M. Roth, D. Jung, K. Falk, et al. "Bright Laser-Driven Neutron Source Based on the Relativistic Transparency of Solids". *Phys. Rev. Lett.*, **110**, 044802 (2013).

[12] S. P. D. MANGLES, C. D. MURPHY, Z. NAJMUDIN, ET AL. "Monoenergetic beams of relativistic electrons from intense laser-plasma interactions". *Nature*, **431**, 535 (2004).

[13] J. FAURE, Y. GLINEC, A. PUKHOV, ET AL. "A laser-plasma accelerator producing monoenergetic electron beams". *Nature*, **431**, 541 (2004).

[14] C. G. R. GEDDES, C. TOTH, J. VAN TILBORG, ET AL. "High-quality electron beams from a laser wakefield accelerator using plasma-channel guiding". *Nature*, **431**, 538 (2004/09/30/online).

[15] R. A. SNAVELY, M. H. KEY, S. P. HATCHETT, ET AL. "Intense High-Energy Proton Beams from Petawatt-Laser Irradiation of Solids". *Phys. Rev. Lett.*, **85**, 2945–2948 (2000).

[16] S. C. WILKS, A. B. LANGDON, T. E. COWAN, ET AL. "Energetic proton generation in ultra-intense laser–solid interactions". *Phys. Plasmas,*, **8**(2), 542–549 (2001).

[17] H. SCHWOERER, S. PFOTENHAUER, O. JACKEL, ET AL. "Laser-plasma acceleration of quasi-monoenergetic protons from microstructured targets". *Nature*, **439**(7075), 113108 (2006).

[18] A. SGATTONI, P. LONDRILLO, A. MACCHI, ET AL. "Laser ion acceleration using a solid target coupled with a low-density layer". *Phys. Rev. E*, **85**, 036405 (2012).

[19] I. J. KIM, K. H. PAE, I. W. CHOI, ET AL. "Radiation pressure acceleration of protons to $93MeV$ with circularly polarized petawatt laser pulses". *Phys. Plasmas*, **23**(7), 070701 (2016).

[20] L. YIN, B. J. ALBRIGHT, B. M. HEGELICH, ET AL. "Monoenergetic and GeV ion acceleration from the laser breakout afterburner using ultrathin targetsa)". *Phys. Plasmas,*, **14**(5), 056706 (2007).

[21] L. YIN, B. J. ALBRIGHT, D. JUNG, ET AL. "Break-out afterburner ion acceleration in the longer laser pulse length regime". *Phys. Plasmas*, **18**(6), 063103 (2011).

[22] B. QIAO, M. ZEPF, P. GIBBON, ET AL. "Conditions for efficient and stable ion acceleration by moderate circularly polarized laser pulses at intensities of 1020 W/cm2". *Phys. Plasmas,*, **18**(4), 043102 (2011).

[23] A. ROBINSON, P. GIBBON, M. M ZEPF, ET AL. "Relativistically correct hole-boring and ion acceleration by circularly polarized laser pulses". *Plasma Phys. Control. Fusion*, **51**, 024004 (2009).

[24] F. FIUZA, A. STOCKEM, E. BOELLA, ET AL. "Laser-Driven Shock Acceleration of Monoenergetic Ion Beams". *Phys. Rev. Lett.*, **109**, 215001 (2012).

[25] S. KAR, K. F. KAKOLEE, B. QIAO, ET AL. "Ion Acceleration in Multispecies Targets Driven by Intense Laser Radiation Pressure". *Phys. Rev. Lett.*, **109**, 185006 (2012).

[26] C. A. J. PALMER, N. P. DOVER, I. POGORELSKY, ET AL. "Monoenergetic Proton Beams Accelerated by a Radiation Pressure Driven Shock". *Phys. Rev. Lett.*, **106**, 014801 (2011).

[27] A. P. L. ROBINSON, R. M. G. M. TRINES, N. P. DOVER, ET AL. "Hole-boring radiation pressure acceleration as a basis for producing high-energy proton bunches". *Plasma Phys. Control. Fusion*, **54**(11), 115001 (2012).

[28] A. MACCHI, S. VEGHINI, AND F. PEGORARO. ""Light Sail" Acceleration Reexamined". *Phys. Rev. Lett.*, **103**, 085003 (2009).

[29] A. MACCHI, S. VEGHINI, T. V. LISEYKINA, ET AL. "Radiation pressure acceleration of ultrathin foils". *New J. Phys.*, **12**(4), 045013 (2010).

[30] E. SIMINOS, M. GRECH, S. SKUPIN, ET AL. "Effect of electron heating on self-induced transparency in relativistic-intensity laser-plasma interactions". *Phys. Rev. E*, **86**, 056404 (2012).

[31] V. I. EREMIN, A. V. KORZHIMANOV, AND A. V. KIM. "Relativistic self-induced transparency effect during ultraintense laser interaction with overdense plasmas: Why it occurs and its use for ultrashort electron bunch generation". *Phys. Plasmas*, **17**(4), 043102 (2010).

[32] V. V. GOLOVIZNIN AND T. J. SCHEP. "Self-induced transparency and self-induced opacity in laser-plasma interactions". *Phys. Plasmas*, **7**(5), 1564–1571 (2000).

[33] J. C. FERNÁNDEZ, D. C. GAUTIER, C. HUANG, ET AL. "Laser-plasmas in the relativistic-transparency regime: Science and applications". *Phys. Plasmas*, **24**(5), 056702 (2017).

[34] L. E. HARGROVE, R. L. FORK, AND M. A. POLLACK. "LOCKING OF He–Ne LASER MODES INDUCED BY SYNCHRONOUS INTRACAVITY MODULATION". *Appl. Phys. Lett.*, **5**(1), 4–5 (1964).

[35] H. W. MOCKER AND R. J. COLLINS. "MODE COMPETITION AND SELF-LOCKING EFFECTS IN A Q-SWITCHED RUBY LASER". *Appl. Phys. Lett.*, **7**(10), 270–273 (1965).

[36] R. W. HELLWARTH. *Advances in Quantum Electronics edited by J. R. Singer* (Columbia University Press, New York, 1961).

[37] J. ZHOU, G. TAFT, C.-P. HUANG, ET AL. "Pulse evolution in a broad-bandwidth Ti:sapphire laser". *Opt. Lett.*, **19**(15), 1149–1151 (1994).

[38] D. STRICKLAND AND G. MOUROU. "Compression of amplified chirped optical pulses". *Opt. Commun.*, **56**, 219–221 (1985).

[39] A. ASHKIN. "Acceleration and Trapping of Particles by Radiation Pressure". *Phys. Rev. Lett.*, **24**, 156–159 (1970).

[40] A. DUBIETIS, G. JONUŠAUSKAS, AND A. PISKARSKAS. "Powerful femtosecond pulse generation by chirped and stretched pulse parametric amplification in BBO crystal". *Opt. Commun.*, **88**(4), 437 – 440 (1992).

[41] N. ISHII, L. TURI, V. S. YAKOVLEV, ET AL. "Multimillijoule chirped parametric amplification of few-cycle pulses". *Opt. Lett.*, **30**(5), 567–569 (2005).

[42] S. WITTE, R. ZINKSTOK, W. HOGERVORST, ET AL. "Numerical simulations for performance optimization of a few-cycle terawatt NOPCPA system". *Appl. Phys. B*, **87**, 677 (2007).

[43] I. ROSS, P. MATOUSEK, M. TOWRIE, ET AL. "The prospects for ultrashort pulse duration and ultrahigh intensity using optical parametric chirped pulse amplifiers". *Opt. Commun.*, **144**(1), 125 – 133 (1997).

[44] I. N. ROSS, J. L. COLLIER, P. MATOUSEK, ET AL. "Generation of terawatt pulses by use of optical parametric chirped pulse amplification". *Appl. Opt.*, **39**(15), 2422–2427 (2000).

[45] S. WITTE AND K. S. E. EIKEMA. "Ultrafast Optical Parametric Chirped-Pulse Amplification". *IEEE J. Sel. Top. Quantum Electron.*, **18**(1), 296–307 (2012).

[46] E. GRACE, C. TSANGARIS, AND G. NEW. "Competing processes in optical parametric chirped pulse amplification". *Opt. Commun.*, **261**(2), 225 – 230 (2006).

[47] J. MOSES, C. MANZONI, S.-W. HUANG, ET AL. "Temporal optimization of ultrabroadband high-energy OPCPA". *Opt. Express*, **17**(7), 5540–5555 (2009).

[48] Q. ZHANG, E. J. TAKAHASHI, O. D. MÜCKE, ET AL. "Dual-chirped optical parametric amplification for generating few hundred mJ infrared pulses". *Opt. Express*, **19**(8), 7190–7212 (2011).

[49] F. F. CHEN. *Introduction to Plasma Physics and Controlled Fusion, Volume 1: Plasma Physics* (Plenum Press, 1984).

[50] W. L. KRUER AND K. ESTABROOK. "J × B heating by very intense laser light". *Phys. Fluids*, **28**(1), 430–432 (1985).

[51] B. HEGELICH, D. JUNG, B. ALBRIGHT, ET AL. "Experimental demonstration of particle energy, conversion efficiency and spectral shape required for ion-based fast ignition". *Nucl. Fusion*, **51**(8), 083011 (2011).

[52] R. R. WILSON. "Radiological Use of Fast Protons". *Radiology*, **47**(5), 487–491 (1946). PMID: 20274616.

[53] R. N. KJELLBERG, T. HANAMURA, K. R. DAVIS, ET AL. "Bragg-Peak Proton-Beam Therapy for Arteriovenous Malformations of the Brain". *N. Engl. J. Med.*, **309**(5), 269–274 (1983). PMID: 6306463.

[54] K. ZEIL, M. BAUMANN, E. BEYREUTHER, ET AL. "Dose-controlled irradiation of cancer cells with laser-accelerated proton pulses". *Appl. Phys. B*, **110**, 437 (2013).

[55] P. BOLTON, T. HORI, H. KIRIYAMA, ET AL. "Toward integrated laser-driven ion accelerator systems at the photo-medical research center in Japan". *Nucl. Instrum. Methods Phys. Res.*, **620**(1), 71 – 75 (2010). COULOMB09.

[56] *Ion source development and radiobiology applications within the LIBRA project*, vol. 8079.

[57] A. M. KOEHLER. "Proton Radiography". *Science*, **160**(3825), 303–304 (1968).

[58] N. KING, E. ABLES, K. ADAMS, ET AL. "An 800-MeV proton radiography facility for dynamic experiments". *Nucl. Instrum. Methods Phys. Res.*, **424**(1), 84 – 91 (1999).

[59] M. BORGHESI, A. J. MACKINNON, D. H. CAMPBELL, ET AL. "Multi-MeV Proton Source Investigations in Ultraintense Laser-Foil Interactions". *Phys. Rev. Lett.*, **92**, 055003 (2004).

[60] C. K. LI, F. H. SÉGUIN, J. A. FRENJE, ET AL. "Measuring E and B Fields in Laser-Produced Plasmas with Monoenergetic Proton Radiography". *Phys. Rev. Lett.*, **97**, 135003 (2006).

[61] L. ROMAGNANI, J. FUCHS, M. BORGHESI, ET AL. "Dynamics of Electric Fields Driving the Laser Acceleration of Multi-MeV Protons". *Phys. Rev. Lett.*, **95**, 195001 (2005).

[62] S. KAR, M. BORGHESI, C. A. CECCHETTI, ET AL. "Dynamics of charge-displacement channeling in intense laser–plasma interactions". *New J. Phys.*, **9**(11), 402 (2007).

[63] L. WILLINGALE, P. M. NILSON, A. G. R. THOMAS, ET AL. "High-Power, Kilojoule Class Laser Channeling in Millimeter-Scale Underdense Plasma". *Phys. Rev. Lett.*, **106**, 105002 (2011).

[64] L. ROMAGNANI, S. V. BULANOV, M. BORGHESI, ET AL. "Observation of Collisionless Shocks in Laser-Plasma Experiments". *Phys. Rev. Lett.*, **101**, 025004 (2008).

[65] K. W. D. LEDINGHAM, P. MCKENNA, T. MCCANNY, ET AL. "High power laser production of short-lived isotopes for positron emission tomography". *J. Phys. D*, **37**(16), 2341 (2004).

[66] Y. KIYANAGI. "Neutron Imaging at Compact Accelerator-Driven Neutron Sources in Japan". *J. Imaging*, **4**(4) (2018).

[67] L. WILLINGALE, A. G. R. THOMAS, P. M. NILSON, ET AL. "Proton probe measurement of fast advection of magnetic fields by hot electrons". *Plasma Phys. Control. Fusion*, **53**(12), 124026 (2011).

[68] J. NUCKOLLS, L. WOOD, A. THIESSEN, ET AL. "Laser Compression of Matter to Super-High Densities: Thermonuclear (CTR) Applications". *Nature*, **239**, 139 (1972).

[69] J. LINDL. "Development of the indirect-drive approach to inertial confinement fusion and the target physics basis for ignition and gain". *Phys. Plasmas*, **2**(11), 3933–4024 (1995).

[70] M. TABAK, J. HAMMER, M. E. GLINSKY, ET AL. "Ignition and high gain with ultrapowerful lasers*". *Phys. Plasmas*, **1**(5), 1626–1634 (1994).

[71] M. TEMPORAL. "Fast ignition of a compressed inertial confinement fusion hemispherical capsule by two proton beams". *Phys. Plasmas*, **13**(12), 122704 (2006).

[72] M. TEMPORAL, J. J. HONRUBIA, AND S. ATZENI. "Proton-beam driven fast ignition of inertially confined fuels: Reduction of the ignition energy by the use of two proton beams with radially shaped profiles". *Phys. Plasmas*, **15**(5), 052702 (2008).

[73] V. Y. BYCHENKOV, W. ROZMUS, A. MAKSIMCHUK, ET AL. "Fast ignitor concept with light ions". *Plasma Phys. Rep.*, **27**, 1017–1020 (2001).

[74] X. ZHANG, B. SHEN, L. JI, ET AL. "Ion acceleration with mixed solid targets interacting with circularly polarized lasers". *Phys. Rev. ST Accel. Beams*, **12**, 021301 (2009).

[75] T.-P. YU, A. PUKHOV, G. SHVETS, ET AL. "Stable Laser-Driven Proton Beam Acceleration from a Two-Ion-Species Ultrathin Foil". *Phys. Rev. Lett.*, **105**, 065002 (2010).

[76] M. GRECH, S. SKUPIN, R. NUTER, ET AL. "High-quality ion beams by irradiating a nano-structured target with a petawatt laser pulse". *New J. Phys.*, **11**(9), 093035 (2009).

[77] T. SCHLEGEL, N. NAUMOVA, V. T. TIKHONCHUK, ET AL. "Relativistic laser piston model: Ponderomotive ion acceleration in dense plasmas using ultraintense laser pulses". *Phys. Plasmas*, **16**(8), 083103 (2009).

[78] C. K. HUANG, B. J. ALBRIGHT, L. YIN, ET AL. "A double-foil target for improving beam quality in laser ion acceleration with thin foilsa)". *Phys. Plasmas*, **18**(5), 056707 (2011).

[79] P. KAW AND J. DAWSON. "Relativistic Nonlinear Propagation of Laser Beams in Cold Overdense Plasmas". *Phys. Fluids*, **13**(2), 472–481 (1970).

[80] C. MAX AND F. PERKINS. "Strong Electromagnetic Waves in Overdense Plasmas". *Phys. Rev. Lett.*, **27**, 1342–1345 (1971).

[81] L. WILLINGALE, S. R. NAGEL, A. G. R. THOMAS, ET AL. "Characterization of High-Intensity Laser Propagation in the Relativistic Transparent Regime through Measurements of Energetic Proton Beams". *Phys. Rev. Lett.*, **102**, 125002 (2009).

[82] A. HENIG, D. KIEFER, K. MARKEY, ET AL. "Enhanced Laser-Driven Ion Acceleration in the Relativistic Transparency Regime". *Phys. Rev. Lett.*, **103**, 045002 (2009).

[83] X. JIAO, J. SHAW, T. WANG, ET AL. "A tabletop, ultrashort pulse photoneutron source driven by electrons from laser wakefield acceleration". *Matter Radiat. Extremes*, **2**(6), 296 – 302 (2017).

[84] A. HIGGINSON, R. J. GRAY, M. KING, ET AL. "Near-100 MeV protons via a laser-driven transparency-enhanced hybrid acceleration scheme". *Nat. Commun.*, **9**, 724 (2018).

[85] S. CHOUDHARY AND A. R. HOLKUNDKAR. "Efficient ion acceleration by relativistic self-induced transparency in subwavelength targets". *Eur. Phys. J. D*, **70**(11), 234 (2016).

[86] M. CHEN, Z.-M. SHENG, Q.-L. DONG, ET AL. "Collisionless electrostatic shock generation and ion acceleration by ultraintense laser pulses in overdense plasmas". *Phys. Plasmas*, **14**(5), 053102 (2007).

[87] S. S. BULANOV, A. BRANTOV, V. Y. BYCHENKOV, ET AL. "Accelerating monoenergetic protons from ultrathin foils by flat-top laser pulses in the directed-Coulomb-explosion regime". *Phys. Rev. E*, **78**, 026412 (2008).

[88] F. MACKENROTH, A. GONOSKOV, AND M. MARKLUND. "Chirped-Standing-Wave Acceleration of Ions with Intense Lasers". *Phys. Rev. Lett.*, **117**, 104801 (2016).

[89] S. CHOUDHARY AND A. R. HOLKUNDKAR. "Chirp assisted ion acceleration via relativistic self-induced transparency". *Phys. Plasmas*, **25**(10), 103111 (2018).

[90] B. GONZALEZ-IZQUIERDO, M. KING, R. J. GRAY, ET AL. "Towards optical polarization control of laser-driven proton acceleration in foils undergoing relativistic transparency". *Nat. Commun.*, **7**, 12891 (2016).

[91] C. SCULLION, D. DORIA, L. ROMAGNANI, ET AL. "Polarization Dependence of Bulk Ion Acceleration from Ultrathin Foils Irradiated by High-Intensity Ultrashort Laser Pulses". *Phys. Rev. Lett.*, **119**, 054801 (2017).

[92] H. VOSOUGHIAN, G. SARRI, M. BORGHESI, ET AL. "The effect of positively chirped laser pulse on energy enhancement of proton acceleration in combinational radiation pressure and bubble regime". *Phys. Plasmas*, **24**(10), 103123 (2017).

[93] M. KALUZA, J. SCHREIBER, M. I. K. SANTALA, ET AL. "Influence of the Laser Prepulse on Proton Acceleration in Thin-Foil Experiments". *Phys. Rev. Lett.*, **93**, 045003 (2004).

[94] J. DAVIS, G. M. PETROV, AND A. L. VELIKOVICH. "Dynamics of intense laser channel formation in an underdense plasma". *Phys. Plasmas*, **12**(12), 123102 (2005).

[95] A. SULLIVAN, H. HAMSTER, S. P. GORDON, ET AL. "Propagation of intense, ultrashort laser pulses in plasmas". *Opt. Lett.*, **19**(19), 1544–1546 (1994).

[96] Z. NAJMUDIN, M. TATARAKIS, K. KRUSHELNICK, ET AL. "Ultra-high-intensity laser propagation through underdense plasma". *IEEE Trans. Plasma Sci.*, **30**(1), 44–45 (2002).

[97] P. SPRANGLE AND B. HAFIZI. "High-power, high-intensity laser propagation and interactions". *Phys. Plasmas*, **21**(5), 055402 (2014).

[98] X. L. CHEN AND R. N. SUDAN. "Two-dimensional self-focusing of short intense laser pulse in underdense plasma". *Phys. Fluids B*, **5**(4), 1336–1348 (1993).

[99] D. K. SINGH, J. R. DAVIES, G. SARRI, ET AL. "Dynamics of intense laser propagation in underdense plasma: Polarization dependence". *Phys. Plasmas*, **19**(7), 073111 (2012).

[100] T. C. WILSON, F. Y. LI, M. WEIKUM, ET AL. "Influence of strong magnetic fields on laser pulse propagation in underdense plasma". *Plasma Phys. Control. Fusion*, **59**(6), 065002 (2017).

[101] A. G. SMYTH, G. SARRI, M. VRANIC, ET AL. "Magnetic field generation during intense laser channelling in underdense plasma". *Phys. Plasmas*, **23**(6), 063121 (2016).

[102] L. HADŽIEVSKI, M. S. JOVANOVIĆ, M. M. ŠKORIĆ, ET AL. "Stability of one-dimensional electromagnetic solitons in relativistic laser plasmas". *Phys. Plasmas*, **9**(6), 2569–2574 (2002).

[103] G. Sánchez-Arriaga, E. Siminos, and E. Lefebvre. "Relativistic solitary waves modulating long laser pulses in plasmas". *Plasma Phys. Control. Fusion*, **53**(4), 045011 (2011).

[104] A. Pukhov, N. Kumar, T. Tückmantel, et al. "Phase Velocity and Particle Injection in a Self-Modulated Proton-Driven Plasma Wakefield Accelerator". *Phys. Rev. Lett.*, **107**, 145003 (2011).

[105] A. R. Holkundkar and G. Brodin. "Transition from wakefield generation to soliton formation". *Phys. Rev. E*, **97**, 043204 (2018).

[106] P. Sprangle, E. Esarey, and A. Ting. "Nonlinear theory of intense laser-plasma interactions". *Phys. Rev. Lett.*, **64**, 2011–2014 (1990).

[107] P. Sprangle, E. Esarey, and A. Ting. "Nonlinear interaction of intense laser pulses in plasmas". *Phys. Rev. A*, **41**, 4463–4469 (1990).

[108] C. D. Decker and W. B. Mori. "Group velocity of large amplitude electromagnetic waves in a plasma". *Phys. Rev. Lett.*, **72**, 490–493 (1994).

[109] L. Yin, B. J. Albright, B. M. Hegelich, et al. "GeV laser ion acceleration from ultrathin targets: The laser break-out afterburner". *Laser Part. Beams*, **24**, 291–298 (2006).

[110] W. P. Leemans, B. Nagler, A. J. Gonsalves, et al. "GeV electron beams from a centimetre-scale accelerator". *Nat. Phys.*, **2**, 696 (2006/09/24/online).

[111] J. Faure, C. Rechatin, A. Norlin, et al. "Controlled injection and acceleration of electrons in plasma wakefields by colliding laser pulses". *Nature*, **444**, 737 (2006).

[112] P. Chen, J. M. Dawson, R. W. Huff, et al. "Acceleration of Electrons by the Interaction of a Bunched Electron Beam with a Plasma". *Phys. Rev. Lett.*, **54**, 693–696 (1985).

[113] P. Sprangle, E. Esarey, J. Krall, et al. "Propagation and guiding of intense laser pulses in plasmas". *Phys. Rev. Lett.*, **69**, 2200–2203 (1992).

[114] T. M. Antonsen and P. Mora. "Self-focusing and Raman scattering of laser pulses in tenuous plasmas". *Phys. Rev. Lett.*, **69**, 2204–2207 (1992).

[115] P. Sprangle, E. Esarey, and A. Ting. "Excitation of ultrarelativistic plasma waves by pulse of electromagnetic radiation". *J. Exp. Theor. Phys.*, **50**, 198 (1989).

[116] M. Zeng, M. Chen, L. L. Yu, et al. "Multichromatic Narrow-Energy-Spread Electron Bunches from Laser-Wakefield Acceleration with Dual-Color Lasers". *Phys. Rev. Lett.*, **114**, 084801 (2015).

[117] S. Bulanov, N. Naumova, F. Pegoraro, et al. "Particle injection into the wave acceleration phase due to nonlinear wake wave breaking". *Phys. Rev. E*, **58**, R5257–R5260 (1998).

[118] P. Volfbeyn, P. B. Lee, J. Wurtele, et al. "Driving laser pulse evolution in a hollow channel laser wakefield accelerator". *Phys. Plasmas*, **4**(9), 3403–3410 (1997).

[119] X. F. Li, Q. Yu, Y. J. Gu, et al. "Bubble shape and electromagnetic field in the nonlinear regime for laser wakefield acceleration". *Phys. Plasmas*, **22**(8), 083112 (2015).

[120] A. G. R. Thomas, S. P. D. Mangles, Z. Najmudin, et al. "Measurements of Wave-Breaking Radiation from a Laser-Wakefield Accelerator". *Phys. Rev. Lett.*, **98**, 054802 (2007).

[121] B. Liu, J. Meyer-ter Vehn, K.-U. Bamberg, et al. "Ion wave breaking acceleration". *Phys. Rev. Accel. Beams*, **19**, 073401 (2016).

[122] A. Modena, Z. Najmudin, A. E. Dangor, et al. "Electron acceleration from the breaking of relativistic plasma waves". *Nature*, **377**, 606 (1995).

[123] C. I. Moore, A. Ting, K. Krushelnick, et al. "Electron Trapping in Self-Modulated Laser Wakefields by Raman Backscatter". *Phys. Rev. Lett.*, **79**, 3909–3912 (1997).

[124] C. E. Clayton, K. A. Marsh, A. Dyson, et al. "Ultrahigh-gradient acceleration of injected electrons by laser-excited relativistic electron plasma waves". *Phys. Rev. Lett.*, **70**, 37–40 (1993).

[125] D. Umstadter, J. K. Kim, and E. Dodd. "Laser Injection of Ultrashort Electron Pulses into Wakefield Plasma Waves". *Phys. Rev. Lett.*, **76**, 2073–2076 (1996).

[126] C. G. R. Geddes, K. Nakamura, G. R. Plateau, et al. "Plasma-Density-Gradient Injection of Low Absolute-Momentum-Spread Electron Bunches". *Phys. Rev. Lett.*, **100**, 215004 (2008).

[127] E. Oz, S. Deng, T. Katsouleas, et al. "Ionization-Induced Electron Trapping in Ultrarelativistic Plasma Wakes". *Phys. Rev. Lett.*, **98**, 084801 (2007).

[128] S. P. Le Blanc, M. C. Downer, R. Wagner, et al. "Temporal characterization of a self-modulated laser wakefield". *AIP Conference Proceedings*, **398**(1), 651–663 (1997).

[129] G. Malka, E. Lefebvre, and J. L. Miquel. "Experimental Observation of Electrons Accelerated in Vacuum to Relativistic Energies by a High-Intensity Laser". *Phys. Rev. Lett.*, **78**, 3314–3317 (1997).

[130] E. L. Clark, K. Krushelnick, J. R. Davies, et al. "Measurements of Energetic Proton Transport through Magnetized Plasma from Intense Laser Interactions with Solids". *Phys. Rev. Lett.*, **84**, 670–673 (2000).

[131] A. Maksimchuk, S. Gu, K. Flippo, et al. "Forward Ion Acceleration in Thin Films Driven by a High-Intensity Laser". *Phys. Rev. Lett.*, **84**, 4108–4111 (2000).

[132] A. P. L. Robinson, A. R. Bell, and R. J. Kingham. "Effect of Target Composition on Proton Energy Spectra in Ultraintense Laser-Solid Interactions". *Phys. Rev. Lett.*, **96**, 035005 (2006).

[133] B. J. Albright, L. Yin, B. M. Hegelich, et al. "Theory of Laser Acceleration of Light Ion Beams from Interaction of Ultrahigh Intensity Lasers with Layered Targets". *Phys. Rev. Lett.*, **97**, 115002 (2006).

[134] P. Mora. "Plasma Expansion into a Vacuum". *Phys. Rev. Lett.*, **90**, 185002 (2003).

[135] J. Fuchs, P. Antici, E. d'Humières, et al. "Laser-driven proton scaling laws and new paths towards energy increase". *Nat. Phys.*, **2**, 48 (2005). Article.

[136] F. N. Beg, A. R. Bell, A. E. Dangor, et al. "A study of picosecond laser–solid interactions up to $10^19W/cm^2$". *Phys. Plasmas*, **4**(2), 447–457 (1997).

[137] P. Gibbon and E. Förster. "Short-pulse laser - plasma interactions". *Plasma Phys. Control. Fusion*, **38**(6), 769 (1996).

[138] T. Kluge, T. Cowan, A. Debus, et al. "Electron Temperature Scaling in Laser Interaction with Solids". *Phys. Rev. Lett.*, **107**, 205003 (2011).

[139] A. J. Mackinnon, Y. Sentoku, P. K. Patel, et al. "Enhancement of Proton Acceleration by Hot-Electron Recirculation in Thin Foils Irradiated by Ultraintense Laser Pulses". *Phys. Rev. Lett.*, **88**, 215006 (2002).

[140] J. S. Green, N. Booth, R. J. Dance, et al. "Time-resolved measurements of fast electron recirculation for relativistically intense femtosecond scale laser-plasma interactions". *Sci. Rep.*, **8**(1), 4525 (2018).

[141] J. Schreiber, F. Bell, F. Grüner, et al. "Analytical Model for Ion Acceleration by High-Intensity Laser Pulses". *Phys. Rev. Lett.*, **97**, 045005 (2006).

[142] M. Zepf, E. L. Clark, K. Krushelnick, et al. "Fast particle generation and energy transport in laser-solid interactions". *Phys. Plasmas*, **8**(5), 2323–2330 (2001).

[143] M. BORGHESI, J. FUCHS, S. V. BULANOV, ET AL. "Fast Ion Generation by High-Intensity Laser Irradiation of Solid Targets and Applications". *Fusion Sci. Technol.*, **49**(3), 412–439 (2006).

[144] A. ZIGLER, S. EISENMAN, M. BOTTON, ET AL. "Enhanced Proton Acceleration by an Ultrashort Laser Interaction with Structured Dynamic Plasma Targets". *Phys. Rev. Lett.*, **110**, 215004 (2013).

[145] Y. SENTOKU, T. E. COWAN, A. KEMP, ET AL. "High energy proton acceleration in interaction of short laser pulse with dense plasma target". *Phys. Plasmas*, **10**(5), 2009–2015 (2003).

[146] M. PASSONI, L. BERTAGNA, AND A. ZANI. "Target normal sheath acceleration: theory, comparison with experiments and future perspectives". *New J. Phys.*, **12**(4), 045012 (2010).

[147] A. J. MACKINNON, M. BORGHESI, S. HATCHETT, ET AL. "Effect of Plasma Scale Length on Multi-MeV Proton Production by Intense Laser Pulses". *Phys. Rev. Lett.*, **86**, 1769–1772 (2001).

[148] S. P. HATCHETT, C. G. BROWN, T. E. COWAN, ET AL. "Electron, photon, and ion beams from the relativistic interaction of Petawatt laser pulses with solid targets". *Phys. Plasmas*, **7**(5), 2076–2082 (2000).

[149] T. E. COWAN, J. FUCHS, H. RUHL, ET AL. "Ultralow Emittance, Multi-MeV Proton Beams from a Laser Virtual-Cathode Plasma Accelerator". *Phys. Rev. Lett.*, **92**, 204801 (2004).

[150] K. NEMOTO, A. MAKSIMCHUK, S. BANERJEE, ET AL. "Laser-triggered ion acceleration and table top isotope production". *Appl. Phys. Lett.*, **78**(5), 595–597 (2001).

[151] M. ALLEN, P. K. PATEL, A. MACKINNON, ET AL. "Direct Experimental Evidence of Back-Surface Ion Acceleration from Laser-Irradiated Gold Foils". *Phys. Rev. Lett.*, **93**, 265004 (2004).

[152] J. FUCHS, Y. SENTOKU, S. KARSCH, ET AL. "Comparison of Laser Ion Acceleration from the Front and Rear Surfaces of Thin Foils". *Phys. Rev. Lett.*, **94**, 045004 (2005).

[153] J. FUCHS, Y. SENTOKU, E. D'HUMIÈRES, ET AL. "Comparative spectra and efficiencies of ions laser-accelerated forward from the front and rear surfaces of thin solid foils". *Phys. Plasmas*, **14**(5), 053105 (2007).

[154] M. HEGELICH, S. KARSCH, G. PRETZLER, ET AL. "MeV Ion Jets from Short-Pulse-Laser Interaction with Thin Foils". *Phys. Rev. Lett.*, **89**, 085002 (2002).

[155] B. M. Hegelich, B. Albright, P. Audebert, et al. “Spectral properties of laser-accelerated mid-Z MeV/u ion beams”. *Phys. Plasmas*, **12**(5), 056314 (2005).

[156] B. M. Hegelich, B. J. Albright, J. Cobble, et al. “Laser acceleration of quasi-monoenergetic MeV ion beams”. *Nature*, **439**, 441.

[157] M. ROTH, E. BRAMBRINK, P. AUDEBERT, et al. “Laser accelerated ions and electron transport in ultra-intense laser matter interaction”. *Laser and Particle Beams*, **23**(1), 95–100 (2005).

[158] T. Kiefer, T. Schlegel, and M. C. Kaluza. “Plasma expansion into vacuum assuming a steplike electron energy distribution”. *Phys. Rev. E*, **87**, 043110 (2013).

[159] H. Daido, M. Nishiuchi, and A. S. Pirozhkov. “Review of laser-driven ion sources and their applications”. *Rep. Prog. Phys.*, **75**(5), 056401 (2012).

[160] T. Esirkepov, M. Borghesi, S. V. Bulanov, et al. “Highly Efficient Relativistic-Ion Generation in the Laser-Piston Regime”. *Phys. Rev. Lett.*, **92**, 175003 (2004).

[161] S. C. Wilks, W. L. Kruer, M. Tabak, et al. “Absorption of ultra-intense laser pulses”. *Phys. Rev. Lett.*, **69**, 1383–1386 (1992).

[162] A. Macchi, F. Cattani, T. V. Liseykina, et al. “Laser Acceleration of Ion Bunches at the Front Surface of Overdense Plasmas”. *Phys. Rev. Lett.*, **94**, 165003 (2005).

[163] A. Pukhov and J. Meyer-ter Vehn. “Laser Hole Boring into Overdense Plasma and Relativistic Electron Currents for Fast Ignition of ICF Targets”. *Phys. Rev. Lett.*, **79**, 2686–2689 (1997).

[164] J. Badziak, S. Głowacz, S. Jabłoński, et al. “Production of ultrahigh-current-density ion beams by short-pulse skin-layer laser–plasma interaction”. *Appl. Phys. Lett.*, **85**(15), 3041–3043 (2004).

[165] I. V. Pogorelsky, M. Babzien, I. Ben-Zvi, et al. “BESTIA – The next generation ultra-fast CO2 laser for advanced accelerator research”. *Nucl. Instrum. Methods Phys. Res.*, **829**, 432 – 437 (2016). 2nd European Advanced Accelerator Concepts Workshop - EAAC 2015.

[166] F. Sylla, M. Veltcheva, S. Kahaly, et al. “Development and characterization of very dense submillimetric gas jets for laser-plasma interaction”. *Rev. Sci. Instrum.*, **83**(3), 033507 (2012).

[167] A. Zani, D. Dellasega, V. Russo, et al. “Ultra-low density carbon foams produced by pulsed laser deposition”. *Carbon*, **56**, 358 – 365 (2013).

[168] A. Macchi, M. Borghesi, and M. Passoni. "Ion acceleration by super-intense laser-plasma interaction". *Rev. Mod. Phys.*, **85**, 751–793 (2013).

[169] B. Qiao, M. Zepf, M. Borghesi, et al. "Stable GeV Ion-Beam Acceleration from Thin Foils by Circularly Polarized Laser Pulses". *Phys. Rev. Lett.*, **102**, 145002 (2009).

[170] F. Dollar, C. Zulick, A. G. R. Thomas, et al. "Finite Spot Effects on Radiation Pressure Acceleration from Intense High-Contrast Laser Interactions with Thin Targets". *Phys. Rev. Lett.*, **108**, 175005 (2012).

[171] B. Aurand, S. Kuschel, O. Jäckel, et al. "Radiation pressure-assisted acceleration of ions using multi-component foils in high-intensity laser–matter interactions". *New J. Phys.*, **15**(3), 033031 (2013).

[172] F. Pegoraro and S. V. Bulanov. "Photon Bubbles and Ion Acceleration in a Plasma Dominated by the Radiation Pressure of an Electromagnetic Pulse". *Phys. Rev. Lett.*, **99**, 065002 (2007).

[173] X. Zhang, B. Shen, L. Ji, et al. "Instabilities in interaction of circularly polarized laser pulse and overdense target". *Phys. Plasmas*, **18**(7), 073101 (2011).

[174] Y. J. Gu, Q. Kong, S. Kawata, et al. "Enhancement of proton acceleration field in laser double-layer target interaction". *Phys. Plasmas*, **20**(7), 070703 (2013).

[175] B. M. Hegelich, I. Pomerantz, L. Yin, et al. "Laser-driven ion acceleration from relativistically transparent nanotargets". *New J. Phys.*, **15**(8), 085015 (2013).

[176] D. Jung, L. Yin, D. C. Gautier, et al. "Laser driven $1GeV$ carbon ions from preheated diamond targets in the break out afterburner regime". *Phys. Plasmas*, **20**(8), 083103 (2013).

[177] D. Stark, L. Yin, B. Albright, et al. "Effects of dimensionality and laser polarization on kinetic simulations of laser-ion acceleration in the transparency regime". In "APS Meeting Abstracts", p. GO5.005 (2017).

[178] F. Wagner, S. Bedacht, V. Bagnoud, et al. "Simultaneous observation of angularly separated laser-driven proton beams accelerated via two different mechanisms". *Phys. Plasmas*, **22**(6), 063110 (2015).

[179] E. Lefebvre and G. Bonnaud. "Transparency/Opacity of a Solid Target Illuminated by an Ultrahigh-Intensity Laser Pulse". *Phys. Rev. Lett.*, **74**, 2002–2005 (1995).

[180] F. Cattani, A. Kim, D. Anderson, et al. "Threshold of induced transparency in the relativistic interaction of an electromagnetic wave with overdense plasmas". *Phys. Rev. E*, **62**, 1234–1237 (2000).

[181] M. Tushentsov, A. Kim, F. Cattani, et al. "Electromagnetic Energy Penetration in the Self-Induced Transparency Regime of Relativistic Laser-Plasma Interactions". *Phys. Rev. Lett.*, **87**, 275002 (2001).

[182] B. Shen and Z. Xu. "Transparency of an overdense plasma layer". *Phys. Rev. E*, **64**, 056406 (2001).

[183] S. Palaniyappan, B. M. Hegelich, H.-C. Wu, et al. "Dynamics of relativistic transparency and optical shuttering in expanding overdense plasmas". *Nat. Phys.*, **8**, 763 EP – (2012). Article.

[184] H. W. Powell, M. King, R. J. Gray, et al. "Proton acceleration enhanced by a plasma jet in expanding foils undergoing relativistic transparency". *New J. Phys.*, **17**(10), 103033 (2015).

[185] P. L. Poole, L. Obst, G. E. Cochran, et al. "Laser-driven ion acceleration via target normal sheath acceleration in the relativistic transparency regime". *New J. Phys.*, **20**(1), 013019 (2018).

[186] A. A. Gonoskov, A. V. Korzhimanov, V. I. Eremin, et al. "Multicascade Proton Acceleration by a Superintense Laser Pulse in the Regime of Relativistically Induced Slab Transparency". *Phys. Rev. Lett.*, **102**, 184801 (2009).

[187] J. A. Bittencourt. *Fundamentals of Plasma Physics* (Pergamon, 1986).

[188] R. Lichters, R. E. W. Pfund, and J. Meyer-ter-Vehn. "LPIC++ : A Parallel One-dimensional Relativistic Electromagnetic Particle-In-Cell Code". *MPQ Report*, **225** (1997).

[189] X. Q. Yan, C. Lin, Z. M. Sheng, et al. "Generating High-Current Monoenergetic Proton Beams by a CircularlyPolarized Laser Pulse in the Phase-StableAcceleration Regime". *Phys. Rev. Lett.*, **100**, 135003 (2008).

[190] T. Esirkepov, M. Yamagiwa, and T. Tajima. "Laser Ion-Acceleration Scaling Laws Seen in Multiparametric Particle-in-Cell Simulations". *Phys. Rev. Lett.*, **96**, 105001 (2006).

[191] A. Macchi and C. Benedetti. "Ion acceleration by radiation pressure in thin and thick targets". *Nucl. Instrum. Methods Phys. Res. A*, **620**(1), 41 – 45 (2010).

[192] D. Tatomirescu, D. Vizman, and E. d'Humières. "Numerical modeling of laser-driven ion acceleration from near-critical gas targets". *Plasma Physics and Controlled Fusion*, **60**(6), 064002 (2018).

[193] E. d'Humières, E. Lefebvre, L. Gremillet, et al. "Proton acceleration mechanisms in high-intensity laser interaction with thin foils". *Phys. Plasmas*, **12**(6), 062704 (2005).

[194] R. A. Loch, T. Ceccotti, F. Quéré, et al. "Ion acceleration in the transparent regime and the critical influence of the plasma density scale length". *Phys. Plasmas*, **23**(9), 093117 (2016).

[195] A. R. Holkundkar, C. Harvey, and M. Marklund. "Thomson scattering in high-intensity chirped laser pulses". *Phys. Plasmas*, **22**(10), 103103 (2015).

[196] H. Vosoughian, Z. Riazi, H. Afarideh, et al. "Enhancement of proton acceleration by frequency-chirped laser pulse in radiation pressure mechanism". *Phys. Plasmas*, **22**(7), 073110 (2015).

[197] Y. I. Salamin, J.-X. Li, B. J. Galow, et al. "Laser acceleration of proton bunches by petawatt chirped linearly polarized laser pulses". *Phys. Rev. A*, **85**, 063831 (2012).

[198] G. A. Mourou, T. Tajima, and S. V. Bulanov. "Optics in the relativistic regime". *Rev. Mod. Phys.*, **78**, 309–371 (2006).

[199] G. Brodin, M. Marklund, L. Stenflo, et al. "Dispersion relation for electromagnetic wave propagation in a strongly magnetized plasma". *New J. Phys.*, **8**(1), 16 (2006).

[200] N. Pathak, A. Zhidkov, T. Hosokai, et al. "Spectral effects in the propagation of chirped laser pulses in uniform underdense plasma". *Phys. Plasmas*, **25**(1), 013119 (2018).

[201] S. Salous. "Dispersion of chirp pulses by the ionosphere". *J. Atmospheric Sol.-Terr. Phys.*, **56**(8), 979 – 994 (1994).

[202] A. Macchi and C. Benedetti. "Ion acceleration by radiation pressure in thin and thick targets". *Nucl. Instrum. Methods Phys. Res. A*, **620**(1), 41 – 45 (2010).

[203] T. D. Arber, K. Bennett, C. S. Brady, et al. "Contemporary particle-in-cell approach to laser-plasma modelling". *Plasma Phys. Control. Fusion*, **57**(11), 113001 (2015).

[204] A. Sgattoni, L. Fedeli, S. Sinigardi, et al. "Optimising PICCANTE - an Open Source Particle-in-Cell Code for Advanced Simulations on Tier-0 Systems" (2015).

[205] U. Teubner and P. Gibbon. "High-order harmonics from laser-irradiated plasma surfaces". *Rev. Mod. Phys.*, **81**, 445–479 (2009).

[206] J. M. Cole, K. T. Behm, E. Gerstmayr, et al. "Experimental Evidence of Radiation Reaction in the Collision of a High-Intensity Laser Pulse with a Laser-Wakefield Accelerated Electron Beam". *Phys. Rev. X*, **8**, 011020 (2018).

[207] J. M. DAWSON. "Particle simulation of plasmas". *Rev. Mod. Phys.*, **55**, 403–447 (1983).

[208] C. BIRDSALL AND A. LANGDON. *Plasma Physics via Computer Simulation* (Boca Raton: CRC Press, 1991).

[209] D. FILIPPYCHEV. "Computing the Particle Paths in an Open-Trap Sharp-Point Geometry". *Computational Mathematics and Modeling*, **12**, 193–210 (2001).

LIST OF PUBLICATIONS AND PRESENTATIONS

International Journals

1. *Shivani Choudhary*, Amol R. Holkundkar , "Efficient ion acceleration by relativistic self-induced transparency in subwavelength targets", *Eur. Phys. J. D*, **70**, 234 (Nov. 2016).

2. *Shivani Choudhary*, Amol R. Holkundkar , "Chirp assisted ion acceleration via relativistic self-induced transparency", *Phys. Plasmas*, **25**, 103111 (Oct. 2018).

3. *Shivani Choudhary*, Amol R. Holkundkar , "Laser pulse dispersion in underdense plasma and associated ion acceleration by relativistic self-induced transparency", *Phys. Plasmas*, **26**, (Aug. 2019).

Conferences

1. *Shivani Choudhary*, Amol R. Holkundkar ,"Effect of Laser and Target Conditions on Proton Acceleration by Relativistic Self Induced Transparency Mechanism", *Proc. twenty fourth DAE-BRNS National Laser symposium (NLS-24), held at Raja Rammana Centre for Advanced Technology (RRCAT), Indore*, (2 Dec – 5 Dec 2015).

2. *Shivani Choudhary*, Amol R. Holkundkar , "Effect of Laser and Target conditions on Proton Acceleration by Frequency Chirped Laser Pulses", *32 PSSI, held at IPR, Ahemdabad*, (7 Nov – 10 Nov 2017).

3. *Shivani Choudhary*, Amol R. Holkundkar , "Study of Ion Acceleration using Frequency Chirped Pulses", *Proc. Twenty sixth DAE-BRNS National Laser symposium (NLS-26), held at BARC, Mumbai*, (23 Dec – 25 Dec 2017).

4. *Shivani Choudhary*, Amol R. Holkundkar , "Ion acceleration due to dispersion of laser pulse in under-dense plasma", *Proc. Twenty seventh DAE-BRNS National Laser Symposium (NLS-26), held at Raja Rammana Centre for Advanced Technology (RRCAT), Indore*, (3 Dec – 6 Dec 2018).

BRIEF BIOGRAPHY OF THE SUPERVISOR

Dr. Amol R. Holkundkar is an Associate Professor in the Department of Physics, Birla Institute of Technology and Science Pilani, Pilani campus. He received his Ph.D. degree from Bhabha Atomic Research Center (BARC) (University of Mumbai), in the year 2010. This was followed by a Post-Doctoral research work at Umeå University, Sweden. He joined the Department of Physics, BITS Pilani in 2012. He has published several highly cited paper in reputed international journals. His area of research is focused on the study of laser matter interaction.

BRIEF BIOGRAPHY OF THE CANDIDATE

Ms. Shivani Choudhary obtained her Bachelors degree in Electrical and Electronics Engineering from Uttarakhand Technical University, Dehradun in 2012. She joined Department of Physics, BITS Pilani in January, 2014 as a research scholar. She has completed her PhD in the area of Plasma physics specifically laser plasma interactions. She has published research articles in the journals of international repute. Along with it, she has participated and presented her work in various National conferences. Presently, she is working as a Research Fellow in Surface Plasma Attosource Group at ELI-ALPS, Szeged, Hungary.